Properties of axonal and synaptic extracellular field potentials in the barn owl

D I S S E R T A T I O N

zur Erlangung des akademischen Grades

d o c t o r r e r u m n a t u r a l i u m
(Dr. rer. nat.)
im Fach Biologie

eingereicht an der
Lebenwissenschaftlichen Fakultät
Humboldt-Universität zu Berlin

von
Dipl.-Phys. Thomas McColgan

Präsidentin der Humboldt-Universität zu Berlin:
Prof. Dr.-Ing. Dr. Sabine Kunst

Dekan der Lebenwissenschaftlichen Fakultät:
Prof. Dr. Bernhard Grimm

Gutachter:
1. Richard Kempter
2. Catherine Carr
3. Gaute Einevoll

Tag der mündlichen Prüfung: 28.8.2018

Ich widme diese Arbeit
meiner liebsten Franziska und meinen Eltern.

Acknowledgements

I would like to thank my supervisor Richard Kempter for his excellent support in the production of this dissertation, the inspiring discussions and his always helpful feedback. I thank Catherine Carr for her generosity in letting me use her experimental data, the opportunity to participate in experiments in her lab, useful advice and many introductions at conference posters. I would also like to thank Hermann Wagner for introducing me to barn owl research and for making the introduction to Richard Kempter that made this dissertation possible.

I thank my wonderful Franziska for all her support and patience, as well as for just being who she is.

Many thanks to my parents for their support, both spiritual and material, during my studies, and for always believing in whatever path I chose.

Thanks to Elvira Lauterbach, Karin Winkelhöfer, Rike Schupper and Andreas Hantschmann for administrative and technical support that helped everything run smoothly.

Thanks to all my colleagues at the ITB, in particular Paula Kuokkanen, for many productive discussions and for being a great desk neighbor. Nikolay Chenkov for many pelasant coffee breaks. All other members of the ITB for making it such a great and enjoyable place, that I am missing already. I would also like to mention Laurenz Wiskott, Mathias Franzius and Henning Sprekeler for welcoming me at the ITB in 2006 and giving me my first taste of computational neuroscience.

I also thank all my collaborators, in particular Anna Kraemer, Ji Liu and Sahil Shah for their experimental support, and Christine Köppl and Go Ashida for discussions and insights.

Abstract

Extracellular field potentials (EFPs) recorded in the brain are an important indicator of neural activity for neuroscientists. In many cases, their physiological basis is unknown or debated. The barn owl auditory brainstem provides an excellent opportunity to study these EFPs and their origins. The barn owl auditory brainstem is ideal because the field potentials are very large and very easily controlled by the auditory stimulus, and the underlying anatomy is well known. Here I present two examples of exploiting the unique properties of the EFP in the barn owl auditory brainstem. The first is concerned with axons, where I show that activity in axon bundles with characteristic termination zones generates strong dipole moments. The second example is concerned with synaptic currents, from which I was able to extract a signature of short-term plasticity. The methods and insights I developed are applicable to other organisms as well, and contribute to the general understanding of the roles different anatomical structures can play in the generation of EFPs.

Zusammenfassung

Im Gehirn gemessene Extrazelluläre Feldpotentiale (EFPs) sind ein wichtiges Maß für neuronale Aktivität. In vielen Fällen ist der genaue physiologische Ursprung dieser Potentiale unbekannt oder umstritten. Der auditorische Hirnstamm der Schleiereule bietet eine ausgezeichnete Möglichkeit, die EFPs und ihren Ursprung zu untersuchen. Der Hirnstamm der Eule ist ideal, weil das Feldpotential in ihm sehr stark ist, weil die zugrundeliegende Anatomie wohl-untersucht ist, und weil das Potential sehr einfach durch auditorische Stimulation gesteuert werden kann. In dieser Arbeit präsentiere ich zwei Beispiele, in welchen ich mir die einzigartigen Eigenschaften der Schleiereule zunutze mache, um das EFP zu erforschen. Das erste Beispiel behandelt Axone, und ich zeige, dass neuronale Aktivität in Axonbündeln, welche eine charakteristische Endzone besitzen, ein starkes Dipolmoment erzeugen kann. Im zweiten Beispiel behandele ich Synapsen. Aus den EFPs der Synapsen konnte ich die Merkmale der synaptischen Kurzzeitplastizität extrahieren. Die Methoden und Erkenntnisse die ich entwickelt habe sind auf andere Organismen übertragbar und erweitern das Verständnis vom Einfluss unterschiedlicher anatomischer Strukturen auf das EFP.

Contents

1 Introduction

When studying complex systems such as the brain, it is important to establish the relationships between the properties of the system that can be measured, and the underlying processes within the system that generate these properties. One example of such a relationship is the generation of extracellular field potentials in the brain. Without such an understanding, interpreting the extracellular field is mere speculation. When such an understanding is possible at the microscopic level, but the signals are measured at the macroscopic level, the interactions between the processes at intermediate scales need to be taken into account. This can be done in a bottom-up fashion, by modeling all the constituent parts and their interactions, or in a top-down fashion, by dissecting components of macroscopic signals and their interactions from a high level. The bottom-up approach is well-suited for theoretical studies, while the top-down approach is suited to experimental studies, where macroscopic signals are measured, and carefully designed interventions can reveal the finer structure of the system layer by layer. Ultimately, a full understanding requires a convergence of these two approaches.

The topic of this dissertation is the decomposition of such a signal, using a combination of top-down and bottom-up methods. I will first give an introduction into the system being studied. This will begin with an introduction to the history and current state of mathematical modeling of extracellular field potentials in the brain (Chapter 1.1) at different scales. Then follows a presentation of the brain regions of interest for this dissertation, the auditory brainstem of the barn owl, showing the progress which has been made in understanding the extracellular field potential in this system and the reason why it is ideally suited for the study of EFPs (Chapter 1.2).

I then show two concrete examples of how we can use this approach to gain an understanding of the system. The first is the study of axon bundles, where we can use the extracellular fields recorded from multielectrode arrays in order to infer activity patterns and the morphological structures of incoming nerve fibers in the nucleus laminaris (Chapter 2). The second example shows how, using also a pharmacological technique, we can gain an understanding about the synaptic dynamics in the nucleus (Chapter 3).

These concrete examples are followed by an outlook on how the presented work could be extended in the future. In particular, suggestions are made how a

complete understanding of all constituent components of the neurophonic could be achieved, and how the scope of the work could be extended to include more easily accessed far field potentials such as the auditory brainstem response (Chapter 4).

Chapters 2 and 3 are designed to be self-contained. Chapter 2 is based on the manuscript published as (McColgan et al., 2017).[1]

1.1 Extracellular field potentials in the brain

1.1.1 Basic mathematical description

In order to derive the bottom-up model of extracellular field potentials, we start out by considering Maxwell's equations (Maxwell, 1863; Heaviside, 1893). Because recording electrodes are large compared to individual atoms, the appropriate formulation to consider are the macroscopic Maxwell's equations in a linear medium:

$$\nabla \cdot \epsilon \mathbf{E} = \rho \tag{1.1}$$

$$\nabla \times \mathbf{E} = -\frac{\partial}{\partial t}\mathbf{B} \tag{1.2}$$

$$\nabla \cdot \mathbf{B} = 0 \tag{1.3}$$

$$\nabla \times \frac{1}{\mu}\mathbf{B} = \mathbf{J} + \frac{\partial}{\partial t}\epsilon \mathbf{E} \tag{1.4}$$

where $\mathbf{E}$ and $\mathbf{B}$ are the electrical and magnetic fields, ρ is the charge density, $\mathbf{J}$ is the current density, ϵ is the electrical permittivity, and μ is the magnetic permeability. $\nabla = (\partial_x, \partial_y, \partial_z)$ is known as the Nabla operator.

For the fields in the brain, oscillations are typically at frequencies of below 10 kHz, in which case the influence of magnetic induction is negligible: $\frac{\partial}{\partial t}\mathbf{B} \approx 0$. This means that the electrical field is conservative, and can be stated as the gradient of a potential ϕ:

$$\mathbf{E} = \nabla \cdot \phi \tag{1.5}$$

[1] These chapters are the result of a collaboration with several researchers. I conceived the projects, performed the data analysis, produced the figures and wrote the text. The experimental data was recorded by Catherine Carr with help from Ji Liu and Anna Kraemer at the University of Maryland. Paula Kuokkanen, Hermann Wagner and Richard Kempter helped with discussions and editing of the manuscripts.

We will treat the extracellular medium is an Ohmic conductor, meaning that it has the same resistivity at all frequencies. There is some debate on whether this assumption is justified Bédard et al. (2010), but experiments seem to suggest that the assumption is justified for frequencies below 10 kHz (Logothetis et al., 2007). A similar derivation for the basic equations of the extracellular field which includes a frequency-dependent extracellular medium can be found in (Bédard et al., 2004). Continuing with the assumption of a resistive medium, we can write that

$$\mathbf{J} = \sigma_e \mathbf{E} + \mathbf{J}_S \tag{1.6}$$

and

$$\nabla \cdot \mathbf{J} = 0 \tag{1.7}$$

where σ_e is the extracellular conductivity, and $\mathbf{J}_S$ is the so called "impressed current". The interpretation of this impressed current is not trivial, but in the case of the EFP in the brain it can be thought of as the current crossing the membranes into the extracellular medium (See Gratiy et al. (2017) for a derivation). The membrane current density entering or leaving the extracellular space is then defined as $i = -\nabla \cdot \mathbf{J}_S$. Taking the gradient of Equation 1.5 and substituting with Equations 1.6 and 1.7 then gives us

$$\nabla \cdot [\sigma_e \nabla \cdot \phi] = i \quad . \tag{1.8}$$

Equation 1.8 has the same form as the Poisson's equation found in electrostatics, with the exception that it treats current source densities instead of charge densities. This means that it can be solved for ϕ using the same mathematical methods, though it should not lead one to believe the underlying physical processes to the same. Solution methods for Poisson's equation can be found in standard texts on electrodynamics (Jackson, 2007).

I will give three important examples here: For the case of a collection of N point current sources I_n at points $\mathbf{r}_n$, the membrane current density is described by $i(\mathbf{r}) = \sum_n I_n \delta(\mathbf{r} - \mathbf{r}_n)$. In this case the solution is

$$\phi(\mathbf{r}) = \frac{1}{4\pi\sigma_e} \sum_n \frac{I_n}{\|\mathbf{r} - \mathbf{r}_n\|} \quad . \tag{1.9}$$

In the case of a current distribution spatially confined to a volume V, the solution is

$$\phi(\mathbf{r}) = \frac{1}{4\pi\sigma_e} \int_V \frac{I(\mathbf{r}')}{\|\mathbf{r} - \mathbf{r}'\|} \mathrm{d}\mathbf{r}' \quad . \tag{1.10}$$

In the case of a thin cylinder of length s, which is a good approximation for many segments of neurons, one can estimate the potential by that of a line at the center of the cylinder, in which case the potential has a simple analytic solution:

$$\phi_{\mathrm{LSA}}(r,h) = \frac{I}{4\pi\sigma_e s}\log\left|\frac{\sqrt{h^2+r^2}-h}{\sqrt{l^2+r^2}-l}\right| \tag{1.11}$$

where r is the radial distance from the line, h is the axial distance from one end of the line, and $l = h + s$ is the distance from the other end of the line. This is called the line source approximation (LSA, see Holt and Koch (1999); Gold et al. (2006)).

It is important to note that a number of assumptions were made in order to arrive at these equations. In particular, the intracellular and extracellular domains have been assumed to be perfectly screened from each other in the introduction of $\mathbf{J}_S$. Due to the high mobility of charges in the extracellular medium, this is in general a good approximation as the mobility leads to Debye screening of the domains from each other. The potentials differ from the approximation at distances smaller than the Debye length from the boundary, which is typically < 10 nm in the extracellular medium. Furthermore, diffusive currents due to the different concentrations and mobilities of various ionic species have been neglected. It has been suggested that these diffusive currents might cause errors in the CSD analysis by introducing spurious currents (Halnes et al., 2017).

There are a number of schemes to overcome these shortcomings, including the electroneutral (EN) and Poisson-Nernst-Planck (PNP) formulations. See (Pods, 2017) for an overview.

In this work, I relied on the solutions of Equation 1.8, and in particular on equation 1.9, and on the LSA in Equation 1.11 for the simulations in Chapter 3 that used LFPy (Lindén et al., 2014); more detailed approaches such as the PNP or EN formulations were not considered.

1.1.2 Synchrony and summation of extracellular field potentials

An important question that arises when studying EFPs, which typically cannot be attributed to single neurons, is how exactly the contributions from many neurons combine to form the measured response. Practitioners would frequently like to know which neuronal subpopulation contributes to the signal. This desire is reflected in the naming of the "local field potential" (LFP), which is arguably a misnomer, because the frequency content does not necessarily relate to the locality of a recorded potential. A related question which is generally more tractable than the attribution of distinct neuronal populations to EFP components is the determination of volume surrounding the recording

electrode that contributes to the recorded EFP. This question was first addressed experimentally in a number of studies, mainly in the cortex (Kreiman et al., 2006; Liu and Newsome, 2006; Berens et al., 2008; Katzner et al., 2009; Xing et al., 2009). The findings of these studies were seemingly contradictory, with values for the radius of the contributing volume ranging from several millimeters (Kreiman et al., 2006) to a hundred micrometers (Xing et al., 2009; Katzner et al., 2009).

The missing piece in this puzzle is that the synchrony of the contained neurons plays a crucial role in determining the size of the recorded volume. This was suggested early by Mitzdorf (1985), and described mathematically by Kuokkanen et al. (2010), closely followed by Lindén et al. (2011) and (Denker et al., 2011). Essentially, unsynchronized contributions will cancel each other out to an increasing degree as the volume gets larger and the contained population grows, while synchronized contributions add up and lead to a contribution even from large distances.

In Chapter 2 I present a method of estimating how synchrony can interact with the anatomy of a fiber bundle to generate stronger or weaker signals. Surprisingly, in this case there can be a resonant degree of synchronization of spikes within a volley, with both higher or lower synchronization leading to a weaker population signal.

1.1.3 Inverse methods

The models described in the previous sections provide a way of predicting EFPs from underlying neural activity. This is referred to as the forward problem. In most cases, however, the experimenter is interested in the opposite direction of inference: it is possible to measure the EFP, and one would like to draw conclusions about the underlying activity, in particular the membrane currents. This is called the inverse problem. In the most general case (compare Equation 1.8), this problem is solved by calculating the Laplacian of the EFP, which leads us to the current density

$$i = \sigma_e \Delta\phi \quad . \tag{1.12}$$

In most experimental settings, it is not possible to solve the inverse problem in its general form, because the distribution of membrane currents in space is not sufficiently constrained by the measured EFP. Solving the inverse problem would require a dense three-dimensional array of electrodes.

In special cases, it is possible to include additional assumptions about the distribution of currents, which makes the inverse problem solvable with one- or two- dimensional electrode configurations.

The simplest assumption is a laminar symmetry of the current distribution, where currents are equal in all directions except along the axis of the multielectrode array. In this case, the Laplacian can be approximated by its finite difference formulation. This method was popularized by Nicholson and Freeman (1975) and is known as the current source density (CSD).

The one-dimensional CSD has enjoyed very high popularity for many years. Linear electrodes are easy to obtain and to handle compared to two- or three-dimensional arrays, and it is simple to calculate the CSD from the recorded potentials. However, the method has several shortcomings.

One critical problem of the conventional CSD analysis is that taking the second spatial derivative of the EFP severely amplifies the high-frequency noise. This was addressed by the so-called inverse CSD (iCSD) method (Pettersen et al., 2006). The general idea of iCSD is to take a more model-based approach to CSD analysis, by parametrizing the current distribution in a way that reflects the prior knowledge available about the system. If one knows that the current distribution should be smooth, an appropriate model is a spline. One can then parametrize the spline in such a way that the inverse problem remains solvable (by choosing the number of parameters equal to the number of recording locations), and obtain a better estimate of the current distribution. When using splines, the method is called spline-iCSD (Łęski et al., 2007), but other models can be applied to the iCSD approach as well.

A closely related extension of the CSD is the kernel CSD (kCSD) (Potworowski et al., 2011) The kCSD increases the number of allowable models to include technically underspecified models (i.e. models with more free parameters than recording channels), by incorporating standard methods for regularization from the field of machine learning. Such regularization methods also provide a more principled way of dealing with measurement noise. A further advantage of the kCSD is that it allows for the use of irregularly placed recording electrodes. The downside of the method is that it can rapidly get very computationally intensive.

In Chapter 2, I provide a novel method of solving the inverse problem based on prior knowledge of the signal-propagating properties of axons.

1.1.4 Spatial models and relationship to EEG

While EFPs recorded with invasive electrodes within the brain can be very useful for scientific studies, they are not suitable for medical applications, except for very rare cases in which such disruptive procedure can be justified. Electroencephalogram (EEG) recordings, on the other hand, are easily recorded from human and animal subjects. There are a number of closely related recording methods such as the ECoG and the ABR.

The interpretation of these EEG potentials can be separated into forward and backward problems, in a manner similar to that described for EFPs above. Forward problem approaches typically start with a higher-level description of brain activity, such as the dipole moments generated by the activity of a neuronal populations. In the study of EEG signals, the assumption of a homogeneous extracellular medium no longer holds, and it becomes necessary to model the macroscopic structure of the scull and the different conductivities of it's constituents. A popular approach is the four-sphere model, which models the skull as a series of concentric spherical shells, one shell each for cortical tissue, the cerebrospinal fluid (CSF), the skull, and the scalp (Nunez and Srinivasan, 2006). More sophisticated models also exist, most prominently the finite element method (FEM), which compartmentalizes the skull into more detailed segments and can handle more realistic, non-spherical geometries, and can incorporate morphometric or FMRI data (Ziegler et al., 2014; Yan et al., 1991).

Establishing forward models of the EEG make it possible to apply inverse methods to infer underlying activity from EEG signals (Nunez and Srinivasan, 2006; Sanei and Chambers, 2013), though the dispersive effects from the skull, as well as the distributed nature of cortical processing make it hard to directly attribute contributions of particular brain structures to EEG components. In the EEG literature this problem is called source localization (Sanei and Chambers, 2013).

More sophisticated experimental techniques, such as paired recordings and lesion studies have shown promise in linking brain structures more directly to their EEG contributions (for review see Michel et al., 2004).

1.2 Sound localization in the barn owl

1.2.1 Evolution and ethology

The barn owl is a hunter that hunts predominantly during the night or in the twilight hours. In the low light conditions during these hours, the barn owl cannot rely solely on vision to locate its prey. The primary mechanism used to identify and track prey is localization based on sounds emitted by the prey (Payne, 1971; Konishi, 1973).

There is a strong selective pressure on the barn owl to excel at the task of prey capture, and consequently also to excel at sound localization. Because they do not carry large fat reserves, barn owls will perish after going about one week without being able to eat Wagner et al. (2013). When raising their young, the owls have to feed themselves and the fledglings, meaning that capture must happen at a fast rate. It has been reported that in some cases, the parent

animal can return to the nest with fresh prey as often as once every 15 minutes (Wagner et al., 2013). An astonishing feat if one considers that this includes the time for feeding the fledgling, flying to the hunting location, locating the animal, capturing it, and returning to the nest. A study measuring the number of prey animals captured by a population of barn owls during roosting found that a barn owl will capture 2.5 prey animals per fledgling and night, with most of the captures occurring the first 3 hours after sunset (Browning et al., 2016).

This impressive performance is facilitated by a number of behavioural, morphological and neuronal adaptations. The facial ruff forms a disk that acts as a kind of parabolic dish, serving to focus incoming sound waves onto the ears (von Campenhausen and Wagner, 2006; Hausmann et al., 2009). The ruff consists of special types of feathers that further enhance this effect (von Campenhausen and Wagner, 2006).

When hunting by sound, the barn owl will typically turns its head roughly in the direction of a sound source when it initially perceives it. It then waits for some additional sound to ocurr while the head is oriented towards the sound source, before striking (Payne, 1971). The initial head turn will undershoot to a certain degree (Hausmann et al., 2009), consistent with the behaviour of a bayesian estimator with a prior biased in the current head orientation direction of the owl (Fischer and Peña, 2011).

The barn owl uses two main cues to localize the origin of a sound. The first is the interaural level difference (ILD), meaning the difference in sound intensity received between the ears. The second is the interaural time difference (ITD), meaning the difference in arrival time between the ears. ILD is used to determine the elevation of a sound source. This is possible because the ear canals of the barn owl are asymmetric, with one pointing slightly upward and the other pointing slightly downward. This has the effect of increasing the intensity of the sound arriving at the upward-pointing ear canal when the sound comes from above, and vice versa when the sound comes from below. The azimuth of a sound location is determined by ITD. If a sound originates from the right of the owl, sound waves will arrive at the right ear before the left ear. When the sound originates frontally, it arrives at both ears simultaneously. The precision obtained by the barn owl behaviourally is 1.5° Moiseff and Konishi (1981); Konishi (1973). This corresponds to a temporal accuracy of microseconds, a remarkably short time to discriminate if one considers that neuronal systems typically operate on timescales of milliseconds.

1.2.2 Auditory brainstem pathways

The initial processing of these auditory cues takes place in the auditory brainstem. The basic organization of the auditory brainstem is common to most birds, and is shown schematically in Figure 1.1.

Auditory stimuli arrive via auditory nerve fibers (ANF), pass on to the ipsilateral nucleus magnocellularis (NM) and the ipsilateral nucleus angularis (NA). From NA begins the pathway for processing the ILD cue, while NM is the first stage in the processing of ITD (Sullivan and Konishi, 1984). Responses in NL neurons are largely insensitive to ILD (Viete et al., 1997; Brette, 2011). The synapses formed between ANF axons and NM neurons are excitatory, and have a special morphology, with a large endbulb covering a significant portion of the soma. Similar endbulbs are found in the mammalian auditory brainstem, where they are called the calyx of Held. From NM, the signal is passed on to the ipsilateral and contralateral nucleus laminaris (NL), again via excitatory synapses. NL is the first point at which information from both ears is processed, and it is here that the ITD cue is first evaluated. The mechanism for the extraction of ITD will be explained in the following section. NA projects to the superior olivary nucleus (SON), which is an inhibitory nucleus. SON forms inhibitory projections onto the ipsilateral NL, NM, and NA. From NA and NL, the information is passed on to higher order nuclei not treated here. The studies presented here were both performed mostly in NL.

1.2.3 Neuronal mechanism of sound localization

The anatomy of the barn owl NL is highly structured, with axons from the ipsilateral NM entering from the dorsal side, and axons from the contralateral NM entering ventrally. These axons take up the majority of the volume of the nucleus, and NL neurons are sparsely distributed, with on average 100 µm between nearest neighbours. The structure resembles that suggested early on by Jeffress (1948) for the localization of sounds (Carr and Konishi, 1990). In the Jeffress model, ITDs are detected by means of delay lines emanating from both ears, together with a set of coincidence detectors, each connected to delay lines from both ears. The coincidence detectors function in such a way that they only respond when a signal reaches them from both ears simultaneously. This means that for any given coincidence detector, there will be an ITD which can be exactly cancelled out by the delays induced by the delay lines, and the coincidence detector will thus be tuned to that ITD. If one now imagines a linear array of such coincidence detectors, with the delay lines from both ears lined up along this array in opposite directions and contacting the coincidence detectors along the way, this array will form a map of ITD, as shown in Figure 1.2A.

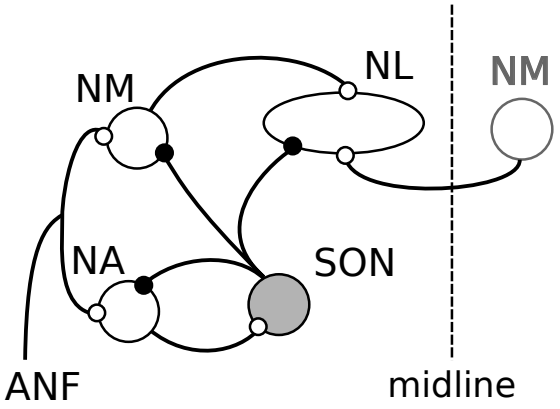

Figure 1.1: Connectivity diagram of the avian auditory brainstem. Nuclei are labeled with their abreviations: nucleus magnocellularis (NM), nucleus angularis (NA), nucleus laminaris (NL), and superior olivary nucleus (SON). The auditory nerve fibers are labeled ANF. Large circles indicate the nuclei, filled white for excitatory neurons and gray for inhibitory neurons. Small circles indicate synapses, filled white for excitatory and black for inhibitory. Solid black lines indicate axons, the dashed black line indicates the midline. Only nuclei on one side of the midline are shown, except for the contralateral nucleus laminaris, from which projections cross the midline. Diagram adapted from Ohmori (2014).

In the barn owl, the Jeffress model is implemented by the NM axons forming the delay lines, and NL neurons act as coincidence detectors (Carr and Konishi, 1990; Ashida et al., 2007; Simon et al., 1999), shown in Figure 1.2B. NL neurons have a number of morphological adaptations that impove their function as coincidence detectors and enable the extraordinary temporal precision they achieve, such as the passive soma with negligible dendrites (Ashida et al., 2007) and the axonal site of spike initiation (Kuba et al., 2006).

1.3 The extracellular field potential in the barn owl auditory brainstem

1.3.1 Properties of the neurophonic potential in the barn owl nucleus laminaris

In the studies presented here, I analyzed and modeled data recorded in the auditory brainstem of the barn owl. In many parts of the auditory brainstem, the EFP has prominent frequency-following component, which is called the "neurophonic" (Weinberger et al., 1970). The neurophonic has been observed in the NL of the chicken (Schwarz, 1992; Wagner et al., 2005, 2009; Köppl and Carr, 2008), as well as the analogous nucleus in mamals, the medial superior

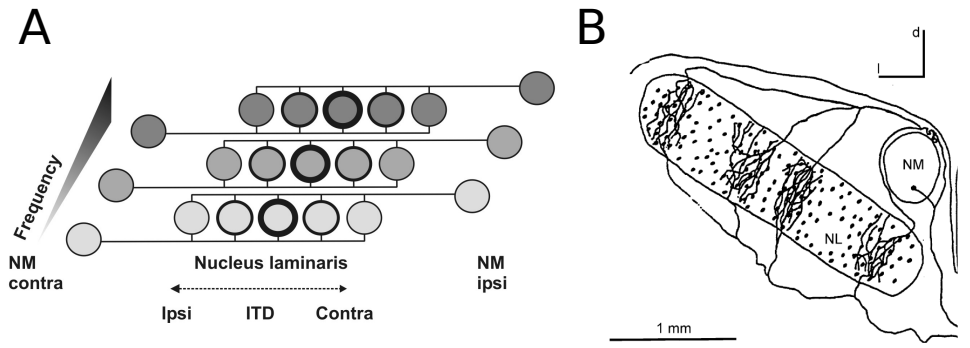

Figure 1.2: The Jeffress model of sound localization and its implementation in the barn owl. (**A**) Schematic diagram of Jeffress model and frequency map in NL. Neurons (depicted as circles) are tuned to a specific frequency, indicated by shade of gray. Within a frequency layer, neurons receive inputs from NM neurons tuned to the same frequency, from both the ipsi- and contralateral side. Neurons from one iso-ITD layer indicated by thick circles. (**B**) Anatomic structure of ITD detection structure in NL. Dots indicate locations of NL cell bodies. Traces show an ipsilateral and a contralateral axon entering NL. Ipsi- and contralateral axons run in opposite directions and form synapses with NL neurons, resulting in an ITD gradient in their responses. Dorsal (d) and Lateral (l) directions indicated by axes at the top. (A) from (Vonderschen, 2008), (B) from (Wagner et al., 2013).

olive (MSO) (Weinberger et al., 1970; Boudreau, 1965).

The neurophonic in the barn own NL is large, reaching amplitudes of several millivolts (Carr and Konishi, 1990; Kuokkanen et al., 2010). It is organized in a tonotopic manner, meaning that at any location there is a stimulus frequency that elicits a maximal response amplitude. The potential then also oscillates with this stimulus frequency. The tonotopic map is oriented in the rostrocaudal direction in NL, and it is smooth, meaning that as the electrode moves along the tonotopic axis, changes in frequency response are gradual. The neurophonic can be measured for stimulus frequencies of up to 10 kHz (Carr and Konishi, 1990).

A further property of the neurophonic in NL is that it responds differentially to ITDs (Carr and Konishi, 1990). At a given location, there will be one ITD to which the response is maximal, which is called the best ITD. These best ITDs are also organized to form maps within NL (McColgan et al., 2014; Carr et al., 2015; Sullivan and Konishi, 1986a). The best ITD in these maps progresses in the dorsoventral direction. There are several such maps aligned next to each other in mediolateral direction. Each of these maps has a slightly shifted positions of best ITD = 0 ms relative to each other (Carr et al., 2015).

The neurophonic has extraordinary precision. Responses to clicks show a very

high degree of similarity across hundreds of presentations, with a jitter on the order of 2 µs (Wagner et al., 2009, 2005).

1.3.2 Origin of the neurophonic potential in the barn owl nucleus laminaris

In early studies it was unclear which components of the nucleus were causing the neurophonic (Sullivan and Konishi, 1986b). NL neurons may have seemed plausible because it was known that their firing rate was modulated by ITD, a property shared by the neurophonic as described above. However, in recent years it has become clear that the neurophonic is in fact generated to a large extent by the incoming axons and synapses from NM. The rise and fall of the amplitude of the signal, previously interpreted as a rise and fall in NL firing rates, is in fact due to the constructive and destructive interference of the input-driven signals, whose phase shifts relative to each other with ITD. This was shown by Kuokkanen et al. (2010), who determined that NL neurons are so sparsely distributed in NL (mean distance between neurons $\approx$ 100 µm), that the number of neurons that contribute to a recording could not reach the observed signal-to-noise ratio (SNR). The incoming axons, on the other had, are very densely packed in NL, and their number can account for the high SNR. A further argument that speaks against the NL neurons as a source of the neurophonic is their anatomy. The NL cells at frequencies above 2.5 kHz have almost no dendrites. This means that they do not generate a large dipole moment, and we should expect their extracellular fields to be weak. Recent work has shown that the contributions of NL neurons can be isolated in the spectral domain (Kuokkanen et al., 2017).

1.4 Aim of the dissertation

As I showed in the previous sections, the EFP in NL has a number of interesting properties: It has a relatively simple and well-understood underlying anatomy and physiology. It is a very strong and reliable signal. It is directly controllable by the presentation of binaural stimuli. These three properties make it ideal for a model study of the origin of an EFP. It might, in principle, be possible to understand which neuronal components contribute which parts to the measured neurophonic responses. Such a disentanglement would be extremely challenging in most other systems, because of greater variability in the underlying anatomical structures and neuronal activity (Richerson et al., 2005; Makarov et al., 2010; Makarova, 2011; Makarova et al., 2014; Herreras et al., 2015).

The main aim of the following two chapters will be the further understanding

of the exact composition of the neurophonic. In Chapter 2 I will show how the dominant axonal field potentials can achieve their large amplitudes and dipolar spatiotemporal distribution. In Chapter 3 I investigate the much smaller, synaptic component of the EFP in NL. Despite contributing less than 1% to the overall variance of the EFP, I demonstrate that it can be consistently isolated from the rest of the EFP, and that it can be used to understand the dynamical properties of the NM-NL synapses.

2 Extracellular potentials of axon bundles with termination zones

2.1 Introduction

Extracellular field potentials (EFPs) are at the heart of many experimental approaches used to examine the inner workings of the brain. Types of EFPs include invasively recorded signals such as the electrocorticogram (ECoG) and the local field potential (LFP), as well as the noninvasively recorded electroencephalogram (EEG) and the auditory brainstem response (ABR) (Brette and Destexhe, 2012; Nunez and Srinivasan, 2006). Measures derived from the EFP such as the current source density (CSD) and multiunit activity (MUA) are also frequently used. The origins of these signals and measures, especially in cases in which the activity is not clearly attributable to a single cell, is a matter of debate (Buzsáki et al., 2012).

EFPs in the brain were long thought to be primarily of synaptic origin (Buzsáki et al., 2012). As a consequence, many modeling studies focussed on the extracellular fields induced by postsynaptic currents on the dendrites and the soma of a neuron (Holt and Koch, 1999; Einevoll et al., 2013; Lindén et al., 2011, 2010; Fernández-Ruiz et al., 2013). However, a number of recent data analyses and modeling efforts have revealed that active, non-synaptic membrane currents can play an important role in generating population-level EFPs (Reimann et al., 2013; Anastassiou et al., 2015; Schomburg et al., 2012; Ray and Maunsell, 2011; Belluscio et al., 2012; Waldert et al., 2013; Ness et al., 2016; Scheffer-Teixeira et al., 2013; Reichinnek et al., 2010; Sinha and Narayanan, 2015; Taxidis et al., 2015), including far reaching potentials detectable at the scalp (Teleńczuk et al., 2011, 2015). Currents from the axon are still thought to be so small as to be of minor importance for the EFP.

One of the reasons for the assumption that axonal currents contribute little to the EFP is that the far field of an action potential traveling along an idealized straight and long axon is quadrupolar, meaning that it decays faster with distance than synaptic sources, which are typically dipolar (Nunez and Srinivasan, 2006). Surprisingly, theoretical (Tenke et al., 1993) and experimental studies indicated that the EFP of axonal responses may also have a dipolar structure. For example, Blot and Barbour (2014) reported an EFP

with a characteristic dipolar structure in the vicinity of cerebellar Purkinje cell axons; other studies (Swadlow et al., 2002; Swadlow and Gusev, 2000) showed that the axonal part of the EFP of thalamocortical afferents showed a polarity reversal associated with a dipolar source, and classical current source density studies found dipolar current distributions in axonal terminal zones in the cortex and the lateral geniculate nucleus, and attributed these to axons because of conduction velocities (Mitzdorf and Singer, 1978; Mitzdorf, 1985; Mitzdorf and Singer, 1977; see also Tenke et al., 1993). Here we introduce another experimental system and show a strong dipolar, axonal field potential in the auditory brainstem of the barn owl.

The discrepancy between the quadrupolar structure of EFPs generated by idealized axons, and the experimentally observed dipolar structure raises the question of how axons are able to generate dipolar field potentials. In this manuscript we show how dipolar far fields in the EFP of axons can be explained by the axons' anatomical structure. In particular, the branchings and terminations of axons in their terminal zone area deform the extracellular waveform (Gydikov et al., 1986; Gydikov and Trayanova, 1986; Plonsey, 1977) and can lead to a dipolar EFP structure. Axon bundles, sometimes called fascicles, exist throughout the peripheral and central nervous system and have such terminal zones (Kandel et al., 2000; Hentschel and van Ooyen, 1999; Nornes and Das, 1972; Goodman et al., 1984). The white matter of the mammalian brain can be viewed as an agglomeration of such fascicles (Schüz and Braitenberg, 2002). We therefore predict pronounced contributions of axon bundles to EFPs, which are neglected in current models.

In what follows, axonal contributions to the EFP are first investigated by a numerical model based on forward simulation (Holt and Koch, 1999; Gold et al., 2006). This first model includes a large-scale multi-compartment simulation (Jack et al., 1975; Rall, 1959; Abbott, 1992; Hines and Carnevale, 1997; Hines et al., 2009) of an axon population. We then outline the basic mechanisms by means of a second, analytically tractable, model of a generic axon bundle. Finally, we validate model predictions with data from multi-site *in vivo* electrophysiological recordings from the barn owl auditory brainstem.

2.2 Materials and Methods

2.2.1 Experimental recordings

The experiments were conducted at the Department of Biology of the University of Maryland. Data was collected from three barn owls (*Tyto furcata pratincola*). Procedures conformed to NIH Guidelines for Animal Research and were approved by the Animal Care and Use Committee of the University of

Maryland. Anaesthesia was induced prior to each experiment by intramuscular injection of a total of $8 - 10$ ml/kg of 20% urethane divided into three to four injections over the course of 3 hours. Body temperature was maintained at 39°C by a feedback-controlled heating blanket.

Recordings were made in a sound-attenuating chamber (Acoustic Systems Inc., Austin, TX, USA). Tungsten electrodes with impedances between 2 and 20 MΩ were used to find suitable recording locations in nucleus laminaris (NL). Once NL had been located, the tungsten electrode was retracted and replaced with a 32 channel multi-electrode array (A1x32-15mm-50-413-A32, Neuronexus, Ann Arbor, MI, USA). The multi-electrode array was lowered using a microdrive (MP225, Sutter Instruments Co., Novato, CA, USA) during continuous presentation of a white-noise burst stimulus until visual inspection of the waveform showed that NL was at the center of the array. A grounded silver chloride pellet, placed under the animal's skin around the incision, served as the animal ground electrode. Electrode signals were amplified by a headstage (HS36, Neuralynx Inc., Tucson, AZ, USA). An adapter (ADPT-HS36-N2T-32A, Neuralynx Inc.) was used between the electrode and the headstage. A further adapter (ADPT-HS-36-ERP-27, Neuralynx Inc.) was used between the headstage and the control panel in order to map all 32 channels to the amplifiers. Pre-amplified electrode signals were passed to the control panel (ERP27, Neuralynx Inc.), then to four 8-channel amplifiers (Lynx-8, Neuralynx Inc.), and then to an analogue-to-digital converter (Cheetah Digital Interface, Neuralynx Inc.) connected to a personal computer running Cheetah5 software (Neuralynx Inc.) where the responses were stored for off-line analysis.

Acoustic stimuli were digitally generated by a custom-made MATLAB (MathWorks, Natick, MA, USA; RRID:SCR_001622) script (McColgan and Liu, 2017) driving a signal-processing board (RX6, Tucker-Davis Technologies, Alachua, FL, USA) at a sampling rate of 195.3125 kHz. The sound stimuli were attenuated using a programmable attenuator (PA5, Tucker-Davis Technologies). Click stimuli were generated as a single half-wave of a 5 kHz sine tone. Miniature earphones were inserted into the owl's ear canals and fixed to a headplate. Acoustic stimuli were fed to these earphones. Stimulus delivery was triggered by National Instruments equipment (NI USB-6259 and BNC-2090A, National Instruments Inc, Austin, TX, USA), and stimulus presentation times were recorded along with the responses. Trigger pulses were configured in MATLAB through Ephus software (Vidrio Technologies LLC, Ashburn, VA, USA). Responses were averaged over 10 repetitions.

2.2.2 Multi-compartment model of axons

We modeled axons using NEURON (Hines and Carnevale, 1997; Hines et al., 2009) and extended previous work by Simon et al. (1999) and Kuba and Ohmori

(2009), which included the high- and low-threshold potassium channels used by Rathouz and Trussell (1998). The axon was modeled as a sequence of active nodes and passive myelinated segments. The nodes and myelinated segments had lengths of 2 µm and 75 µm, respectively. We used the model of a nucleus magnocellularis (NM) axon provided by Simon et al. (1999) in ModelDB (Hines et al. (2004), Accession number: 153998). In order to ensure robust spike propagation at the bifurcations, some of the model the parameters were modified. The values of the properties that were modified from those provided by Simon et al. (1999) are shown in Table 1. In addition, the Q10 values were set to 3, and the temperature was set to 40° C as done by Kuba and Ohmori (2009). The ratio of leak conductance and capacitance between node and myelin was changed from 80 as used by Simon et al. (1999) to 1000 (Koch, 2004). We removed the Hodgkin-Huxley type potassium conductivities included by Simon et al. (1999) (which are based on data from the squid axon) from the simulations, and increased the KLVA and KHVA conductances (which are based on physiological data from the auditory brainstem) to compensate. In order to avoid nodes lining up in axial direction, the very first myelinated segment had a length drawn from a uniform distribution between 0 and 75 µm.

We included branching axons in our simulations. Branches were generated by connecting the incoming passive segment to one end of a node, and the two outgoing passive segments to the other end of the node, and then continuing the alternation of active and passive segments in each resulting branch. In Figure 2.1A-D, where the positions of bifurcations or terminations of axons were fixed, the last node was placed in the axon as usual, and the last myelinated segment was shortened in order to obtain the total length before the bifurcation or termination.

To approximate the infinitely long axons, we added segments before and after the shown portions of the axon. We chose the total length of the additional segments by incrementally increasing the length segment-by-segment until there was no visual difference between each successive lengthening of the axon, arriving at a length of 3 mm at each end.

To evoke an action potential at a designated time, a special conductance was temporarily activated in the first node of Ranvier. The conductance had a reversal potential of 0 mV, a maximal amplitude of 0.05 µS, and a time course described by an alpha-function with time constant 0.01 ms. Soma and axon initial segment were not modeled explicitly. This conductance resembled a synaptic conductance, except for the very short time constant and the lack of a somatic or dendritic compartment on which synapses typically impinge.

For the simplified axon geometries used in Figure 2.1, the branching pattern was fixed as described in the caption, with the exception of the axial positions of the branching points in Figure 2.1E: a random offset between branching points was drawn from a gamma distribution with mean 400 µm and standard

deviation 300 µm. The initial branching point for each axon was offset from the original location by a distance drawn from a Gaussian distribution with mean zero and a width of 300 µm. This was done to smooth out the effects of individual branchings or terminations.

For the axons in Figure 2.2, branching patterns were generated procedurally, starting with a root segment. In order to avoid artifacts from the stimulus and to simulate a long fiber tract prior to the terminal zone, a sequence of 10 active and passive segments without bifurcations was assumed before the terminal zone (770 µm total length). To this root, segments were appended iteratively. Before adding a segment, a decision whether to branch or terminate an axon was drawn from a probability distribution that was dependent on the axial position of the end of the previous segment. These probability distributions were modeled as logistic functions with the parameters adjusted to roughly match the numbers of branchings and terminations shown by Carr and Konishi (1990). Thus, an initial phase dominated by bifurcations was followed by a phase dominated by terminations, with the probability of termination reaching 100% at the end of the terminal zone. The distribution of bifurcations had its maximum at axial location $z = 0$ with a standard deviation of 200 µm. The distribution of terminations had its maximum at $z = 500$ µm, with a standard deviation of 100 µm. The branching angle had an average of 20°, with a standard deviation of 5°. At branching points, the plane containing the branches had a uniform random orientation, resulting in a 3-dimensional structure of the axon bundle.

In all cases except for the simulations shown in Figure 2.2, the radial position of all node and myelin compartments was set to zero, meaning they were placed on a straight line extending axially.

Numerical simulations of action potentials propagating along axons yielded the membrane currents from which we calculated extracellular fields. This procedure is described in detail by Gold et al. (2006). Briefly, the extracellular medium is assumed to be a homogeneous volume conductor with conductivity σ_e, and a quasi-static approximation of the electrical field potential ϕ is made. The extracellular potential $\phi(\mathbf{r}, t)$ at location $\mathbf{r}$ and time t due to a membrane current density distribution $i(\mathbf{r}, t)$ is then governed by the equation $\Delta\phi(\mathbf{r}, t) = \frac{1}{\sigma_e} i(\mathbf{r}, t)$, with Δ denoting the Laplace operator (Nunez and Srinivasan, 2006). If the currents i are constrained to a volume W, this equation has the solution

$$\phi(\mathbf{r}, t) = \frac{1}{4\pi\sigma_e} \int_W \frac{i(\mathbf{r}', t)}{|\mathbf{r} - \mathbf{r}'|} \mathrm{d}\mathbf{r}' \ . \tag{2.1}$$

Since the majority of the current flows through the small nodes of Ranvier in myelinated axons, we used the point-source approximation for all compartments, and subdivided the myelinated segments into 10 iso-potential sections each;

Symbol	Meaning	Value	Value used by Simon et al. (1999)
R_a	axial resistance	50 Ω cm	200 Ω cm
$\bar{g}_{\mathrm{Na}}$	maximum sodium conductance	2.4 S/cm^2	0.32 S/cm^2
$\bar{g}_{\mathrm{KLVA}}$	maximum low-threshold potassium conductance	0.1 S/cm^2	3 mS/cm^2
$\bar{g}_{\mathrm{KHVA}}$	maximum high-threshold potassium conductance	1.5 S/cm^2	30 mS/cm^2
$g_{\mathrm{leak}}^{\mathrm{node}}$	leak conductance in node	1 mS/cm^2	0.28 mS/cm^2
$g_{\mathrm{leak}}^{\mathrm{myelin}}$	leak conductance in myelin	1 µS/cm^2	35 µS/cm^2
E_{leak}	leak reversal potential	-72 mV	-45 mV
E_{K}	potassium reversal potential	-80 mV	-60 mV
E_{Na}	sodium reversal potential	50 mV	40 mV
c_m^{myelin}	membrane capacitance in myelin	1 nF/cm^2	12 nF/cm^2

Table 2.1: Parameter values used for the multi-compartment model which were modified from those used by Simon et al. (1999).

we did not use the line-source approximation (Holt and Koch, 1999).

Analysis of the resulting extracellular field potential (EFP) included filtering. All filtering was performed with third-order Butterworth filters. The multi unit activity (MUA) was calculated by high-pass filtering the signal with a cutoff of 2500 Hz, setting all samples with negative values to zero, and then low-pass filtering the resulting response with a cutoff of 500 Hz. The low-pass filtered EFP was calculated with a cutoff of 1000 Hz. To exclude influences of spectral leakage on our results, we also performed the same analysis with 20th-order Butterworth filters and found qualitatively identical results. The specific filtering (3rd or 20th order Butterworth) did not affect our conclusions.

The code for these simulations is available at `https://github.com/phreeza/pyLaminaris` (McColgan and Liu, 2017).

2.2.3 Mean-field model of an axon bundle

To better understand the processes leading to the complex spatio-temporal patterns of extracellular fields, we devised an analytically tractable model of axon bundles. We defined the spatial dimension in cylindrical coordinates $\mathbf{r} = (\rho, \varphi, z)$, where ρ was the radial distance from the cylindrical axis, φ the angle of azimuth, and z the axial distance along the cylinder axis. We considered a simple model axon bundle that extended infinitely in the axial z-direction at $\rho = 0$. The bundle had a variable number of fibers along the z axis, denoted by $n(z)$, each of which cylindrical with an identical radius a. This meant that the total cross-sectional area A of the bundle at a given depth z was given by $A(z) = \pi a^2 n(z)$. We assumed the axons to be perfect transmission lines, meaning that the action potential is a traveling wave with velocity v along the axon. In particular, we neglected delays and distortions that can be induced when an axon branches or terminates. In this case, we could assume that the membrane voltage was the same in each fiber for a given z coordinate. From linear cable theory (e.g. Jack et al., 1975), we then obtained the following expression for the total transmembrane current per unit length $I(z,t)$ from a given membrane potential $V(z,t)$:

$$I(z,t) = \frac{\partial}{\partial z}\left(\frac{A(z)}{r_L}\frac{\partial}{\partial z}V(z,t)\right) \tag{2.2}$$

$$= \frac{\pi a^2}{r_L}\frac{\partial}{\partial z}\left(n(z)\frac{\partial}{\partial z}V(z,t)\right) \tag{2.3}$$

$$= \frac{\pi a^2}{r_L}\left(\frac{\partial}{\partial z}n(z)\cdot\frac{\partial}{\partial z}V(z,t) + n(z)\cdot\frac{\partial^2}{\partial z^2}V(z,t)\right) \tag{2.4}$$

We next calculated the corresponding extracellular field potential $\phi(\mathbf{r},t)$ of a given membrane potential waveform $V(z,t)$ propagating through the axon bundle. Due to the rotational symmetry of the system and the fact that current flows only at $\rho = 0$, the membrane current can be described as $i(\mathbf{r},t) = I(z,t)\frac{\delta(\rho)}{\rho}$, where $\frac{\delta(\rho)}{\rho}$ is the Dirac delta distribution for a line at $\rho = 0$. Applying this membrane current to Equation 2.1, we obtained

$$\phi(\mathbf{r},t) = \frac{1}{4\pi\sigma_e}\int_{-\infty}^{\infty}\frac{I(z',t)}{\sqrt{(z-z')^2+\rho^2}}\mathrm{d}z' \ , \tag{2.5}$$

which is independent of the angle φ.

To derive the frequency responses in Figure 2.3, we simulated the membrane potentials as sinusoids, i.e. $V(z,t) = \sin(2\pi f\cdot(z-tv))$, with varying frequen-

cies f between 100 Hz and 5 kHz and calculated the standard deviation of the response for each frequency individually. The amplitude of the membrane potential V was the same for all frequencies.

To derive the dipole moment of a simplified projection zone, we considered an axon bundle in which identical spikes with the waveform $V_{\text{spike}}(z,t)$ propagate as traveling waves with a velocity v in positive z direction: $V_{\text{spike}}(z,t) = V_{\text{spike}}(z-tv,0)$. If each of the fibers is stimulated with an inhomogeneous Poisson process, with the driving rate $\lambda(t)$ shared among all axons, the average membrane potential across fibers will be $V(z,t) = V_{\text{spike}}(z,t) * \lambda(t)$, where $*$ denotes the convolution with respect to the time t. Plugging this into Equation 2.4, we obtained

$$I(z,t) = \frac{\pi a^2}{r_L}\left(\frac{\partial}{\partial z}n(z)\cdot\frac{\partial}{\partial z}\left[V_{\text{spike}}(z,t)*\lambda(t)\right] + n(z)\cdot\frac{\partial^2}{\partial z^2}\left[V_{\text{spike}}(z,t)*\lambda(t)\right]\right) \tag{2.6}$$

$$= \frac{\pi a^2}{r_L}\lambda(t) * \left(\frac{\partial}{\partial z}n(z)\cdot\frac{\partial}{\partial z}V_{\text{spike}}(z,t) + n(z)\cdot\frac{\partial^2}{\partial z^2}V_{\text{spike}}(z,t)\right) . \tag{2.7}$$

2.2.4 Analytical solution of the mean-field model of an axon bundle

Assuming Gaussian shapes for the firing-rate pulse $\lambda(t) = \bar{\lambda}_{\text{pulse}}\exp\left(-\frac{t^2}{2\sigma^2_{\text{pulse}}}\right)$, the spike $V_{\text{spike}}(z,t) = V_{\text{spike}}(z-tv,0) = \bar{V}_{\text{spike}}\exp\left(-\frac{(z-tv)^2}{2\sigma^2_{\text{spike}}}\right)$, and the fiber bundle projection zone $n(z) = \bar{n}\exp\left(-\frac{z^2}{2\sigma_{\text{n}}^2}\right)$, we were able to take advantage of the fact that the product and the convolution of two Gaussians are again Gaussian, and obtained

$$I(z,t) = \bar{n}\bar{\lambda}_{\text{pulse}}\bar{V}_{\text{spike}}\sqrt{2}\pi^{3/2}a^2\cdot\exp\left(-\frac{z^2}{2\sigma_n^2} - \frac{(z-tv)^2}{2v^2\left(\sigma^2_{\text{pulse}}+\sigma^2_{\text{spike}}\right)}\right) \tag{2.8}$$

$$\cdot\frac{\sigma_n^2\left(-v^2\sigma^2_{\text{pulse}} - v^2\sigma^2_{\text{spike}} + (z-tv)^2\right) - v^2 z\left(\sigma^2_{\text{pulse}}+\sigma^2_{\text{spike}}\right)(tv-z)}{v^4 r_L\sigma_n^2\sqrt{\frac{1}{\sigma^2_{\text{pulse}}}+\frac{1}{\sigma^2_{\text{spike}}}}\left(\sigma^2_{\text{pulse}}+\sigma^2_{\text{spike}}\right)^2} .$$

The dipole moment $p(t)$ is defined as

$$p(t) = \int_{-\infty}^{\infty} z \cdot I(z,t)\mathrm{d}z \quad , \tag{2.9}$$

into which we can enter Equation 2.8 to obtain

$$p(t) = -\bar{n}\bar{\lambda}_{\text{pulse}}\bar{V}_{\text{spike}}\frac{2\pi^2 a^2}{r_L}\frac{v^2\sigma_n\sigma_{\text{pulse}}\sigma_{\text{spike}}}{\left(\sigma_n^2 + v^2\left(\sigma_{\text{pulse}}^2 + \sigma_{\text{spike}}^2\right)\right)^{3/2}} \cdot t \exp\left(\frac{-t^2v^2}{2\left(\sigma_n^2 + v^2\left(\sigma_{\text{pulse}}^2 + \sigma_{\text{spike}}^2\right)\right)}\right) \quad . \tag{2.10}$$

The dipole moment has its peak amplitude at $t_{\max} = -\sqrt{\sigma_n^2 + v^2\left(\sigma_{\text{pulse}}^2 + \sigma_{\text{spike}}^2\right)}/v$, and takes the value

$$p_{\max} = p(t_{\max}) = \frac{2a^2\pi^2}{r_L\sqrt{e}} \cdot \frac{v\sigma_n\sigma_{\text{pulse}}\sigma_{\text{spike}}\bar{n}\bar{\lambda}_{\text{pulse}}\bar{V}_{\text{spike}}}{\left(\sigma_n^2 + v^2\left(\sigma_{\text{pulse}}^2 + \sigma_{\text{spike}}^2\right)\right)} \quad , \tag{2.11}$$

which is presented as Equation 2.12 in the Results section.

2.2.5 Model fitting to experimental data

In order to relate the model to experimentally obtained data as shown in Figure 2.5, we performed a nonlinear least squares fit, minimizing the mean squared error ϵ between the measured potential ϕ_{measured} and the model prediction ϕ_{model} in Equations 2.5 and 2.4 for $N = 32$ measurement locations z_n $(n = 1, \ldots, N)$ and $M = 600$ time points t_m $(m = 1, \ldots, M)$: $\epsilon = \frac{1}{NM}\sum_{n=1}^{N}\sum_{m=1}^{M}\left[\phi_{\text{measured}}(z_n, t_m) - \phi_{\text{model}}(z_n, t_m)\right]^2$. The separation between electrodes was given by the electrode layout as 50 µm. The time between sampling points was 5.12 µs. We achieved the minimization of the error ϵ using the "optimize.minimize" routine provided by the SciPy package (Jones et al., 2001). The free parameters to be determined by the optimization routine were the distance ρ, the velocity v, the number of fibers per unit length $n(z_n)$ for each measurement location z_n, and the spatial derivative of the average membrane potential $\frac{\mathrm{d}}{\mathrm{d}z}V(z_1, t_m)$ at electrode location z_1 for each time point t_m. We fit the first derivative of the membrane potential in order to better capture the low-frequency components that we found in Figure 2.1 E, and because the membrane potential appears only as the derivative in the model. The derivative of the membrane voltage at the other locations than z_1 was then determined by the traveling-wave assumption: $\frac{\mathrm{d}}{\mathrm{d}z}V(z_n, t_m) = \frac{\mathrm{d}}{\mathrm{d}z}V(z_1, t_m - \frac{z_n - z_1}{v})$, using a linear interpolation between timepoints. The model assumption of a single line of axons with electrodes at a fixed distance is a simplification of a three-dimensional axon tree where the fibers are distributed at various distances.

The distance parameter ρ in Equation 2.5 can be interpreted as an average distance in this simplification.

To aid the convergence of the fit algorithm, an initial guess for the number of fibers $n(z_n)$ was set by hand. Initializing the guess to a constant or a fully random number of fibers resulted in a failure to converge. However, different Gaussian-like initial guesses converged to a single solution, meaning that the specific initial guess did not alter the final fit result. Initializing the membrane voltage with different normally distributed values did not affect the outcome of the fit. The results shown in Figure 2.5 were obtained with an initial guess of a Gaussian with amplitude 12, centered at penetration depth 725 µm with standard deviation 400 µm.

Because of the linearity of Equations 2.1-2.5 both in the current I and the membrane potential V, inferring the membrane voltage V from the average over trials of the extracellular potential ϕ produces the average membrane voltage V. This in turn is the membrane voltage response of a single spike convolved with the peri-stimulus time histogram (PSTH).

2.3 Results

2.3.1 Effects of axonal bifurcations and terminations on extracellular action potentials

To understand how the geometry of an axon affects the extracellular waveform associated with action potentials, we first numerically simulated single action potentials propagating along generic axons and calculated their contribution to the EFP (for details, see Materials and Methods). This was done for five scenarios: quasi-infinite axons, terminating axons, bifurcating axons, axons that bifurcate as well as terminate, and axon bundles (Figure 2.1). We began by simulating a long axon, approximating an infinitely long axon following a straight line path, neither bifurcating nor terminating (Figure 2.1A). The extracellular action potential has the characteristic triphasic shape. As the action potential travels along the axon, the waveform is translated in time with the conduction velocity, but is otherwise unchanged. The triphasic shape is also present in the spatial arrangement of transmembrane currents at any given time, which is the reason for the quadrupolar EFP response traditionally assumed for axons.

There are two ways of understanding the triphasic shape of the extracellular waveform. One way is by attribution of the peaks of the response to individual current types. The first, small positive peak corresponds to the capacitive current, the large and negative second peak to the sodium current, and the final positive peak to the potassium current (Gold et al., 2006). Another,

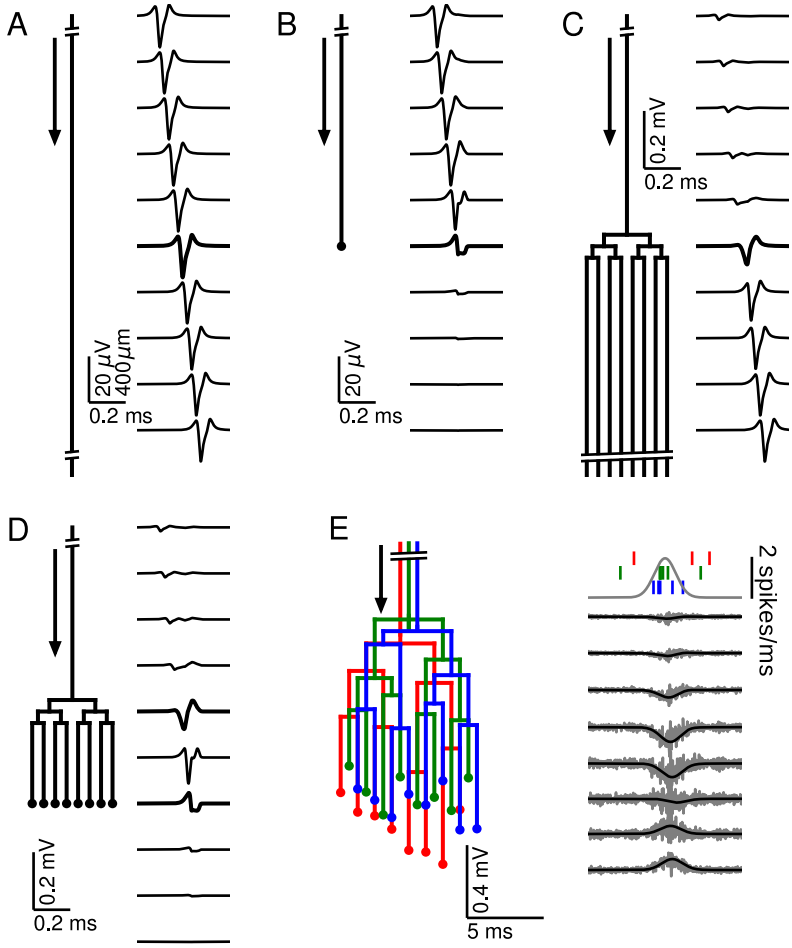

Figure 2.1: Relationship between axon morphology and extracellular potential. Multi-compartment simulations of action potentials traveling along axons with varying morphologies, as indicated by the diagram on the left-hand side of each subfigure. Action potential propagation direction indicated by arrow. Waveforms, shown on the right-hand side of each subfigure, were recorded at a horizontal distance of 150 µm from the axons. The vertical depth is indicated by the plot position, spaced by 400 µm. Horizontal plot location and distances between axons are for illustration only, all axons were simulated to lie on a straight line. (**A**) Action potential in a quasi-infinitely long, straight axon. (**B**) Terminating axon. Action potential waveform closest to the termination thickened for emphasis. (**C**) Branching axon. The axon branches multiple times within of 200 µm. Thicker waveform at the center of the bifurcation zone. (**D**) Combined bifurcations and terminations. Note the larger voltage scales in C and D, which correspond to the different number of fibers. (**E**) Response in a population of 100 randomized morphologies, three of which are shown schematically (colored). Activity consists of spontaneous background activity (100 spikes/s) superimposed with a brief Gaussian pulse of heightened spike rate (2000 spikes/s). Spike rate and example spike times for the three morphologies are shown at the top. Right: gray lines show activity of full population averaged over 40 trials, while the black lines show the low-pass (<1 kHz) component. Note that the time and voltage scales are different from A-D. In all graphs, spatial scales are the same, as indicated by the scale bar in A.

more mathematical way of understanding the triphasic shape is specific to the nature of the axon. Due to Kirchhoff's law and cable theory (see Materials and Methods), the local transmembrane current in a homogeneous axon is proportional to the second spatial derivative of the membrane potential along the direction of the axon. Because the action potential is roughly a traveling wave, the currents are also proportional to the second *temporal* derivative of the membrane potential. The three extrema of the EFP are thus related to the points of maximum curvature in the action potential waveform, namely the onset, the maximum, and the end of the spike.

Next we simulated the response of an axon that terminates (Figure 2.1B). Here the action potential approaching the recording location (top traces) has the same, triphasic EFP response as in the non-branching case. When the action potential reaches the termination point, its EFP gradually deforms into a biphasic response, with a positive peak preceding a negative peak. The mechanism for this deformation can be understood as follows: As the action potential approaches the recording location next to the termination, the majority of the transmembrane currents flow at points located before the termination, and they are almost identical to those in the non-terminating case; the first, capacitive peak is not affected. As already mentioned, the second and third peaks of the extracellular action potential in the non-terminating case are generated by currents close to or after the electrode location. In the terminating axon, there are no currents at points after the termination, leading to a partial suppression of the second peak and a complete suppression of the third peak.

Another generic structure found in axons is a bifurcation. To emphasize the impact of bifurcations, we simulated a single axon that bifurcates three times on each branch within a distance of 200 µm (100 µm between branchings), leading to a total number of 8 collaterals leaving the bifurcation zone (Figure 2.1C). (Note that in order to avoid confounding effects, the horizontal distances between axons in Figure 2.1C-E are for illustration only; all collaterals were simulated to lie on a straight line.) The EFP far away from the bifurcation zone has a triphasic shape and resembles the one observed in Figure 2.1A, and the amplitude is proportional to the number of axon fibers. The EFP near the bifurcation zone has a biphasic shape. Although there is an initial tiny positive peak, the response is dominated by the second, negative and the third, positive peak. This waveform can again be understood by comparison to the first example (Figure 2.1A) containing the infinitely long axon: The tiny positive initial peak resembles the infinite case, because it is constituted by the action potential-related currents flowing within the part of the axon before the bifurcation. As the action potential passes the bifurcation zone, there are now several action potentials (one in each fiber). Because of the active nature of the action potential, the active currents are the same in each outgoing fiber as in the incoming fiber. This leads the second and third peak to

be multiplied in size, yielding a quasi-biphasic response. We chose to simulate several bifurcations because this leads to a clearer effect in the EFP. In the case of a single bifurcation, this effect is also present, but the amplification of the second and third peak relative to the first peak is not as notable as in this example.

To understand how bifurcations and terminations interact when they are present in the same axon, we simulated an axon with an identical number of bifurcations as in the previous case, but then added terminations to all the fibers 700 µm after the bifurcation zone (Figure 2.1D). We found that this configuration leads to the same biphasic responses as observed in the cases of the isolated anatomical features. A triphasic response occurred in-between the bifurcation and termination zones. A notable point here is that the potential at the bifurcation and termination are both biphasic and on the same timescale, but opposite in polarity.

After having studied the EFPs of single axons, we next started to simulate axon bundles, because axons often run in parallel bundles in the brain. Moving towards more biologically plausible axon geometries, we considered bundles consisting of axons with slightly altered spatial arrangement: we randomly perturbed the precise locations of bifurcations and terminations in the axon tree (Figure 2.1E, left; for details, see Materials and Methods). We simulated 100 axons and stimulated each axon with an inhomogeneous Poisson spike train (Kuokkanen et al., 2010; Softky and Koch, 1993). The driving rate of the inhomogeneous Poisson process was the same for all axons and consisted of a constant background rate (100 spikes/s) and a Gaussian pulse of heightened activity (2000 spikes/s). The standard deviation of the pulse was 1 ms, resulting in an additional 3.5 spikes per axon being fired on average over the entire duration of the pulse. The resulting extracellular population-level waveforms (Figure 2.1E, right) showed a polarity reversal reminiscent of Figure 2.1D. However, in the bifurcation zone, the summed contribution from many fibers and action potentials lead to a monophasic negative peak, and in the termination zone there was a monophasic positive peak. Interestingly, the summed potential at the center of the terminal zone largely cancelled out.

The fact that the responses in Figure 2.1E were mostly monophasic can be explained by the presence of a non-zero bias in the biphasic responses observed for the single spike responses in Figure 2.1D: close to a bifurcation, the area under the negative part of the curve slightly exceeded that of the positive part, and vice versa close to a termination. When summed up over many spikes with different timings, this difference in areas induced a positive or negative polarity of the population response in Figure 2.1E.

The reversal behaviour shown in Figure 2.1E is similar to the polarity reversal associated with a dipole observed in experimental studies (Swadlow and Gusev, 2000; Swadlow et al., 2002; Blot and Barbour, 2014). To summarize, simple

one-dimensional model axon structures can produce complex and diverse spatiotemporal EFP responses, including monophasic, biphasic and triphasic waveforms, comparable to experimentally recorded responses.

2.3.2 Axonal projections generate a dipole-like field potential

Dipole-like EFPs have a much larger spatial reach than quadrupolar-like EFPs, which are typically associated with axons (Nunez and Srinivasan, 2006). To further understand whether and how axons can generate a dipolar EFP, in Figure 2.2 we turned to three-dimensional axon morphologies, in contrast to the one-dimensional case studied in Figure 2.1 (for details, see Materials and Methods). We thus simulated a parallel fiber bundle of 5000 axons that at first runs at a constant number of fibers without bifurcations and then reaches a terminal zone. Within this terminal zone, the fibers first bifurcate, which increases the number of fibers. Finally, as the axons reach the end of the terminal zone, they terminate and the number of fibers decreases to zero (example axon shown in Figure 2.2A). To model more closely the actual axonal structures found in nature, we included a radial fanning out of the branches as well as a more diverse set of morphologies with a variable number of bifurcations and terminations (for details, see Materials and Methods).

The spiking activity of a generic axon bundle was simulated by a background spontaneous firing rate of 100 spikes/s and a short pulse of increased activity. We chose a Gaussian pulse with an maximum instantaneous rate of 2900 spikes/s and a standard deviation of 2.8 ms. Note that this high driving rate is only the instantaneous maximum, and the actual firing rate is limited by the refractory period following a spike. These numbers are motivated by the early auditory system of barn owls (Köppl, 1997b; Sullivan and Konishi, 1984; Konishi et al., 1985), where instantaneous spike rates of 3000 spikes/s occur in response to click stimuli (Carr et al., 2016). However, our approach is not limited to the auditory system (which would also require the introduction of the synchronization of the spike times to the auditory stimulation frequency, called phase locking). Instead, this pulse of activity could relate to various kinds of evoked activity in the nervous system, such as sensory stimulation, motor activity or a spontaneous transient increase in population spiking activity.

To characterize the spatiotemporal dynamics of the evoked EFP, the time course of the potential was calculated for several locations along the axon trunk. The responses were averaged over 10 repetitions. We divided our analysis into two frequency bands by filtering the responses. The first frequency band was obtained by low-pass filtering with a cutoff frequency of 1 kHz (Figure 2.2A–C). The second frequency band was the multiunit activity (MUA) obtained by high-pass filtering with a cutoff frequency of 2.5 kHz (Figure 2.2D–F). To make the MUA easier to interpret in terms of overall activity reflected, it was half-wave

rectified and low-pass filtered (<500 Hz, see Materials and Methods). The two frequency bands showed a qualitatively different spatiotemporal response in the vicinity of the projection zone, as we will show in the following.

We first studied the effect of the Gaussian rate pulse on the low-pass filtered EFP (Figure 2.2B). The filtering removed most of the identifiable components of individual spikes, while a population-level signal remained, similar to an LFP signal. The distribution of the maximum amplitudes of these responses is shown by the colored contour lines in Figure 2.2A and the colored voltage traces in Figure 2.2B. Surrounding the terminal zone of the axon bundle in Figure 2.2A, low-pass filtered EFP amplitudes showed a double-lobed shape typical of a dipole.

In Figure 2.2B, the low-pass filtered EFP responses mostly showed monophasic deflections elicited by the population firing rate pulse, in a manner similar to that observed in Figure 2.1E. Such deflections were visible at all recording locations. In the radial direction away from the axon tree, i.e. in the horizontal direction in the figure, the low-pass filtered EFP amplitude decays. In the axial direction along the axon tree, i.e. in vertical direction in the figure, the voltage deflection reverses polarity in the middle of the terminal zone of the bundle (Figure 2.2B). The polarity reversal occurs by a decrease of the amplitude to zero and a subsequent reappearance with reversed polarity (as opposed to a polarity reversal through a gradual shift in phase). This behaviour is also typical for a dipolar field potential.

The point of the polarity reversal coincides with the middle of the terminal zone. Interestingly, this means that the absolute value of the response amplitude reaches a local minimum just at the axial location at which the number of axonal fibers reaches a maximum. To better understand how the anatomical features of the axon bundle and the EFP response amplitude are related, we compared its signed maximum value (meaning the *signed* value corresponding to the maximum *magnitude* of the amplitude of the EFP, black line in Figure 2.2C) with the change of the number of nodes per 200 µm bin (purple histogram in Figure 2.2C): Along the nerve trunk the number of fibers is constant. As the axon bundle reaches its terminal zone, the number of bifurcations increases (purple bars point to the right in Figure 2.2C). The increase of bifurcations is followed by an increase in terminations. In the middle of the terminal zone, the number of bifurcations and terminations are equal. At the same depth, the amplitude of the EFP component crosses zero. At the end of the terminal zone, the terminations outweigh the bifurcations (purple bars point leftwards in Figure 2.2C). As the axon bundle ends, there are no longer any bifurcations or terminations, and the number of fibers decays toward zero. Overall, the signed maximum amplitude EFP (black trace) follows the distribution of branchings and terminations (purple histogram). This progression of amplitudes in the low-frequency components seen in Figure 2.2C is also visible in Figure 2.2B, most

clearly in the first column. The polarity reversal in the center of Figure 2.2B corresponds to the crossing of zero amplitude in Figure 2.2C.

To understand how the EFP contributions are related to individual spikes, we next turned our attention to the high-frequency MUA. The MUA is thought to reflect local spiking activity (Stark and Abeles, 2007). In Figure 2.2D, the iso-amplitude lines of the MUA appeared like an ellipsoid centered at the terminal zone (Figure 2.2D); they did not show the double-lobe shape observed for the low-pass filtered EFP in Figure 2.2A.

The shape of the MUA response was weakly dependent on the recording location. The main change across locations was in the scaling of the amplitude (Figure 2.2E). The amplitude decays with radial distance from the trunk. In the axial direction, the amplitude reaches its maximum in the middle of the fiber bundle. This dependence of the MUA amplitude on the axial location is further examined in Figure 2.2F. The amplitude of the MUA component (black trace) changes in accordance with the local number of nodes per unit length (teal-colored histogram), which is proportional to the number of fibers. The local number of fibers and the MUA amplitude are both constant along the nerve trunk. Both measures then increase in amplitude as the number of fibers is increased by bifurcations. As the fibers terminate and the number of fibers decreases, so does the amplitude of the MUA.

To conclude, we have shown a qualitatively different behaviour in the low- and high-frequency components of the EFP, i.e. for the low-pass filtered EFP and the MUA. The particular branching and terminating structure of the axon bundle may thus give rise to a dipolar low-pass filtered EFP.

2.3.3 Effects of bifurcations and terminations on distance scaling of EFPs

To further demonstrate that bifurcations and terminations of axons give rise to a dipolar field, we investigated the effect of an axon terminal structure on the spatial reach of the EFP (Figure 2.3). Motivated by the fundamentally different spatial distributions of the low-pass filtered EFP and the high-frequency MUA in Figure 2.2, we again differentiated between these frequency bands and simulated an axon bundle containing a terminal zone with bifurcations and terminations. Moreover, as a control, we also simulated an axon bundle without bifurcations in which a fixed number of fibers simply terminates.

In order to separate the effects of any radial fanning out of the axon bundle from the effects of bifurcations and terminations, and to afford better analytic tractability, we transitioned back to a simpler one-dimensional model of the axon bundle (see Materials and Methods). This model omitted the radial fanning out of the bundle in the terminal zone, as in Figure 2.1. Furthermore,

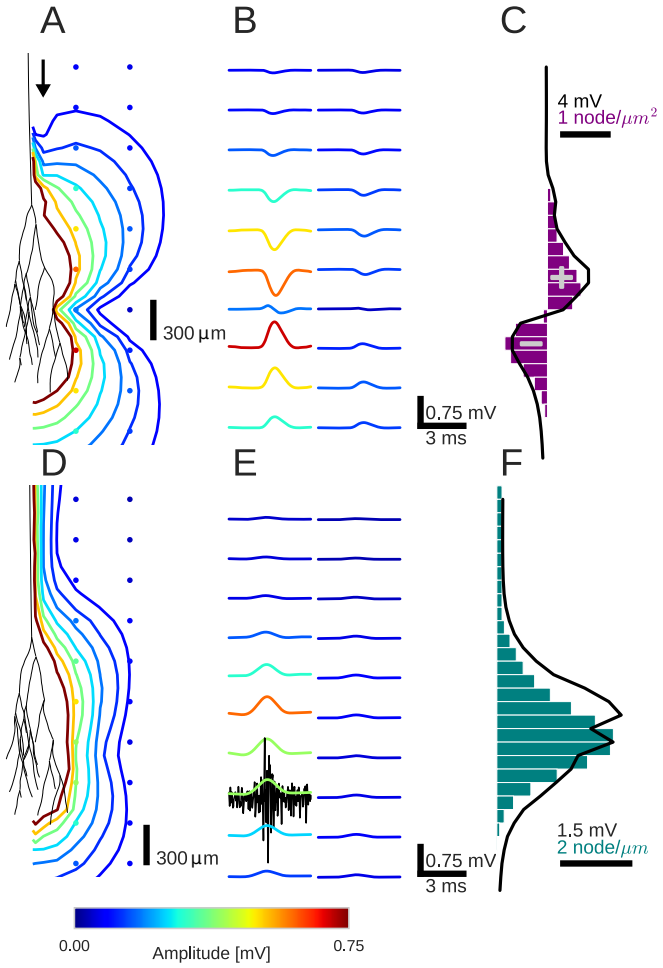

Figure 2.2: An activity pulse in an axonal projection generates a dipole-like extracellular field potential (EFP). (**A**) Modeled example axon from the simulated bundle in black, along with iso-potential lines for the low-pass filtered (<1 kHz) EFP signature of the activity pulse. The contours (amplitudes in mV as indicated by colorbar) show the typical double-lobe of a dipole. (**B**) The low-pass filtered EFP waveforms, recorded at the locations of the colored dots in *A*, show mostly unimodal peaks. The peak amplitude reverses polarity as a function of recording location in the vertical direction. The reversal occurs by inverting the amplitude with approximately unchanged shape. (**C**) Progression of the maximum low-pass filtered EFP amplitude with depth (black line) at a distance of 100 µm from the trunk (indicated by arrow in A). The amplitude closely follows the local change (spatial derivative) in number of nodes per unit length (purple histogram), which is proportional to the difference in number between bifurcations and terminations. (**D**) Modeled axon from bundle as in A, and iso-potential contours for the multi-unit activity (MUA) component. (**E**) Response waveforms of the MUA component. High-pass filtered (>2.5 kHz) component (the first processing stage for calculation of MUA, see Materials and Methods) in black. (**F**) Maximum amplitude of the MUA component (black line) follows the number of fibers (teal-colored histogram). Note the different units of the histograms in (C) and (F), due to the fact that (C) is the derivative in space of (F).

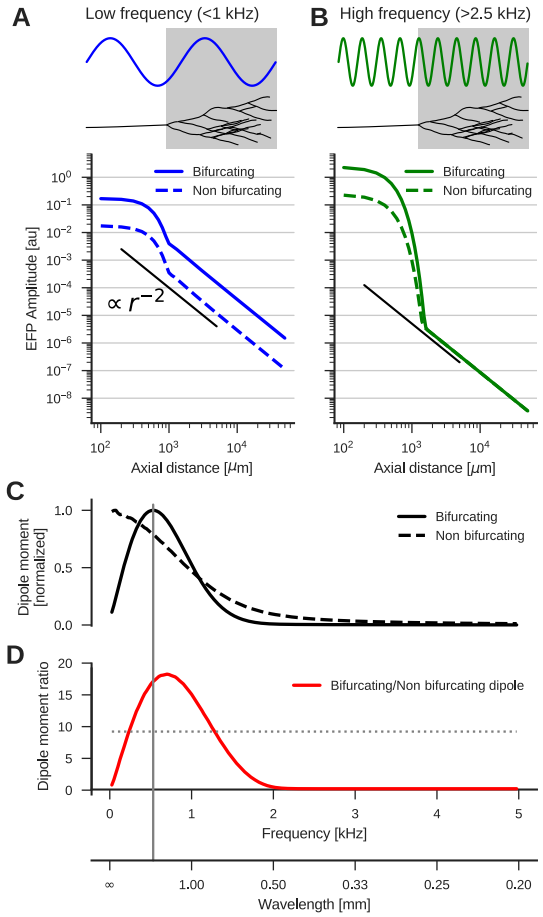

Figure 2.3: The low-frequency (<1 kHz) component of the axon bundle EFP is influenced supralinearly by a projection zone, while the high-frequency (>2.5 kHz) component is not. (**A**) Scaling of the low-frequency (<1 kHz) EFP component. (*Top*) The spatial wavelength of the membrane potential oscillation (blue) is larger than the width of the projection zone (gray). (*Bottom*) The amplitude of the low-frequency EFP component for the bifurcating case (solid line) decays with with axial distance from the axon bundle. It always always exceeds the EFP amplitude of the non-bifurcating case (dashed line). Note the double-logarithmic scale. Axial distances r are calculated from the center of the terminal zone. For comparison, scaling that follows r^{-2} is indicated with the black line. (**B**) Same as A but for the high-frequency (>2.5 kHz) EFP component. (*Top*) The spatial wavelength of the membrane potential oscillation (green) is much smaller than the width of the projection zone (gray). (*Bottom*) The amplitude of the high-frequency EFP decays several orders of magnitude within the terminal zone, and the amplitude is larger in the bifurcating case (solid line) compared to the non-bifurcating case (dashed line). Far away from the terminal zone, i.e., for axial distances $r > 1$ mm, they decay proportional to r^{-2} but with similar amplitudes.
(**C**) Normalized dipole moments of the bifurcating and non-bifurcating bundles as a function of frequency. (**D**) Ratio of the dipole moments between bifurcating and non-bifurcating cases (red line), compared to the maximum ratio 10 of the number of fibers (dotted line), to indicate supralinear (>10) and sublinear (<10) contributions. Vertical gray line in C and D indicates the width (~2 mm) of the projection zone.

we discarded the detailed conductance-based simulation of the membrane potential, and instead assumed a fixed membrane potential waveform traveling along the axon trunk with a constant propagation velocity. Using linear cable theory, it was then possible to calculate the membrane currents necessary for the determination of the EFP. The analytic nature of the simplified model also allowed us to consider a continuous number of fibers instead of simulating discrete bifurcations and terminations. All following simulations are based on this simplified model.

To verify that this simpler one-dimensional model accurately captures the EFP response of an axon bundle, we applied parameters equivalent to those used in Figure 2.2 and compared the resulting EFP to that obtained from the full biophysical model. We calculated the relative difference of the EFPs by taking the absolute value of their differences, and normalizing by the sum of their absolute values. Averaged over time, this relative difference at distances greater than 1 mm from the center of the projection zone was < 0.05 in axial direction. In the radial direction, we found, as expected, larger relative discrepancies of < 0.3 for radial distances > 1 mm. In what follows, we focus on the axial direction, which is the dipole axis.

Let us now specify how we simulated the two axon bundle morphologies. The control case was a non-bifurcating bundle, which had a constant number of 50 fibers up to the termination point, and then tapered out with a Gaussian profile that was centered at the termination point with a height of 50 fibers and width (standard deviation) of 300 µm. The second case was that of an axon bundle with a projection zone containing bifurcations. Here we added to the distribution of the number of axons used for the non-bifurcating control case a further Gaussian distribution to account for the projection zone. This additional Gaussian was also centered at the termination point, but had an amplitude of 450 fibers and a standard deviation of 500 µm, meaning that the overall width of the terminal zone was ≈ 2 mm. Unlike the tapering-out in the control condition, this component was added for both before and after the termination point. It resulted in a maximal fiber number of 500 at the termination point, which is a factor 10 larger than in the control case. Both distributions constructed in this way were smooth, and they had smooth first derivatives in space. In both cases, the number of fibers decreased monotonically after the termination point. We considered a conduction velocity of 1 m/s in this example, though results are qualitatively the same for other values. In order to understand the frequency-specific effects of the projection zone, we calculated the responses to membrane potential components with temporal frequencies between 25 Hz and 5 kHz, with the same amplitude for each frequency component. For the conduction velocity 1 m/s, these temporal frequencies corresponded to spatial wavelengths from 10 mm to 0.2 mm, i.e. from much larger to much smaller than the width of the terminal zone. We then calculated for each frequency/wavelength the average amplitude

of the resulting EFP response by taking its standard deviation. Due to the linear nature of our model, the frequency responses obtained in this manner are applicable to the Fourier components of any membrane potential time-course.

The dipole-like component observed in Figure 2.2 for the low-frequency component had its dipole axis aligned with the axon trunk. We therefore considered the distance r beyond the termination point in the direction extending the axon trunk, which we called the axial direction. Because we suspected a dipolar response, we expected the amplitude of the field potential to decay as r^{-2}. To test the scaling behaviour of this component, we first plotted the average amplitude of the low-frequency responses (f<1 kHz) in axial direction in Figure 2.3A. The plot is on a double logarithmic scale, meaning that the slope of the curve corresponds to the scaling exponent, and the vertical offset corresponds to the amplitude of the size of the dipole moment, which is a measure for the strength of the dipolar EFP. We observed the expected r^{-2} scaling for distances larger than the extent of the bifurcation zone ($\gtrsim$ 1 mm).

Comparing the responses of the bifurcating axon bundle and the non-bifurcating control condition (full and dashed lines in Figure 2.3A), we saw that for short distances ($<$ 1 mm) the response of the bifurcating case was a factor 10 larger than the control. At these distances the response was due to the local fibers, of which there are 10 times more in the bifurcating case. At distances larger than 1 mm, we observed that the distance scaling was proportional to r^{-2}, meaning that there was a dipole moment in both conditions (a vanishing dipole moment would have implied a slope steeper than r^{-2}). Interestingly, for distances larger than 1 mm the response in the bifurcating case exceeded the control by a factor 20. We thus concluded that at low frequencies, the bifurcation zone contributes supralinearly to the dipole moment.

The reason for this supralinearity is that contributions from different parts of the axon bundle can interfere constructively or destructively. The maximum constructive interference occurs when the spatial width of the oscillation agrees with that of the projection zone (Figure 2.3A, top). Importantly, currents from fibers inside the projection zone on average interact destructively with those from outside the projection zone. The magnitude of this effect depends on the ratio of the number of fibers inside the projection zone compared to the number outside. The larger the ratio the smaller the impact of destructive interference. Thus, bifurcations suppress the destructive interference (Figure 2.3A, bottom, full line). On the other hand, for a ratio of one, i.e. the non-bifurcating case, destructive interference is strong, which diminishes the overall response amplitude (Figure 2.3A, bottom, dashed line).

Next, we examined the high-frequency (>2.5 kHz) component (Figure 2.3B). As in the low-frequency case, the response at distances $<$ 1 mm was greater in the bifurcating case by a factor of 10. The asymptotic scaling was also r^{-2} for axial distances $>$ 1 mm in both cases. However, unlike in the low-frequency

case, the amplitudes were similar between bifurcating and non-bifurcating cases. Thus, the presence of a bifurcation zone did not contribute to the high-frequency dipole moments in the EFP. This feature is explained by the small spatial wavelength of the stimulus compared to the width of the bifurcation zone (Figure 2.3B, top)

2.3.4 Frequency-dependence of dipolar axonal EFPs

We showed that the dipole moment depends on both the anatomy, i.e. the presence of a projection zone, and the temporal frequency range (low vs. high frequencies) of the underlying activity. This relationship can be qualitatively understood by considering that in an axon bundle a voltage waveform propagates at some conduction velocity. The temporal frequency of this signal thus corresponds to a spatial frequency. If the spatial frequency of the membrane potential matches the width of the projection zone, the dipole moment can reach its maximum. In this case, at some point in time, positive membrane currents flow in one half of the projection zone and negative membrane currents flow in the other half (Figure 2.3A, top). For example, if the voltage waveform has a temporal frequency of 1 kHz and propagates at 1 m/s, the spatial wavelength is 1 mm. If the spatial width of the termination zone is about 1 mm, the dipole moment is maximal. In contrast, if the spatial wavelength is much smaller than the width of the projection zone, an alignment between projection zone and current flow is not possible, and the dipole is not amplified (Figure 2.3B, top) (for a detailed derivation see Materials and Methods).

To quantitatively understand the frequency-specific contributions to the dipole moments, we examined the scaling behaviour of the EFP as a function of frequency. The amplitude of the dipole moment was determined by fitting a straight line with slope -2 to the double logarithmic scaling of the standard deviation of the EFP at a given frequency. The fit was performed for distances > 1 mm. The extrapolation of this straight line to the axial distance 1 µm was then proportional to the dipole moment.

The normalized frequency-specific dipole moments are shown in Figure 2.3C. The dipole moment of the bifurcating case (solid line) has a maximum at around 500 Hz, as expected due to the agreement of the spatial wavelength (1 m/s / 500 Hz = 2 mm; gray vertical line in Figure 2.3D and C) and axial width (about 2 mm; gray box in Figure 2.3A and B) of the projection zone. The match is not exact because the shapes of sine wave and Gaussian are different. For lower and higher frequencies, there is a mismatch in spatial wavelength and the width of the projection zone, meaning that the projection zone contributes only less to the dipole moment, as also observed in Figure 2.3B for higher frequencies. In the non-bifurcating control case (dashed line) there is no projection zone, and the dipole moment decays monotonically with rising

frequency because higher frequencies correspond to a smaller spatial separation of positive and negative currents, and thus to a smaller dipole moment.

In the bifurcating case, the maximum number of fibers was increased by a factor of 10. Accordingly, an increase in the dipole moment by a factor of 10 from the non-bifurcating to the bifurcating case could be explained by just linearly summing the dipole moments of individual fibers. An increase in the dipole moment by a factor greater than 10 would be supralinear. In Figure 2.3D we compared this relative impact of the terminal zone on dipole moments (red line) by plotting the dipole moment ratios across frequencies. The contribution of the terminal zone is greater than 10 (dotted line) for intermediate frequencies between about 200 and 1300 Hz, and smaller than a factor 10 outside this frequency range.

Together, these observations show us that the terminal zone makes a frequency specific contribution to the far-reaching dipole field potential of the axon bundle. This provides a deeper understanding of the findings of Figure 2.2: At low frequencies (< 1 kHz), we observed a supralinear dipolar behaviour due to the specific morphology the bundle, with the projection zone forming the dipole axis. At higher frequencies, the bifurcation zone does not amplify the dipole moment, meaning that we could observe responses mainly locally.

2.3.5 The barn owl neurophonic potential in nucleus laminaris as an example for a dipolar field in an axonal terminal zone.

To test our prediction of dipolar extracellular field potential responses due to axon bundles, we recorded EFP responses from the barn owl auditory brainstem. The barn owl has a highly developed auditory system with a strong frequency-following response in the EFP (up to 9 kHz, Köppl (1997a)), called the neurophonic, which can be recorded in the nucleus laminaris (NL). In NL, the input from the two ears is first integrated to calculate the azimuthal location of a sound source, and this information is encoded in the EFP (Carr and Konishi, 1990). The EFP in this region is mainly due to the afferent activity, and the contribution of postsynaptic NL spikes is small (Kuokkanen et al., 2010, 2013). Furthermore, the anatomy of the afferent axons is well known and follows a stereotypical pattern (Carr and Konishi, 1988, 1990): Two fiber bundles enter the nucleus, with fibers from the contralateral ear entering ventrally, and from the ipsilateral ear entering dorsally. The axon bundles reach the NL from their origin without bifurcating, then bifurcate multiple times at the border of the NL, and then terminate within NL. Axon bundles have a strong directional preference and run roughly in parallel. Most of the volume within NL consists of incoming axons. This well studied physiology and anatomy makes the system an ideal candidate to investigate the EFPs of axon bundles; see the Discussion for arguments why synaptic contributions to

the EFP could also be neglected here.

To explore the spatiotemporal structure of the EFP in NL, we performed simultaneous multi-electrode recordings of the response in NL (Figure 2.4A) to contralateral monaural click stimuli. The click responses showed distinct low-frequency (Figure 2.4B) and high-frequency (Figure 2.4C) components, as previously reported (Wagner et al., 2009). The frequency of the high-frequency ringing corresponds to the recording location on the frequency map within NL, and the ringing reflects the frequency tuning and phase locking of the incoming axons. In addition, there is a low-frequency component in the response (Figure 2.4B). We filtered the data to separate these components, using the same cutoff frequencies as before for low-frequency (<1 kHz) and high-frequency (>2.5 kHz) EFP.

The same simplified model used in Figure 2.3 was fit to the data (example in Figure 2.4) by performing a nonlinear least squares optimization. The model considered only the average membrane potential across the fibers, and we calculated the membrane currents based on the density of fibers instead of simulating individual fibers. The model also discarded the radial extent of the bundle, treating it as a line; see Materials and Methods for more details on the model. Free parameters to be fit were (1) the number of fibers at the depth of each recording location, (2) the average spatial derivative of the membrane potential over time in the fibers at the location next to the most dorsal electrode, (3) the axonal conduction velocity, and (4) the average distance between the axon bundle and electrode array.

The resulting EFP responses and the model fit are depicted in Figure 2.5. Figure 2.5A shows the inferred average over trials of the deviation of the membrane potential from the resting potential in response to the stimulus, at a location in the axon next to the first electrode (penetration depth 1550 µm), obtained from the fit. The inferred voltage is composed of high- and low-frequency components similar to those observed in the EFP. The inferred number of fibers as a function of dorsoventral depth is shown in Figure 2.5B. The number (scaled by an arbitrary factor) has its maximum at the center of the electrode array, and decays steadily to both sides. This profile of the number of fibers is consistent with the known anatomy of axons in NL (Carr and Konishi, 1990; Kuokkanen et al., 2010).

The low-frequency (< 1 kHz, Figure 2.5C) responses reveal the typical polarity reversal that we predicted for an axonal terminal zone (Figures 2.1, 2.2). The dorsoventral depth in Figure 2.5C and D is on the vertical axis, which corresponds to the horizontal axis in Figure 2.5B. The orange lines indicate the actual responses in the data.

The low-frequency responses at the dorsal and ventral edges in Figure 2.5C show the same shape, but with opposite polarity, as expected for a dipolar field.

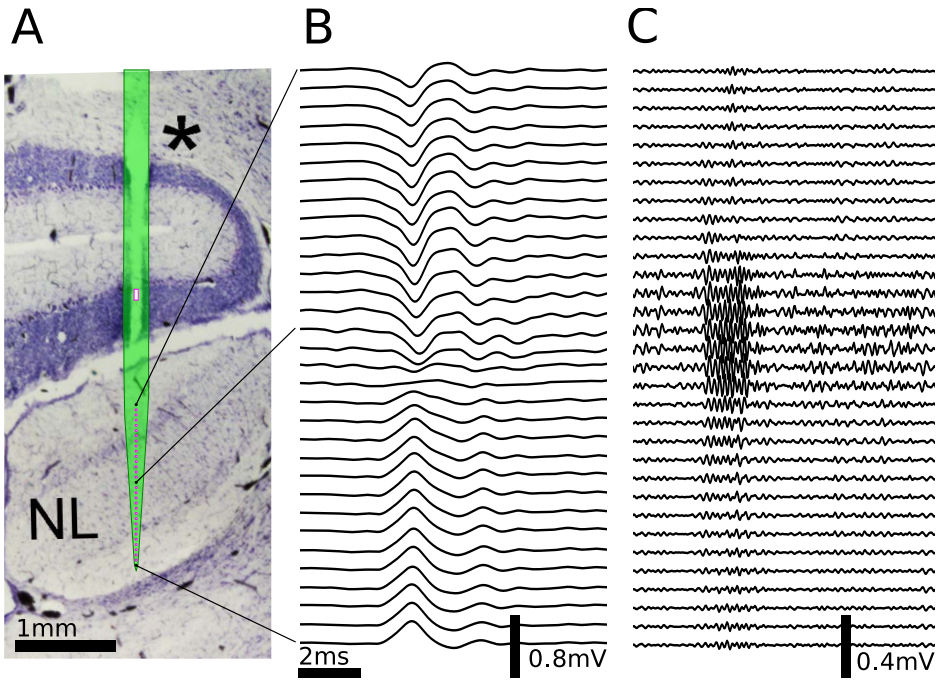

Figure 2.4: Multielectrode recordings in the barn owl show dipolar axonal EFPs. (**A**) Photomicrograph of a 40 µm thick transverse Nissl stained section through the dorsal brainstem, containing a superimposed, to scale, diagram of the multielectrode probe. The probe produced a small slit in a cerebellar folium overlying the IVth ventricle (*), and penetrated into the nucleus laminaris (NL). The recordings were made in NL, and electrodes extended to both sides of the nucleus. The outline of the probe is shown in light green, with the recording electrodes indicated by magenta dots, and the reference electrode as a magenta rectangle. The low-frequency (<1 kHz) component (**B**) and the high-frequency (>2.5 kHz) component (**C**) are ordered in the same way as the electrodes, with three examples connected to their recording sites by black lines. The time scales in B and C are identical (indicated by scale bar). Traces were averaged over 10 repetitions. Voltage scales are indicated by individual scale bars.

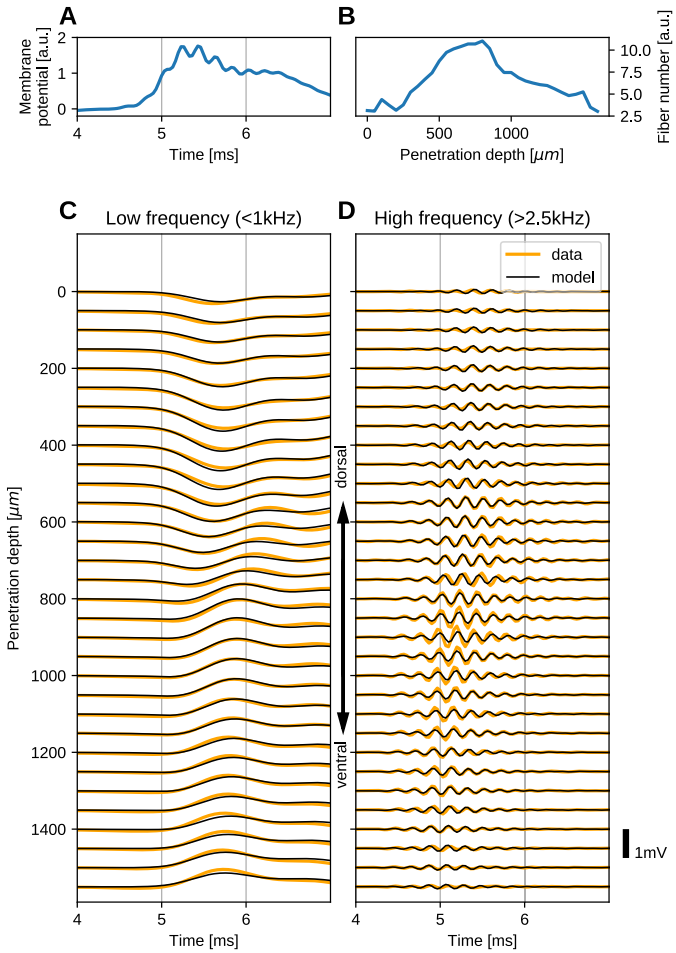

Figure 2.5: The spatial structure of EFPs recorded from the nucleus laminaris of the barn owl can be explained by a model of axonal field potentials (for details, see Materials and Methods). (**A**) Membrane voltage, averaged across fibers, in the model when fit to the data. (**B**) Fitted number of fibers in the model as a function of penetration depth. (**C**) Low-frequency (< 1 kHz) components of the EFP in response to a click stimulus at time 0 ms, at different recording depths. The depth is measured in the direction from dorsal to ventral. Recorded responses (orange) are shown along with model fits (black). (**D**) High-frequency (> 2.5 kHz) responses in recordings (orange) and model (black). Recorded traces were averaged over 10 repetitions.

Note that for a pure dipole field, the amplitude of the central responses have zero amplitude. In the data shown here, central responses show a diminished maximum amplitude, which we interpret as the contribution of higher-order (mostly quadrupole) components. The model is able to capture the behaviour of this quadrupolar component as well, with a slight underestimation of the amplitude of the peak at ventral locations. The model even captures a small oscillation in the data with period of ≈ 1 ms in the center of the recording. Here, too, the small deviations are likely due to slightly inhomogeneous conduction velocities or non-axonal sources.

In addition to the dipolar behavior of the low-frequency response, we also examined the high-frequency (> 2.5 kHz) response, shown in Figure 2.5D. The responses have a Gabor-like shape, as expected (Wagner et al., 2009), with maximum amplitude in the center of the recording array, at around 850 µm penetration depth. The axonal conduction velocity was calculated to be 4.0 m/s, and the distance from the bundle was 162 µm. A previously published estimate of the axonal conduction velocity in this nucleus (McColgan et al., 2014) gave a confidence bound of 0.4–6 m/s. Toward the edges ($<$ 100 µm and $>$ 1400 µm), the amplitude decays. In the central region (400–1200 µm recording depth), a systematic shift in delay can be observed, while the response appears stationary in the more dorsal and ventral electrodes. The delay increases from ventral to dorsal, which is consistent with the anatomy for contralateral stimulation.

All these aspects of the data are qualitatively reproduced by the model (Figure 2.5C and D, black traces). The main deviation between model and data lies in a diminished amplitude of the high-frequency oscillation modelled at the most central electrode sites (Figure 2.5D). Because the phase shift in the central region is mainly determined by the conduction velocity, this mismatch might be due to a variable conduction velocity in the nucleus, and the constant velocity in the model. McColgan et al. (2014) showed that different conduction velocities exist in the core and periphery of the nucleus, as predicted by Carr and Konishi (1990) from variable internode distances. A diminished amplitude in the fit could reflect an inability of the model to exactly match the phase progression. Another possible explanation is that the additional amplitude could be due to non-axonal sources such as synaptic currents or postsynaptic spikes, which do not follow the assumptions underlying our model; see the Discussion for arguments why we expect such contributions to the EFP to be small.

When comparing the inferred membrane potential response (Figure 2.5A) to the measured EFP response (Figure 2.5C and D), the most salient difference is the dissimilar sizes of the frequency components. In the EFP, the low-frequency component has a comparable amplitude to the high-frequency component, but in the membrane potential the low-frequency component is much larger. This

is because the EFP is related to membrane currents, which are proportional to the first and second derivatives of the membrane potential, and taking the derivative is equivalent to applying a high-pass filter.

We performed the fitting procedure (example in Figure 2.5) for 26 recordings from 3 different owls, with monaural stimulation from both ears (implying the activation of distinct axonal populations). The average correlation coefficient for all recordings was $R^2 = 0.56 \pm 0.15$. The correlation coefficient for the example shown in Figure 2.5 was 0.62.

2.3.6 Dipole moments of idealized axon bundles

We have shown theoretically and experimentally for specific examples of axonal projection zones and inputs how dipolar EFPs emerge. We now generalize this approach to predict the resulting dipolar EFP for arbitrary axon and stimulus configurations. Based on our cable-theory model, we analytically derived the maximal dipole moment $p_{\max}$ for a large range of scenarios. From a given dipole moment the maximum far field potential at distance r can be calculated as $\phi_{\max} = \frac{p_{\max}}{4\pi\sigma_e r^2}$ where σ_e is the extracellular conductivity.

To simplify the analytical derivation as much as possible, we assumed a Gaussian waveform for the membrane potential of a single spike, with an amplitude $\bar{V}_{\text{spike}}$ and a width σ_{spike}. The resting membrane potential was irrelevant because only the first and second derivatives of the membrane potential contribute. The axon bundle population consisted of fibers with radius a, axial resistance r_L, and conduction velocity v. The population was assumed to be driven with a Gaussian firing-rate pulse with maximum firing rate $\bar{\lambda}_{\text{pulse}}$ and width σ_{pulse}. The distribution of the number of fibers at a given depth location was also described with a Gaussian, with width σ_n and maximum number $\bar{n}$. This is an adequate approximation if the spikes in the incoming fibers contribute little to the dipole moment before reaching the projection zone. In this scenario, we calculated the peak dipole moment of the bundle (see Materials and Methods for details) to be

$$p_{\max} = \frac{2\pi^2 a^2 \bar{n} \bar{\lambda}_{\text{pulse}} \bar{V}_{\text{spike}}}{\sqrt{e} r_L} \cdot \frac{v \sigma_n \sigma_{\text{pulse}} \sigma_{\text{spike}}}{\left(\sigma_n^2 + v^2 \left(\sigma_{\text{pulse}}^2 + \sigma_{\text{spike}}^2\right)\right)} \quad . \tag{2.12}$$

Equation 2.12 tells us that the dipole moment is proportional to a^2, $\bar{n}$, $\bar{\lambda}_{\text{pulse}}$, $\bar{V}_{\text{spike}}$, and $1/r_L$. The dependence on v and the widths is more complicated; the response is maximal with respect to the three (spatial) widths σ_n, $v\sigma_{\text{pulse}}$ and $v\sigma_{\text{spike}}$ when they satisfy the condition $w_1^2 = w_2^2 + w_3^2$ where w_1 is the largest of the three terms, while w_2 and w_3 are the other two terms, regardless of order.

The dipole moment is thus maximal when the widths of the spike, the pulse, and the terminal zone agree. In particular, if σ_n (the width of the terminal zone) is the widest, then the dipole moment is maximal if σ_n is equal to the spatial width of the overall activity in the axons, which is $v\sqrt{\sigma_{\text{spike}}^2 + \sigma_{\text{pulse}}^2}$. The widths add in this way because the overall activity is the convolution of two Gaussians.

Using this formula, it is then possible to calculate the expected contributions to the EFP for different scenarios. To test the approximation in the case of the barn owl, we chose the following values: axon radius $a = 1$ µm, conduction velocity $v = 4\ \frac{\text{m}}{\text{s}}$ as inferred in the previous section, axial resistivity $r_L = 1\ \Omega\text{m}$, and extracellular conductivity $\sigma_e = 0.33\ \frac{\text{S}}{\text{m}}$ as used in studies of the cortex (Gold et al., 2006; Holt and Koch, 1999), anatomical and physiological parameters $\sigma_n = 500$ µm, $\bar{n} = 80000$, $\bar{V}_{\text{spike}} = 70$ mV from (Carr and Konishi, 1990), and activation patterns for click stimulation from (Köppl, 1997b; Carr et al., 2016): $\bar{\lambda}_{\text{pulse}} = 1000$ spikes/s, $\sigma_{\text{spike}} = 250$ µs, $\sigma_{\text{pulse}} = 0.5$ ms. This leads to a value for the dipole moment of $p_{\max} \approx 2.5\,\mu\text{A}\cdot\text{mm}$. At a distance of 750 µm, roughly the furthest distance recorded with the multielectrode array in Figure 2.4 and Figure 2.5, this dipole moment corresponded to a field potential of 1.1 mV, consistent with the order of magnitude of the responses in our experiments (Figures 2.4, 2.5).

Dipole sources are also to be expected to make up the majority of the electrical signals recorded at the scalp (Nunez and Srinivasan, 2006). One such signal is the auditory brainstem response (ABR), which is recorded at the scalp in response to auditory stimulation with clicks or chirps (Riedel and Kollmeier, 2002). An amplitude of about 10 µV of the ABR in the barn owl has recently been reported by Palanca-Castan et al. (2016). We calculated the contribution expected from an axon bundle with the same characteristics as described before at 2 cm from NL, aiming to estimate the contribution to the ABR. Multiplying by a factor of 2 to account for the fact that there is an NL in each hemisphere, the predicted contribution was 3.1 µV, which is of the same order of magnitude as the value reported in the experiments.

To estimate the low-frequency dipole moment of NL from our multielectrode recordings, it is sufficient to use CSD analysis in one dimension, i.e. $\frac{\partial^2}{\partial z^2}\phi(z) = \frac{1}{\sigma_e} i(z)$ and a simple sinusoidal approximation of the voltage within NL: $\phi(z) = \phi_0 \sin(2\pi z/L)$ for $-L/2 < z < L/2$ and $\phi(z) = 0$ otherwise, where $\phi_0 \approx 0.5$ mV is the amplitude, $L \approx 2$ mm is the spatial wavelength, and z is the depth in NL with $z = 0$ being in the center. To convert the current density i into a current, we approximate the NL volume that contributes to the dipole as $V_{\text{NL}} \approx 6\ \text{mm}^3$ (Kuokkanen et al., 2010). We assume that the current is homogeneously distributed in the directions perpendicular to z. Using the definition of a dipole, $p_{\max} := \int \mathrm{d}V\, i(z) z$, we can integrate over the dimensions perpendicular to z and obtain $p_{\max} = \frac{V_{\text{NL}}}{L} \int_{-L/2}^{L/2} \mathrm{d}z\, i(z) z$. Substituting $i(z)$ and solving the integral,

we find the maximum dipole moment to be $p_{\max} = 2\pi V_{\mathrm{NL}} \sigma_e \phi_0 / L \approx 3\ \mu\mathrm{A} \cdot \mathrm{mm}$, which is consistent with our previous estimates.

As a second example, we considered thalamocortical projections, for which Swadlow and Gusev (2000) reported amplitudes of extracellular spike-related potentials, called axon terminal potentials, at various locations; for example, at 400 µm from the center of the dipole, they reported an amplitude of the response of ≈ 1 µV. Individual thalamocortical axons are thin and have large and highly branched projection zones (Feldmeyer, 2012), so we estimated $\sigma_n = 250$ µm, $\bar{n} = 30$, and $a = 1$ µm. We assumed a jitter $\sigma_{\mathrm{pulse}} = 125$ µs in the arrival time instead of a true activity pulse, and we normalized the pulse to have area 1 because we were considering a spike triggered average. The conduction velocity has been reported as $v = 8.5$ m/s (Simons et al., 2007). Leaving all other values as in the previous approximation, we arrived at a dipole moment of $p_{\max} \approx 1.5 \mu\mathrm{A} \cdot \mu\mathrm{m}$, yielding an extracellular spike amplitude of ≈ 2.3 µV at the distance of 400 µm, which is of the same order of magnitude as the value (≈ 1 µV) reported by Swadlow and Gusev (2000).

In cases in which the jitter σ_{pulse} is longer, the dipole moment is lower. For example, for pulses evoked by a visual stimulus, the pulse durations can exceed 10 ms (Mitzdorf, 1985; Schroeder et al., 1991, 1998; Self et al., 2013). Using the same parameters as for the thalamocortical projection employed before, but increasing the number of fibers by a factor of 100, increasing the width of the pulse to 10 ms, and increasing the maximal firing rate to 10 Hz, we found that the value of the dipole moment was $p_{\max} \approx 0.018\,\mu\mathrm{A} \cdot \mu\mathrm{m}$, which is two orders of magnitude smaller than in the case of the brief pulse discussed above. However, when we further reduced the conduction velocity to 0.4 m/s, the same 10 ms pulse produced a dipole moment of $0.39\,\mu\mathrm{A} \cdot \mu\mathrm{m}$. Such low conduction velocities can, for example, be found in cortico-cortical projections (Swadlow, 1989).

To summarize, Equation 2.12 quantitatively predicts the contribution of axonal projection zones to the far field EFP, and this prediction matched experimental values in several cases.

2.4 Discussion

Numerical simulations, analytical calculations, and experimental data allow us to show how axonal fiber bundles may contribute to the EFP, and explain how the contributions are shaped by axonal morphology. There are three principal effects of axon bundle structure on the EFP. First, the low-frequency components of the EFP are governed by the densities of bifurcations and terminations and can have a dipolar structure (Figure 2.1 and Figure 2.2A-C). Second, the high-frequency components are governed by the local number

of fibers (Figure 2.2D-F). Third, membrane potentials that change on the same spatial scale as an axonal projection zone through which they propagate generate strong dipole moments in the EFP response (Figure 2.3). At the temporal frequencies that correspond to wavelengths of the size of the projection zone, this leads to dipolar EFP components that are not negligible and exceed the reach of the presumed quadrupolar nature of axonal EFPs.

2.4.1 Relevance to the interpretation of electrophysiological recordings

Our findings relate to the interpretation of a wide range of electrophysiological data in general, and to the estimation of current sources in particular. When performing a typical current source density (CSD) analysis, the local number of fibers cannot be disentangled from membrane current density (Nicholson, 1973; Potworowski et al., 2011). In CSD analysis, the membrane current densities can vary independently with time and location. In contrast, in the case of an axonal fiber bundle considered here, the situation is different: the number of fibers is variable in space, in particular in the terminal zone, but the current sources at different locations are highly correlated because they are caused by propagating action potentials. In the case presented here (Figure 2.5) where axonal action potentials dominate the EFP, it was possible to recover the (normalized) fiber densities and average membrane potentials from the recordings.

Beyond recovering actual fiber densities and membrane potentials, our approach enables the interpretation of CSD results in the presence of axon fiber bundles. For example, the sink and source distribution found in classical CSD analysis of axon bundles (Mitzdorf and Singer, 1978; Mitzdorf, 1985; Mitzdorf and Singer, 1977) shows a dipolar structure in terminal zones, but a conclusive explanation of their origin was not given. Tenke et al. (1993) studied the dipole at an axonal terminal zone in the macaque striate cortex for a fixed point in time, attributing the sinks to the depolarized axon endings, and the sources to the return currents distributed along the axons, while not taking account of additional currents flowing at bifurcations. Our modeling approach provides a novel way of interpreting these findings in terms of actively propagated action potentials in a fiber bundle.

As an example case for a fiber bundle, we recorded from the barn owl nucleus laminaris. Figure 2.4 and Figure 2.5 showed that the low- (<1 kHz) and high-frequency (>2.5 kHz) components exhibit qualitatively different behaviours as a function of recording location relative to the terminal zone. The low-frequency component is a largely stationary phenomenon, while the fine structure of the high-frequency component shifts gradually in space as a function of the axonal conduction velocity (Figure 2.5, see also Carr et al. (2015)). Low-frequency

components have a strong dipole moment, meaning that they contribute to the far-field EFP. Due to the difference in reach, the high-frequency component is most suitable for the study of local phenomena while the low-frequency component bears information about locations more distant from the recording site (Figure 2.3), consistent with findings on non-axonal EFPs (Pettersen and Einevoll, 2008; Łęski et al., 2013).

Note that the low-pass (< 1 kHz) filtered EFP is calculated in a similar way to the LFP, with the exception that the cutoff frequencies used to separate the low- and high-pass filtered EFP are relatively high compared to those used in cortical or hippocampal studies to separate LFP and MUA. We applied these high cut-offs because our modeling and experiments were performed in the auditory brainstem of the barn owl, which operates on very short time scales and, consequently, higher frequencies. We expect other systems operating on slower time scales to have lower optimal cutoff frequencies separating the components. Equation 2.12 indicates how the different spatial and temporal system properties relate to each other to generate a dipole moment.

Dipolar fields are essential for the generation of electrical field potentials at greater distances from the brain. The most prominent of these is the EEG, which is commonly attributed to the dipolar contributions of pyramidal cells (Nunez and Srinivasan, 2006). As originally suggested by Tenke et al. (1993), we propose that axonal contributions might also be relevant in the analysis of these fields. This is particularly true for the auditory brainstem response (ABR), which is closely related to the EEG and involves brain structures that display high degrees of synchrony as well as axonal organization, and are thus ideal candidates for the generation of axonal field potentials visible at long ranges. This would in turn have implications for the interpretation of the ABR in clinical contexts.

The ABR amplitude of the barn owl has been reported to be on the order of 10 µV (Palanca-Castan et al., 2016) while we estimated a contribution of about 3 µV amplitude from the incoming axons in NL alone. This estimate of 30% axonal contribution to the ABR suggests that there may indeed be measurable components due to axons in the ABR, in particular, and the EEG, in general. However, this estimate is crude because it did not take into account the anatomy of the skull except for its size. Future studies based on a more detailed skull model and paired recordings of ABR and EFP should improve our understanding of axonal contributions to the ABR.

We have shown that the EFP in the barn owl NL is consistent with a model of axonal sources. We believe synaptic contributions to be small in this case for the following reasons: The somatic membrane potentials due to synaptic currents are much smaller than the impact of postsynaptic spikes (Ashida et al., 2007; Funabiki et al., 2011). Since postsynaptic spikes contribute little to the EFP (Kuokkanen et al., 2010), we suspect that the synaptic contributions

to the EFP are also small. Furthermore, synaptic EFP contributions would require a spatial separation of currents, which is not possible to achieve in NL because of the symmetrical arrangement of synapses on the spherical NL cell bodies (Carr and Konishi, 1990), meaning that synaptic sources can also not explain a dipolar EFP, and are thus expected to contribute little to the EFP.

2.4.2 Dipolar EFPs in other animals and brain regions

It is interesting to note that a similar dipole-like reversal of polarity as shown here for the barn owl NL has been reported in the chicken NL (Schwarz, 1992) as well as in the mammalian analog to NL, the medial superior olive (MSO) (Mc Laughlin et al., 2010). The phase reversal in this case was modeled based on the assumption that the postsynaptic NL and MSO dendrites with their bipolar morphology generate the dipolar EFP response (Mc Laughlin et al., 2010; Goldwyn et al., 2014). However, in the owl this dipolar morphology of neurons is largely absent (Carr and Konishi, 1990), making dendritic sources unlikely. This differential morphology suggests that similar dipolar field potentials in owls and mammals emerge from different physiological substrates. Such a convergence might point towards an evolutionary pressure favoring a bipolar EFP structure in coincidence detection systems, and indeed, Goldwyn and Rinzel (2016) have proposed a model in which this extracellular potential enhances the function of coincidence detectors through a form of ephaptic interaction. Their approach centers on dendrites and is not directly transferable, but it seems possible that a similar mechanism might arise in the barn owl NL based on axonal EFPs.

The key assumption underlying our modeling of axonal geometries is that there exists a preferential direction of the axon arbor. In many structures this is the case, for example in the parts of the auditory brainstem we studied here. In other brain regions, this tendency is not as prominent, with a spectrum existing between completely directed and undirected growth. More undirected growth would lead to a more diffuse response in the EFP, and eventually to a cancellation of the dipolar field potentials. Cuntz et al. (2010) and Budd et al. (2010) studied the principles underlying the growth patterns of axons and found that the degree of direction in the growth of an axon depends on the balance struck between conduction delay and wiring cost. Optimizing for minimal conduction time leads to highly directed structures while optimizing wiring cost leads to more tortuous, undirected growth. This insight suggests that directed structures - and thus also strong, dipolar EFPs due to axons - may be more prevalent in systems which require high temporal precision in the information processing. This requirement for high temporal precision also aligns well with our model prediction: the dipole moment (Equation 2.12) is maximal when the spatial spread of the activation is equal to the size of the

projection zone, favoring short activation times (< 1 ms) for typical projection zone sizes (1 mm) and conduction velocities (1 m/s).

2.4.3 Relationships to more detailed biophysical models

In the systems we were aiming to describe with our model, for example NL and thalamocortical projections, synaptic boutons are typically small, and we did not model them explicitly. In other systems such as the neuromuscular junction, the synaptic structure can be very large when compared to the axon bundle (Harris and Ribchester, 1979; Katz, 1961; Katz and Miledi, 1965). Such a large junction with an overall length of up to 1 mm was modeled by Gydikov and Trayanova (1986). They found a significant effect of this structure on the EFP. The single flaring and tapering neuromuscular junction in their model had a comparable effect as the entire projection zone in our model, with the flaring causing a similar effect as the bifurcations, and the tapering taking the role of the terminations in our model. Given that synaptic boutons are several orders of magnitude smaller in NL and cortex, we do not expect a strong effect in these systems.

Membrane currents flowing in boutons were studied by Geiger and Jonas (2000), who recorded from the terminals of hippocampal mossy fibers and examined calcium and potassium conductances. The potassium conductances broadened the incoming spikes in an activity-dependent manner. This spike broadening is hypothesised to be mediated by slow inactivation of the potassium channels and takes place on a timescale of > 100 ms, and is thus not relevant to the present study. Spike broadening could be captured in our model by incorporating in Equation 2.12 a σ_{spike} that is variable in time.

The calcium currents reported by Geiger and Jonas (2000) were further quantified by Alle et al. (2009). Calcium currents were temporally overlapping and much smaller in amplitude than sodium and potassium currents. We therefore neglected calcium currents in our model.

Modeling the myelinated compartments, we assumed that they are purely passive and strongly insulated from the extracellular space. However, myelinated compartments do in fact express active conductances, in particular in the paranodal and juxtaparanodal region (Chiu and Ritchie, 1981; Waxman and Ritchie, 1985). Including such a detailed distribution of ion channels in our model could lead to a different shape of the waveform and the spectrum of the EFP of an action potential, possibly similar to the effect described by Ness et al. (2016) for active conductances on dendrites. The conclusions drawn by our model are, however, independent of the precise active conductances and the distribution of myelinated and active segments along the axons because our results rely only on the gross waveform of propagating action potentials,

but not on finer details. Active conductances and capacitive currents in the myelinated segments could affect the shape of the action potential waveform, but do not affect our conclusion about the spatial scaling behaviour of the EFP.

Because of the weak dependence of our results on the gross extracellular spike waveform, our analytical model does not include any intrinsic low-pass filtering as can be derived, for example, for dendritic models (Lindén et al., 2010; Einevoll et al., 2013; for reviews see Buzsáki et al., 2012). The effective additional currents flowing at bifurcations and terminations are, however, low-frequency contributions to the overall membrane currents in our model. Extending our model to treat these currents separately might show whether axons could contribute to the observed $1/f$ scaling of the spectrum of the EFP (Pritchard, 1992).

2.4.4 Conclusion

Axonal projections can contribute substantially to EFPs. Our results quantitatively show how the anatomy of axon terminal zones and the activity in axons determine its frequency-specific far-field contribution to the EFP.

3 Extracellular potentials of dynamic synapses in the barn owl nucleus laminaris

3.1 Introduction

Synaptic currents are commonly assumed to be the major cause of extracellular field potentials (EFPs) in the brain (Buzsáki et al., 2012). This assumption is based on the general understanding of biophysical processes leading to the generation of extracellular potentials and the abundance of synapses in most regions being recorded from (Buzsáki et al., 2012; Nunez and Srinivasan, 2006). However, directly segregating EFPs due only to synaptic currents is a challenge (Ray, 2015) and rarely done, using either pharmacological (Kent and Grill, 2013) or statistical methods (Makarov et al., 2010; Makarova, 2011). Isolating the synaptic component of the EFP is especially difficult in brain regions with a complex architecture (Makarova, 2011) because any experimental intervention to manipulate synaptic currents will likewise modify recurrent and outgoing neuronal activity, in possibly unintuitive ways (Grosser et al., 2014; Gonzalez-Sulser et al., 2012).

The barn owl has a highly specialized auditory system with several features that make it suitable to isolate synaptic contributions to the EFP. First, the earliest binaural nucleus in the auditory processing pathway, called nucleus laminaris (NL), has a well-studied anatomy consisting of a single type of neuron: Afferent axons from the nucleus magnocellularis (NM) form excitatory synapses onto NL neurons, and NL neurons and NM axons are organized to form a tonotopic map (Rubel and Parks, 1975; Carr and Konishi, 1990; Carr et al., 2013). Second, the responses of the NM and NL neurons to acoustic stimuli are well-understood: For tonal stimulation, neurons in both nuclei phase lock to the stimulus; NL neurons also modulate their firing rate in response to changes in the interaural time difference (ITD). Third, the recurrent inhibitory inputs to NL are much slower (Burger et al., 2005; Lu and Trussell, 2000) and are neither frequency-specific (Yang et al., 1999) nor ITD-specific (Burger et al., 2005). We will show that these properties make it feasible to separate synaptic currents from those due to other sources such as the postsynaptic (NL neurons) or presynaptic (NM axons) spiking activity.

The EFP in NL has been the subject of several previous studies. Interestingly, it appears that the EFP is mostly attributable to the incoming axons from NM (Kuokkanen et al., 2010, 2013, 2017; McColgan et al., 2017). We hypothesized that the synaptic contribution to the EFP was small. Experimentally confirming the presence of a small—but significant—contribution from synapses to the EFP would thus support the theory of a predominantly axonal EFP in NL.

Synaptic currents in the auditory system have been studied in owls (MacLeod and Carr, 2012; DeBello and Knudsen, 2004) and extensively in chickens (Kuba et al., 2002; Funabiki et al., 1998; Cook et al., 2003; Oline et al., 2016; Oline and Burger, 2014; Fukui and Ohmori, 2004; Rathouz and Trussell, 1998). In young chicks, the efficacy of synapses formed by auditory nerve fibers in NM are subject to strong short-term depression (STD) (Zhang and Trussell, 1994; Brenowitz and Trussell, 2001). The properties of STD in NM follow a tonotopic gradient (Oline et al., 2016). STD is also present in the intensity-processing pathway of the auditory brainstem in avians, in particular in the cochlear nucleus angularis (MacLeod et al., 2007, 2010; MacLeod and Carr, 2012; MacLeod and Horiuchi, 2011). In NL, evidence for the presence of STD was found *in vitro* by Kuba et al. (2002), who suggested that STD can enhance the direction sensitivity of the postsynaptic neurons. In the avian NL, STD has not yet been studied *in vivo*.

In general, STD has been proposed to play a role in several functional tasks, for example gain control (Abbott et al., 1997), detection of movement direction (Fortune and Rose, 2001), and detection of transients (Abbott et al., 1997; Regehr, 2012; for reviews see Abbott and Regehr, 2004; Klug et al., 2012). These roles could all be relevant in the context of the barn owl auditory system. The tonotopic organization of STD points towards a functional role in signal processing (Oline et al., 2016). STD could also form a building block for more sophisticated adaptive behaviour found in higher brain areas such as "stimulus specific adaptation" (Chung et al., 2002; Gutfreund, 2012). Studies of STD *in vivo* are, however, rare (Mulder et al., 1997; Izaki et al., 2002; Wang et al., 2013). The relevance of data on STD collected *in vitro* has been questioned because chronic and transient activation patterns (Hermann et al., 2009) and calcium concentrations (von Gersdorff and Borst, 2002) can be quite different from those found *in vivo* (for review, see Borst, 2010). Here we quantify, for the first time, STD *in vivo* in the avian NL and show similar values of short-term depression to those observed *in vitro*.

3.2 Materials and Methods

3.2.1 Experimental procedures

The experiments were conducted at the Department of Biology of the University of Maryland. Data were collected from four barn owls (*Tyto furcata pratincola*). Procedures conformed to NIH Guidelines for Animal Research and were approved by the Animal Care and Use Committee of the University of Maryland. Anaesthesia was induced prior to each experiment by intramuscular injection of a total of $8 - 10$ ml/kg of 20% urethane divided into three to four injections over the course of 3 hours. Body temperature was maintained at 39°C by a feedback-controlled heating blanket.

We used iontophoresis to deliver drugs to NL, with methods and concentrations similar to those in previous experiments in the barn owl, chick, and rat inferior colliculus (Feldman and Knudsen, 1994; Sanchez et al., 2007; Zhang and Trussell, 1994). All data reported here were obtained using glass pipette barrels of Carbostar-3 or -4 LT microiontophoresis electrodes (Kation Scientific, Minneapolis, MN). Microelectrode barrels were filled with the AMPA/kainate receptor antagonist 1,2,3,4-tetrahydro- 6-nitro- 2,3- dioxo- benzo[f]quinoxaline-7- sulfonamide (NBQX) (5 mM, pH 9.0; Sigma, St. Louis, MO). NBQX is a highly selective competitive antagonist of both AMPA and kainate receptors, with no significant effect on NMDAR-mediated currents (Randle et al., 1992). Note that although we have demonstrated the presence of AMPA receptor subunits in barn owl NL (Levin et al., 1997) and NMDA receptor subunits in chicken (Tang and Carr, 2007), we cannot exclude the possibility that kainate receptors contribute to some NBQX-sensitive responses. The remaining iontophoresis barrels were filled with 0.5 M NaCl, pH 3.5, for current balancing. Retention and ejection currents were applied to the drug barrels via a dual micro-iontophoresis current generator (WPI, Sarasota, FL, USA). A carbon fiber served as the recording electrode (≈ 0.5 MΩ impedance). In preliminary experiments not reported here, we determined that the owls anesthetized with Xylazine and Ketamine showed effects of NBQX, but we switched to urethane anesthesia for the experiments reported here because of potential interactions between ketamine and NMDA receptors (Lodge and Johnson, 1990) and because urethane provided a more stable plane of anesthesia.

On the day of the experiment, 5 mM NBQX was dissolved in 0.9% NaCl vehicle and filled in one barrel of the electrode. Each barrel of the pipette was connected via a silver wire to a separate channel of the micro-iontophoresis current generator. NBQX was retained using positive currents (+10 nA) and ejected using negative currents (-30 to -60 nA). Because the effect in NL was small, we used single-unit recordings in NM as a positive control. Before recording in NL, each iontophoresis electrode was first tested in NM. We

aimed at an average spike reduction of about 63% following iontophoresis using -30 to -60 nA current, consistent with the NBQX blockade of responses in the inferior colliculus (Sanchez et al., 2007). Such a recording session lasted about 40 minutes, and we typically carried out an entire iontophoresis cycle, with ejection washout, for 1–2 NM units, in order to determine appropriate current settings for the application of NBQX. Driven and spontaneous rates were determined for each NM unit prior to, during, and after iontophoresis of NBQX. We observed a mean reduction in firing rate after 6 minutes of iontophoresis of $56 \pm 12\%$, $n = 7$, for a 10 nA holding current and -60 nA ejection current.

Recordings were made in a sound-attenuating chamber (IAC Acoustics, New York, NY). In all recordings, a AgCl ground electrode (WPI) was placed on the dura near the midsagittal sinus. Electrode signals were amplified, and the line noise was removed with a HumBug line noise eliminator (Quest Scientific, North Vancouver, BC, Canada), which only affects the signals at 60 Hz and its higher harmonics. Amplified electrode signals were passed to an analogue-to-digital converter (DD1, Tucker-Davis Technologies (TDT), Gainesville, FL) connected to a personal computer via an optical interface (OI, TDT). Acoustic stimuli were digitally generated by custom-made software ("Xdphys" written in Dr. M. Konishi's lab at Caltech) driving a signal-processing board (DSP2, TDT). Acoustic signals were fed to miniature earphones via D/A converters (DD1, TDT), anti-aliasing filters (FT6-2, TDT), and attenuators (PA4, TDT). Custom-made sound systems, containing the earphones and miniature microphones were placed into the owl's left and right ear canals. The sound systems were calibrated individually for both amplitude and phase before the recordings. Voltage responses were recorded with a sampling frequency of 48,077 Hz, and saved for off-line analysis. We recorded data from 4 individual owls and 5 distinct recording sessions, with one owl providing data from two recording sessions at the same stereotactic coordinates but two hours apart. ITD responses were determined by playing stimuli with different ITDs. First the ITD with maximum response was roughly determined in a preliminary measurement. Then the full tuning curve was measured by playing stimuli at 11 different ITDs, spaced by 30 μs and centered at the ITD with maximal response. A preliminary attenuation tuning was recorded to select an appropriate sound level. We presented stimuli from 10 to 60 dB sound pressure level (SPL) in intervals of 10 dB SPL and chose one or two attenuations that evoked intermediate responses. We also performed a control recording to estimate the noise levels due to the recording setup, by performing an identical stimulation protocol with the recording electrode in saline. We compared the responses from these control recordings to those from recordings from the main experiments, and found that the instrument noise level accounted for $< 0.1\%$ of the variance.

3.2.2 Data Analysis

Data was analyzed using a custom library (pyXdPhys, https://github.com/phreeza/pyXdPhys) for Xdphys data files. Individual response traces were tagged according to the experimental condition in which they were recorded: NBQX or control, as well as ITD, frequency, and attenuation used for stimulus presentation. For the EFPs shown in Figure 3.1, we selected the ITD and frequency that evoked the maximal response, as judged by the average standard deviation of the traces. If several attenuations were recorded, we chose the loudest one. From this subset, all responses from each condition were aggregated and averaged using the arithmetic mean.

Filtering was performed with Butterworth filters of order 5 with the cutoff frequencies stated in the text. In order to avoid delays introduced by the filters, we applied each filter twice, once in the causal and once in acausal direction.

To test the statistical significance of the difference between the conditions in Figure 3.1, we applied the nonparametric cluster based permutation test described by Maris and Oostenveld (2007). This technique solved the multiple comparisons problem and took into account the temporal correlations inherent in the data. Briefly, the technique consists of randomly assigning conditions to trials, and then calculating the uncorrected significance levels for the differences between these permuted conditions at each time step. Adjacent time steps with significant differences were then grouped into clusters, and an empirical distribution of cluster sizes was tabulated. The cluster sizes were then calculated for the actual NBQX and control conditions, and the significance of the difference was calculated based on the empirical distribution of cluster sizes.

Because the observed effect of NBQX was very small, and the experiments were terminal, we did not perform a separate vehicle control experiment in which the ejection current would have been applied without NBQX in the pipette. We instead tested the diffusive nature of the effect by examining the time-course in Figure 3. For the analysis of the NBQX diffusion in Figure 3.3C, we filtered the individual trial response traces with the same cutoff frequencies (< 1 kHz) as in Figure 3.1C and D and calculated the standard deviation of the filtered trace.

3.2.3 Model of short-term plasticity of synaptic currents

To model the synaptic currents under short-term depression (STD), we used the phenomenological Tsodyks-Markram model with only depression (Tsodyks et al., 1998). In this model, the time dependent synaptic efficacy $x(t)$ (with dimensionless values between 0 and 1) returns to its resting state 1 with time

constant τ_D. Upon an action potential reaching the synapse, a fixed fraction $0 < U < 1$ of the available neurotransmitter is released, causing an increase of the synaptic current $I(t)$. An individual postsynaptic current is modelled as an exponentially decaying function with with time constant τ_s and amplitude A; this function is scaled by the synaptic efficacy x.

Following a simplified approach by Tsodyks et al. (1998), we considered a mean-field approximation of the spike-based model. Spikes were replaced by an average firing rate $R(t)$ that depended on the time t. The model is then governed by the following equations:

$$\begin{aligned} \frac{\mathrm{d}}{\mathrm{d}t}x(t) &= \frac{1-x(t)}{\tau_D} - U\,x(t)\,R(t) \\ I(t) &= \tau_s\,A\,U\,x(t)\,R(t)\ . \end{aligned} \tag{3.1}$$

In preliminary attempts to fit this model to the data, we obtained time constants τ_D in the range of seconds, similar to the value 1.1 s for the slow recovery reported by Cook et al. (2003). However, we could not estimate τ_D reliably from our data because of an approximate degeneracy with the parameters τ_s and A that describe single postsynaptic events; in other words, the fitted values of τ_D, τ_s, and A were quite variable, but this variability was highly interdependent. Because of the nature of our data, i.e. EFPs that reflected the summed activity of many synapses, we could not isolate single events, which would be necessary to estimate τ_s and A.

To overcome these limitations of the STD model, we exploited the fact that firing rates R are expected to be high (> 200 spikes/s) and assumed a large τ_D such that the condition $1/\tau_D \ll UR$ is fulfilled. This assumption allowed us to omit in Equation (3.1) the term x/τ_D, which was considered to be small compared to the term $x\,U\,R$. Introducing the new dynamic variable $y = \tau_D\,x$ and defining $\bar{I} = \frac{\tau_s}{\tau_D}A$, we then could simplify the model as

$$\begin{aligned} \frac{1}{UR}\frac{\mathrm{d}}{\mathrm{d}t}y &= \frac{1}{UR} - y \\ I &= \bar{I}\,U\,R\,y\ . \end{aligned} \tag{3.2}$$

The new dynamic variable y is a scaled (by τ_D) synaptic efficacy. It reaches the steady-state value $\frac{1}{UR}$ with time constant $\frac{1}{UR}$. Both the steady-state value and the time constant do depend on the firing rate R. We emphasize that we have assumed that the new time constant $\frac{1}{UR}$ is much smaller than τ_D, which was confirmed by our fits (see Results). We further note that the steady-state value of the current I is equal to $\bar{I}$, which is independent of both U and R. The time constant $\frac{1}{UR}$ for the decay of I, however, does depend on U and R.

Let us discuss a generic example to illustrate the time course of I resulting from the solution of the differential equation (3.2). We consider a population

of synapses that have been driven with a constant rate R_0 for a long time. The constant average steady-state current is then $I = \bar{I}$. Changing the firing rate from R_0 to R_1 in a step-like manner at $t = t_0$ results in a time-dependent current

$$I(t) \quad = \begin{cases} \bar{I} & t < t_0 \\ \bar{I} + \bar{I}\frac{(R_1 - R_0)}{R_0} e^{-UR_1(t-t_0)} & t \geq t_0 \end{cases} . \tag{3.3}$$

This means that at time t_0 the current changes by the amount $\bar{I}(R_1 - R_0)/R_0$, which is proportional to the relative change in the firing rate. Then the current I exponentially decays back to the steady state $\bar{I}$ with the time constant $\frac{1}{UR_1}$, as mentioned above, meaning that the decay depends only on U and the new firing rate R_1, but not on the firing rate R_0 before the step.

In the simplified STD model in Equation (3.2), we could combine in $\bar{I}$ the three variables τ_s, τ_D, and A because they do not occur independently in the model. This property means that they are fully degenerate, i.e., they cannot be determined independently, which is related to their approximate degeneracy in the more complex STD model in Equation (3.1).

Because extracellular potentials in the brain are proportional to a weighted sum of the membrane currents, here we modeled the extracellular potential as a linearly scaled version of the membrane current I. This changed the unit of the variable $\bar{I}$ from a current to a potential. From I we also subtracted the steady-state value $\bar{I}$ because we could not measure DC offsets in the EFP.

In order to fit this simplified model of STD in Equation (3.2) to the experimentally observed EFP traces, we determined the values for U and $\bar{I}$ as well as the time course of $R(t)$ by minimizing the mean square difference between model response and the traces. To fit the firing rate profile $R(t)$, we modeled it as a piecewise linear function with a resting firing rate R_0, a driven firing rate R_1, and a fixed (for each recording location) onset delay $t_0 = 8 \pm 6$ ms with respect to the acoustic stimulus, which accounted for neural and cochlear conduction delays (McColgan et al., 2014; Köppl, 1997b). Note that this range is relatively broad compared to measurements of click latencies (Wagner et al., 2009; McColgan et al., 2014). Since we intended to fit only the low-frequency (< 1 kHz) responses in the EFP, we did not take into account phase locking and the oscillation of $R(t)$ with the stimulus frequency, which was always in the kilohertz range. After a delay t_0 following stimulus onset, the firing rate ramped up to R_1 with a ramp duration of 5 ms, as in the acoustic stimulus. After the duration of the stimulus (200 ms) and including again the delay t_0, the rate ramped back down to R_0 with the same slope. We did not take into account the overshoot of the firing rate at the onset, as observed in MacLeod et al. (2010) because this additional feature did not increase the quality of the fit.

In order to disambiguate between parameter combinations that have similar mean square error values, we performed the following regularizations, based on prior knowledge from the literature (Köppl, 1997b; Peña et al., 1996). We added a penalty of $(R_0 - 200\ \text{Hz})^2$ for values of $R_0 > 200$ Hz, and $(R_1 - 400\ \text{Hz})^2$ for values of $R_1 < 400$ Hz. Both regularization terms were scaled and converted to appropriate units by a factor of $\lambda = 0.1 \left(\frac{\text{mV}}{\text{kHz}}\right)^2$.

3.2.4 Model of spatial responses

We simulated the spatial structure of the extracellular potential due to synaptic currents by implementing the two-compartment model of an NL neuron by Ashida et al. (2007) in the NEURON simulator. The model neuron consisted of a spherical somatic compartment with diameter 25 μm, connected to a myelinated axon initial segment (AIS) of length 50 μm and diameter 2 μm, and the first node of Ranvier, which was 2 μm long and had a diameter of 2 μm. After the first node of Ranvier we added a sequence of 10 identical myelinated segments and nodes of Ranvier in alternating order, which were not included in the model by Ashida et al. (2007). Nodes and myelinated segments had a length of 2 and 50 μm, respectively, and both had a diameter of 1 μm. All segments formed a straight line, which was aligned with the vertical axis in Figure 3.5B. Only the nodes of Ranvier contained active conductances, and we used the same conductances described by Ashida et al. (2007). The capacitance of the myelinated compartments and the AIS were set to 0.02 $\mu\text{F/cm}^2$.

To simulate a synaptic input from an NM axon terminal onto the NL soma, we induced a time-dependent conductance in the somatic compartment. The reversal potential of this postsynaptic current was 0 mV. The resulting excitatory postsynaptic current (EPSC) that we induced in the soma had the shape of an alpha function with a time constant of 0.1 ms and a maximum amplitude of 3.6 nS. This simulated EPSC was used in the LFPy package (Lindén et al., 2014) to calculate the extracellular potential at various locations. We chose the recording locations at intervals of 100 μm and in parallel with the axonal trunk, offset at a distance of 50 μm.

In order to simulate the spatial profile of STD-related currents for 200 ms tonal acoustic stimulation, we simulated the resulting synaptic current as described in Equation (3.2). We normalized these responses by dividing by the total charge transfer (area under the EPSC). Convolving the resulting normalized curves with the spatial responses for a single EPSC resulted in the desired spatial response to the entire stimulation. Scaling these responses up by the number of synapses per neuron $N = 300$ (Ashida et al., 2013) and the number of neurons in NL activated by the stimulation $M = 2000$ (about 20% of the

entire population, as reported by Kubke et al. (2004)) gave us the estimated response when recording the population response in NL.

3.2.5 Linear response decomposition

To separate the NBQX and ITD related effects in the response, we devised a linear model to fit the data (Draper and Smith, 2014). We began by considering each sample of each single-trial trace (not averaged or filtered) as y_{ij}, where i enumerated the number of the sample within the trace, and j the number of the trace. Each trace consisted of 19230 samples (sampling rate 48077 kHz, 400 ms time interval). The example shown in Figure 3.4 consisted of 1375 traces. We then introduced two regressors: the first regressor for the NBQX condition, c_j, which was equal to -1 if NBQX was being applied during trial j, and $c_j = 1$ otherwise. As seen in Figure 3.3, the effect of NBQX is gradual, and not binary. We are thus estimating the average effect of NBQX over the entire duration of application. The second regressor was the presented interaural time difference τ_j in trial j. Due to the sinusoidal stimulation, as a first approximation, the ITD tuned responses at time t_i of the i-th sample are linear in $\sin(2\pi f(t_i + \tau_j))$ and $\cos(2\pi f(t_i + \tau_j))$, where f is the stimulation frequency. The linear regression model including interaction terms was thus

$$\begin{aligned}\hat{y}_{ij} = {} & A_i c_j \\ & + B_i^{\sin} \sin(2\pi f(t_i + \tau_j)) + B_i^{\cos} \cos(2\pi f(t_i + \tau_j)) \\ & + C_i^{\sin} c_j \sin(2\pi f(t_i + \tau_j)) + C_i^{\cos} c_j \cos(2\pi f(t_i + \tau_j)) \\ & + D_i\end{aligned} \tag{3.4}$$

with coefficients A_i, $B_i^{\sin}$, $B_i^{\cos}$, $C_i^{\sin}$, $C_i^{\cos}$, and D_i to be fitted. The amplitudes of the ITD-modulated components were then calculated as $B_i = \sqrt{(B_i^{\sin})^2 + (B_i^{\cos})^2}$, and analogously for C_i, which represent the amplitudes of the interaction between the ITD-related and the NBQX-related components. The coefficients A_i, B_i, and C_i were then plotted in Figure 3.4A, B, and C, respectively. The coefficients D_i were not plotted because they are not attributable to a single putative source of the neurophonic (see examples below).

The significance of the coefficients was determined by means of a two-sided t-test based on the standard deviation of the coefficients, to which a Bonferroni correction was applied for the number of coefficients that were fit. In the case of B_i and C_i, the maximum of the two p-values on the cosine and sine terms was used. We chose this conservative measure in order to avoid false positives from correlations between the coefficients.

This kind of model is able to separate components with different response profiles to ITD and NBQX. This can be understood by examining the best fit results to three idealized cases.

First, if a response y is not at all affected by NBQX, which we assume for the contributions from NM axons, then we expect that A_i and C_i will all be zero. As shown by Kuokkanen et al. (2013), the axonal part of the average neurophonic at a fixed location, when only the delay of the contralateral ear is modified to produce an ITD, can be written as $y_{ij} = a_I \sin(2\pi f\,(t_i + \Delta t_I)) + a_C \sin(2\pi f\,(t_i + \Delta t_C + \tau_j))$ with free parameters a_I, a_C, Δt_I, and Δt_C. This can be rewritten as

$$\begin{aligned} y_{ij} = {} & a_I \sin(2\pi f\,(t_i + \Delta t_I)) + a_C \cos(2\pi f \Delta t_C) \sin(2\pi f\,(t_i + \tau_j)) \\ & + a_C \sin(2\pi f \Delta t_C) \cos(2\pi f\,(t_i + \tau_j)) \ . \end{aligned} \tag{3.5}$$

By comparison of the coefficients in Equations (3.4) and (3.5), we can see that $A_i = 0$, $B_i^{\sin} = a_C \cos(2\pi f \Delta t_C)$, $B_i^{\cos} = a_C \sin(2\pi f \Delta t_C)$, $C_i^{\sin} = C_i^{\cos} = 0$ and $D_i = a_I \sin(2\pi f\,(t_i + \Delta t_I))$. This means that $B_i = a_C$, which was exactly the part of the neurophonic modified by ITD.

Second, we consider the case of a purely NBQX-dependent response that is not modulated by ITD, and we expect that only the A_i and D_i will be non-zero. This would be the case for the average synaptic contributions at all frequencies different from the frequency of a sustained tonal stimulus (Kuokkanen et al., 2010). For example, we can model the synaptic component as $y_{ij} = a_{\mathrm{syn}}(1 + c_j)/2$, meaning that it has the amplitude a_{syn} when NBQX is being applied, and zero otherwise. This can be rewritten as $y_{ij} = a_{\mathrm{syn}}/2 + a_{\mathrm{syn}} c_j/2$. By comparison of the coefficients with Equation (3.4), we can see that this corresponds to $A_i = D_i = a_{\mathrm{syn}}/2$ and $B_i = C_i = 0$.

Third, a response that is dependent on ITD and whose amplitude is modified by NBQX is the only case which would result in non-zero C_i. For example, we expect that the contribution of NL neurons' spiking to the neurophonic is both NBQX and ITD dependent.

Because of the linearity of the model in Equation (3.4), components of the neurophonic that have the idealized properties of ITD- and NBQX-dependence described in the previous three paragraphs can be combined, and also decomposed again in the fit (Draper and Smith, 2014). However, since all components can contribute to D_i, we cannot disentangle these contributions. We can thus draw conclusions about different contributions with the properties discussed above from the fit of the coefficients A_i, B_i, and C_i.

3.2.6 Diffusion simulation

We based our simulations of diffusion from an iontophoretic injection on the calculations by Nicholson and Phillips (1981) and Crank (1979). They showed that for an iontophoretic point source activated at time $t = 0$ with a flow rate q and a diffusion coefficient D in a homogeneous, infinite medium, the concentration C at a distance r from the point source is $C(r,t) = \frac{q}{4\pi Dr}\mathrm{erfc}\left(\frac{r}{2\sqrt{Dt}}\right)$ where erfc is the complementary error function. Switching off the iontophoretic source was then simulated by adding a source with opposite flow rate $-q$ at the time of switching off. Note that D and q are taken to be effective values, and they might differ from their free-space equivalents due to porosity and tortuosity of the tissue. The value for the flow rate is given by $q = nI_p/F$, where $I_p = 60$ nA is the current flowing through the pipette, F is the Faraday constant, and $n = 6.5 \cdot 10^{-4}$ is the transport number, which determines the fraction of the current that is carried by the NBQX ions. We determined the value for n empirically, which is possible because it linearly scales the response. We chose the effective diffusion coefficient $D = 2 \cdot 10^{-6}\frac{\mathrm{cm}^2}{\mathrm{s}}$ as determined by Pararas et al. (2011) for the closely related AMPA-receptor antagonist DNQX.

In order to calculate the effective remaining synaptic currents at a given concentration, we used the results from Zhou and Parks (1991) where the efficacy of NBQX was determined in the chick NL. We approximated their results with an IC_{50} curve, with the percentage of current remaining given by the expression $50\% - 50\% \cdot \mathrm{erf}\left(k \cdot (\log_{10}(C) - \log_{10}(\mathrm{IC}_{50}))\right)$ with the slope factor $k = 3$ and the half-activation value $\mathrm{IC}_{50} = 1.4$ μM.

The effective contribution of a population of synapses was calculated by approximating NL as a sphere of radius 1 mm in which synapses were homogeneously distributed. This simplified NL was embedded into an infinite homogenous medium into which the NBQX could diffuse. Analogous to the calculation made by Kuokkanen et al. (2010), we assumed that the amplitudes of the synaptic responses scale as $1/r^2$. Because the number of synapses in a thin spherical shell with radius r is proportional to r^2, the overall contribution to the response of each concentric shell is then independent of r. This feature resulted in the population response being an arithmetic average over the single-synapse responses at all radii from 0 to 1 mm.

3.3 Results

Using pharmacological methods *in vivo* in anesthetized barn owls, we identified a distinct component of the extracellular field potential (EFP) in the nucleus laminaris (NL) that can be attributed to synaptic activity. We isolated this synaptic component using synaptic blockers, and show how its shape may be

explained using short-term depression (STD).

3.3.1 Application of NBQX reveals a small synaptic contribution to the EFP

In order to understand the contributions of synaptic currents to the EFP in NL, we used pure-tone burst stimuli (200 ms duration). Stimulation evoked the well-known EFP response in NL, called the neurophonic potential (Figure 3.1A-C). The wideband responses (Figure 3.1A) showed transients that were consistent with findings from previous studies of the neurophonic (Carr and Konishi, 1990; Kuokkanen et al., 2010). To isolate the characteristic frequency-following part of the neurophonic, which is prominent for tonal stimuli $\lesssim$ 9 kHz in the barn owl (Köppl, 1997a), we applied a high-pass filter with a cutoff of 1 kHz to the responses (Figure 3.1B). The resulting responses consisted mainly of the phase-locked, frequency-following component associated with the neurophonic, and are mainly attributable to presynaptic spikes from NM afferents (Kuokkanen et al., 2010, 2013, 2017; McColgan et al., 2017).

While the high-frequency component of the response is mostly due to axonal contributions, the low-frequency component is also expected to contain contributions from synapses (Kuokkanen et al., 2010). Synapses should contribute more to the low-frequency component because they can be described by alpha functions, which are low-pass filters (Funabiki et al., 2011). Therefore, in what follows, we will focus more on the low-frequency component of the neurophonic in order to identify a synaptic contribution. To do so, we applied a low-pass filter, again using a cutoff of 1 kHz (Figure 3.1C). This component showed no phase locking, but had transients at stimulus onset and offset, with a slower decay back to the baseline after both.

To separate the contribution of synapses to the neurophonic from other sources, we iontophoresed the AMPA-receptor antagonist NBQX inside NL in urethane anesthesized birds, for typically several minutes (see Materials and Methods for details). In particular, we alternated the application of NBQX with periods of similar durations in which the flow of NBQX was stopped, resulting in wash out of NBQX. We called the blocks of drug application the "NBQX condition" (orange traces in Figure 3.1A-C), and the block before and after NBQX application the "control condition" (blue traces in Figure 3.1A-C). Comparing the averaged wideband responses for these two conditions (Figure 3.1A), we found that the gross structures of the neurophonic were quite similar, which indicated that synaptic contributions were small. Each experiment contained either 2 or 3 control and NBQX blocks each.

To further isolate and quantify differences between the control and NBQX conditions, we first examined the high-pass filtered component (Figure 3.1B).

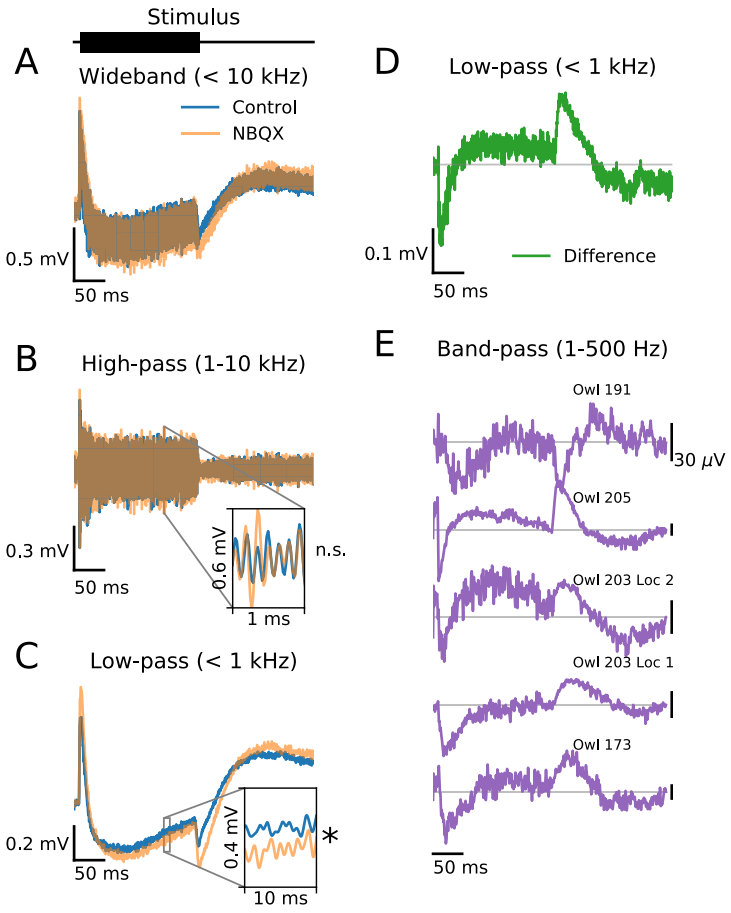

Figure 3.1: NBQX alters EFP responses in nucleus laminaris. (**A**) Tone-burst stimulus (200 ms duration, 6.8 kHz frequency, black bar) and wideband (1 Hz–10 kHz) responses averaged over all trials in the control condition (blue) and during NBQX application (orange; overlap in brown). (**B**) High-pass (> 1 kHz) filtered responses from (A) (same color code). Inset shows a 1 ms excerpt for detail. (**C**) Low-pass (< 1 kHz) filtered responses from (A) (same color code). Inset shows a 10 ms excerpt for detail. Significance level from Bonferroni-corrected two-sided t-test of difference between the curves indicated beside insets in (B) and (C); n.s.: not significant, *: $p < 10^{-3}$. (**D**) Difference between the low-pass filtered responses in NBQX and control conditions shown in (C). (**E**) Band-pass (1–500 Hz) filtered differences between NBQX and control conditions from five recording locations in four owls. We note that the displayed amplitudes of voltages traces are identical but the voltage scales (vertical black bars indicate 30 μV) are different.

The mean responses were similar between control and NBQX conditions, and we found no statistically significant difference between them when applying a cluster-based permutation test (see Materials and Methods, and Maris and Oostenveld (2007)). In contrast, for the low-pass filtered responses, control and NBQX conditions differed (Figure 3.1C). This difference was confirmed with the cluster-based permutation test, which found the means to be different with $p < 10^{-3}$.

In the low-pass filtered responses, the difference between the NBQX and the control conditions revealed synaptic and NL spiking contributions to the neurophonic (Figure 3.1D). We will focus on the low-frequency component, even though synapses should also contribute (but to a lesser relative extent) to higher frequencies. In the following sections, we will show why NBQX-related differences are likely to be almost entirely synaptic, and not due to NL spiking. The putative synaptic contribution in Figure 3.1D had a characteristic shape with a fast rise (< 5 ms) at the beginning of the stimulus presentation, followed by a slower decay back to the baseline. At the end of stimulus presentation, there was another fast transient with opposite direction from the one at stimulus onset, once again followed by a slower decay.

These transient responses, as observed in the difference between NBQX and control conditions, had opposite polarities at the onset and offset of the tone burst, and were robust and repeatable, with similar shapes found in five recording locations in four owls (Figure 3.1E). To make the comparison across owls easier, we normalized the plotted response amplitudes and applied a slightly tighter band-pass filter (1–500 Hz). All responses shared the same double-transient shape.

The putative synaptic contribution to the EFP was very small, explaining only 0.6% of the variance observed across all repetitions and samples. In contrast, the average response over all trials for each sample (regardless of NBQX state) explained 34.1% of the observed variance. Most of the remaining variance was explained by the changes in the presented ITD (see “Linear response decomposition” section in Materials and Methods) and the stochastic nature of NM firing.

NBQX can have a seemingly paradoxical effect on the magnitude and the sign of the slow transients of the neurophonic: in the displayed example (Figure 3.1A and C) the response magnitude in the NBQX condition was larger than in the control condition. This paradox is resolved by taking into account that the neurophonic contains large components other than those generated by synaptic currents. For example, incoming axonal currents can result in a neurophonic component that has a different polarity than the synaptic component (McColgan et al., 2017). This opposite polarity of axonal and synaptic contributions can result in either a net increase or a net decrease of the summed response amplitude when the synaptic contribution is removed

by NBQX. We also note that the low-pass filtered transients in Figure 3.1E (compare the first to the other four examples) can have opposite polarities; we will return to this feature at the end of the Results.

3.3.2 A simple model of short-term plasticity explains the time course of synaptic contributions to the EFP

Inspired by previous *in vitro* experiments and modeling in the chick (Kuba et al., 2002; Cook et al., 2003), we hypothesized that synaptic currents in NL may be subject to short-term depression (STD), and that the time course of the low-pass filtered synaptic contributions to the EFP identified in Figure 3.1D-E could be explained by a model of STD (Abbott et al., 1997; Tsodyks et al., 1998; Tsodyks and Markram, 1997). To test this hypothesis, we implemented a mean-field model of the currents flowing at such a synapse, based on a single reservoir of neurotransmitter that gets partially released on every incoming action potential and gradually replenishes over time (see Materials and Methods for details). The free model parameters were the fraction U of available transmitter released at each event, the firing rate R (here: the resting (R_0) and driven (R_1) firing rates of NM), and the scaling factor $\bar{I}$ of the response. Interestingly, the exact value of the putative slow time constant τ_D for the recovery of the synaptic reservoir (estimated by Cook et al. (2003) to be 1.1 s) was not necessary to explain the time course of synaptic contributions to the EFP. Instead, steady states were reached exponentially in the model with time constant $\frac{1}{UR} \approx 14 - 21$ ms; see Materials and Methods for details.

This model of STD fit the observed time course of the putative synaptic potentials well (Figure 3.2A). The residuals of the model fit (Figure 3.2B) were small (50.1% explained variance in the example shown, 40 ± 14% across all examples) and contained a low-frequency (<100 Hz) component of unknown origin (see Discussion) and a high-frequency (>200 Hz) noise that can be attributed to the stochastic nature of NM firing activity. Instrument noise accounted for a very small amount (< 0.1%) of the variance.

In the example shown in Figure 3.2, the inferred firing rate profile of the input from NM had a resting firing rate of 240 spikes/s and a driven rate of 380 spikes/s (Figure 3.2C). Across all examples, the firing rates were 220 ± 16 spikes/s at rest and 386 ± 9 spikes/s during stimulation. This profile is in the same range as suggested by the literature (from 119.3 to 291.7, mean 219.4 spikes/s at rest (Köppl, 1997b) and 423 ± 113 spikes/s during stimulation (Peña et al., 1996)).

We found that including spike-rate adaptation of NM units at the onset of the firing rate profile (Figure 3.2C) did not improve the fit. We hypothesized that this lack of improvement was due to the short time constant (<10 ms) of spike-

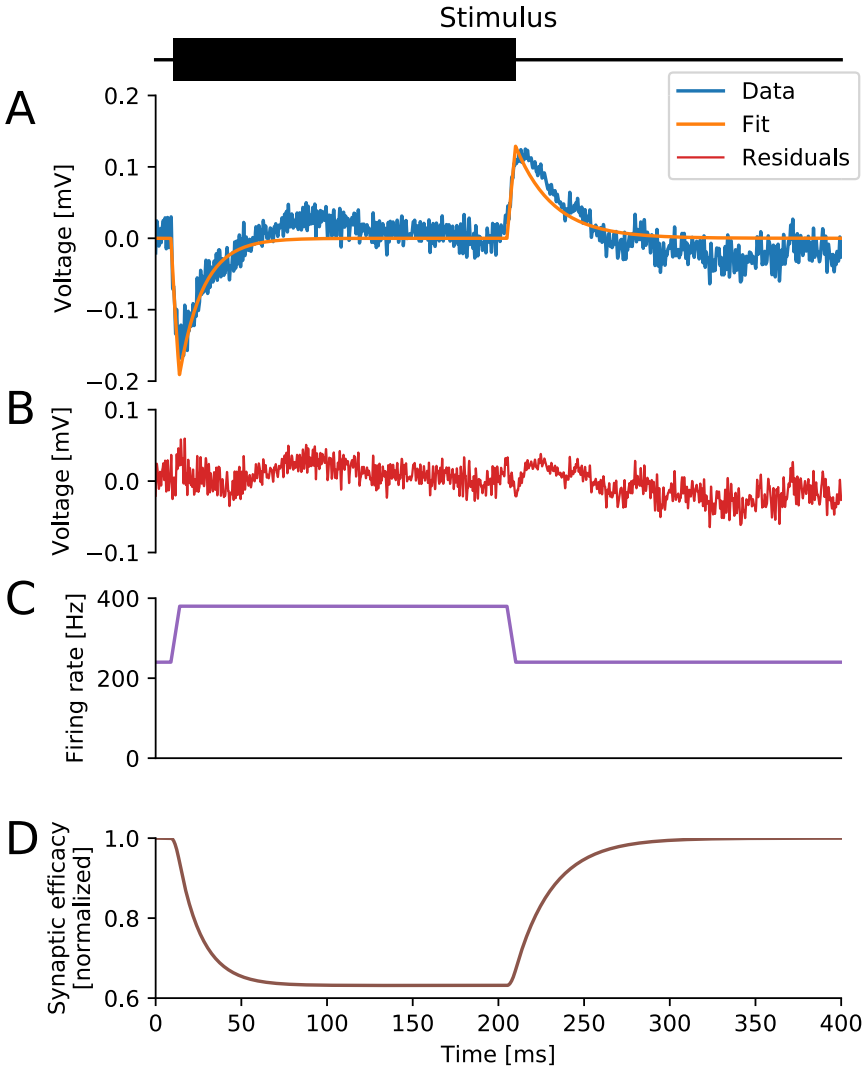

Figure 3.2: Model of short-term depression (STD) fits synaptic contributions to the EFP. (**A**) Auditory stimulus (*top*, same as in Figure 3.1) and extracellular correlate of the putative synaptic currents (*bottom*, blue, same as in Figure 3.1D) compared with a model of synaptic STD (orange, see also Material and Methods). (**B**) Residuals of the fit in (A). (**C**) Firing-rate profile implied by the fit in (A). (**D**) Normalized synaptic efficacy (value 1 corresponds to steady-state efficacy for spontaneous input rate) in response to the stimulus as implied by the fit in (A).

rate adaptation in our experimental conditions. Such short time constants are consistent with the findings of MacLeod et al. (2010), who reported a value of 8 ms.

The utilization factor of the STD process was fit as $U = 0.19$ in the example shown in Figure 3.2, and was $U = 0.10 \pm 0.06$ across all examples. The value for the scaling factor $\bar{I}$ was 0.43 mV in the example shown, and 0.18 ± 0.15 mV across all examples.

Since the model synapses received an input with a high spiking rate even during rest, they probably never reach a state in which their vesicle pool is full. Because we could not estimate the synaptic efficacy in the fully recovered state from the data, we normalized the synaptic efficacy to its steady-state value at resting firing rate (value 1 in Figure 3.2D) and showed the dynamics of change with respect to this baseline.

In the example shown in Figure 3.2, during stimulation the synaptic efficacy approached the fraction 0.63 of its resting state, which equals the ratio of the firing rates $R_0 = 240$ spikes/s and $R_1 = 380$ spikes/s (see Material and Methods for details). Steady states were reached with time constants $\frac{1}{UR}$ (see Materials and Methods for details). After the onset of the acoustic stimulus, the steady state was reached with the time constant $\frac{1}{UR_1} = 14$ ms, and after the offset of the stimulus the synaptic efficacy decayed back to its resting value with the slightly longer time constant $\frac{1}{UR_0} = 21$ ms. These time constants match the time constant of fast recovery (15 ms) reported by Cook et al. (2003). Beyond the predicted two different fast recovery time constants at onset and offset, the different magnitudes of the transients in Figure 3.2A were also reproduced by the model: the amplitude (including the sign) of the transient of the EFP was predicted to be proportional to the relative difference of the firing rates (see Materials and Methods for details): at the onset we have $(R_1 - R_0)/R_0 = 0.58$, and at the offset we find $(R_0 - R_1)/R_1 = -0.37$, which is smaller in amplitude and opposite in sign.

We thus concluded that the nature of the observed component can be explained by STD, and that the system operates in a highly depleted regime.

3.3.3 Diffusion of NBQX in nucleus laminaris is consistent with the slow time course of the synaptic contribution to the EFP

To further test whether the observed changes in the putative synaptic contributions to the EFP were consistent with the effects of NBQX iontophoresis, we considered the diffusion of NBQX in the tissue surrounding the pipette. We calculated the time course of the expected concentration of NBQX in our experimental setting where iontophoresis of NBQX was switched on and off repeatedly. The concentration of NBQX at a given distance from the tip of the

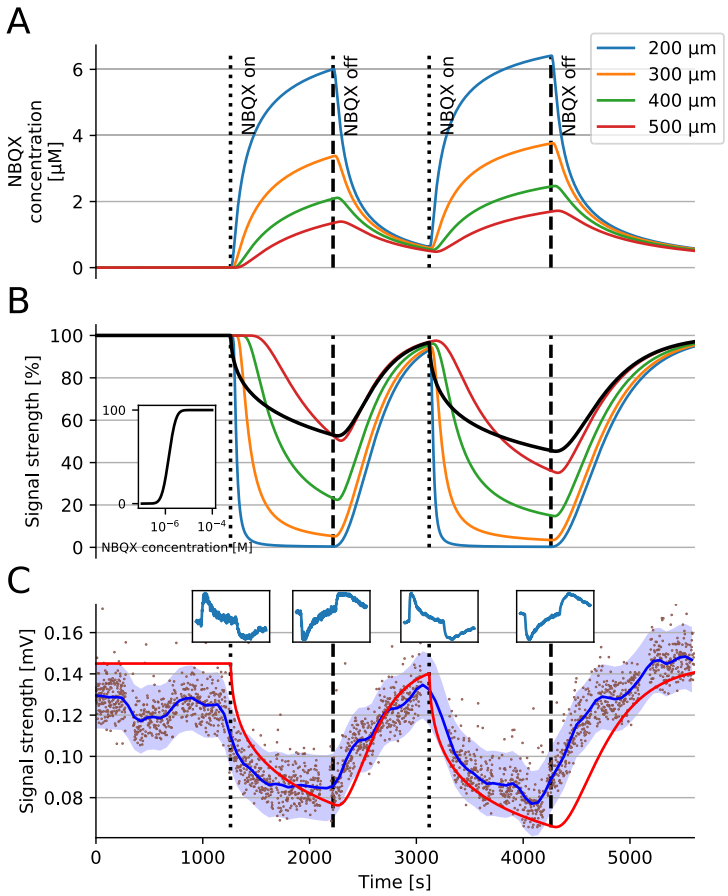

Figure 3.3: Diffusion of NBQX explains time course of amplitudes of synaptic contributions to the EFP. (**A**) Simulated NBQX concentrations for different distances (indicated in legend) from an iontophoretic point source. Switching between ejection (NBQX on) and holding (NBQX off) currents indicated by dotted and dashed lines, as labeled. (**B**) Simulated synaptic current amplitudes (signal strengths) for a synapse at given distances (colors as in A) from the iontophoretic point source. Signal strengths were obtained by applying the dose-response curve (inset) to the concentrations shown in (A). The black line shows the predicted signal assuming a homogeneous distribution of synapses in NL. (**C**) Response amplitudes (signal strengths in mV) in the frequency band associated with synaptic currents (< 1 kHz) during application of NBQX. Brown dots show individual trials in an experiment, and the blue line is the average over time (sliding window width 500 s), along with the 95% confidence interval (from the standard deviation in the sliding window) in light blue. Iontophoresis switching times indicated by dotted and dashed lines as in A and B. Insets show the differences between average stimulus responses for two consecutive blocks, equivalent to Figure 1D. The red line shows the modeled signal (black line in B) scaled to a maximum amplitude of 0.145 mV.

pipette can be modeled by solving the diffusion equation (see Materials and Methods). Because the distances of the synapses from the tip of the pipette are unknown, we first calculated NBQX concentrations for various distances, for example from 200 to 500 μm (Figure 3.3A), which confirmed that NBQX could reach large fractions of NL within the duration ($<$ 1000 s) of NBQX application. Using values for the effectiveness of NBQX on synaptic currents in the chick NL (Zhou and Parks, 1991) (inset in Figure 3.3B), we were then able to predict the amount of remaining synaptic currents at a given concentration of NBQX. Transforming the time course of the concentrations in Figure 3.3A with this dose-effect function yielded a predicted (normalized) synaptic current for a synapse at a given distance from the electrode (Figure 3.3B). Assuming a homogeneous distribution of synapses in a sphere with a radius of 1 mm around the recording electrode and an $1/r^2$ scaling of the contribution of a given synapse at distance r from the pipette and the recording electrode, we calculated the population signal (black curve in Figure 3.3B) by averaging the signal strengths for distances up to 1 mm (see Materials and Methods for details).

We then compared the predicted progression of synaptic current amplitude during NBQX application with the experimental data. By taking the average amplitude of the EFP signal in the frequency band ($<$ 1 kHz) previously identified in Figure 3.1 to be related to the NBQX effect, we were able to estimate the magnitude of the signal strength for every stimulus presentation (a 200 ms tone burst) individually. Figure 3.3C shows how the signal strength evolved over time. The time course of the experimentally measured signal strength has a shape similar to the predicted population signal if its voltage scales were matched (red curve in Figure 3.3C). In both the experiment and the model, we observed a rapid fall of the signal amplitude when the NBQX injection is switched on, followed by a saturation within 10 minutes and a slower recovery after switching off the NBQX injection. The model could not account for a slow drift of the signal strength.

To test if the effect observed in Figure 3.1 is reliable, we calculated the difference in response between consecutive control and NBQX conditions. The resulting curves, calculated in the same way as Figure 3.1D, showed the same shape as those seen in Figure 3.1, with the differences from a NBQX to a control block having the opposite sign, as expected. This led us to conclude that the effect was indeed reliable, and washed out during each control block.

The observed time course of synaptic contributions to the EFP are thus consistent with a diffusive spread of a synaptic antagonist, as expected for an iontophoretic application of NBQX. This consistency serves as a further control that the observed effect is indeed due to a blockage of synaptic currents by NBQX, and not an experimental artifact.

3.3.4 Firing of NL neurons does not contribute significantly to the observed responses

NBQX is an AMPA-receptor antagonist, and neurons in NL receive their excitatory input mainly through AMPA synapses (Raman et al., 1994; Kuba et al., 2002; Zhou and Parks, 1991), with possibly small amounts through other receptors such as kainate and NMDA (Zhou and Parks, 1991). We expect that the application of NBQX reduces the postsynaptic firing activity of NL cells. This changed firing of NL neurons potentially contributes to changes in the EFP between NBQX and control conditions, which we have analyzed in the previous sections. This NL firing component hampers the interpretation of NBQX related effects in terms of synaptic currents. However, from previous analyses (Kuokkanen et al., 2010, 2013, 2017) we know that the number of independent sources needed to generate the observed EFP greatly exceeds the number of NL neurons that are close enough to the recording electrode, and thus we expect their contribution to the EFP to be small. In what follows, we nevertheless performed an additional data analysis to exclude a significant contribution of the spiking of NL neurons to the EFP.

In order to extract the contribution of postsynaptic firing of NL neurons from the EFP, we took advantage of the binaural nature of the NL system. NL neurons are tuned to specific interaural time differences (ITDs), which enabled us to manipulate their firing rate during stimulation by varying the ITD of the binaural stimulus. Because there is a map of ITD (Carr et al., 2013), the NL neurons close to the electrode may contribute to an ITD-tuned component of the neurophonic beyond the ITD-tuned component due to linear summation of the two monaural input-related components (Kuokkanen et al., 2013). Such an interaction between NBQX and ITD would indicate a postsynaptic NL firing component.

To measure the ITD-related modulation of the difference between NBQX and control conditions, we recorded responses at varying ITDs (see Materials and Methods) and fit a linear model to the unfiltered responses like the one shown in Figure 3.1A (see Materials and Methods for details). The ITD component of the model was fit to the typical sinusoidal ITD response pattern (Carr and Konishi, 1990; Kuokkanen et al., 2013), and we here report the amplitude of this sinusoidal modulation. This linear model had four groups of coefficients: the purely NBQX-modulated component, the purely ITD-modulated component, the interaction between ITD and NBQX modulation, and the unmodulated component, which was neither affected by ITD nor by NBQX. Because of the way NL is structured, a significant interaction-related component would indicate a contribution to the EFP of postsynaptic NL firing activity, which depends on ITD.

The resulting model coefficients are shown in Figure 3.4. For each coefficient,

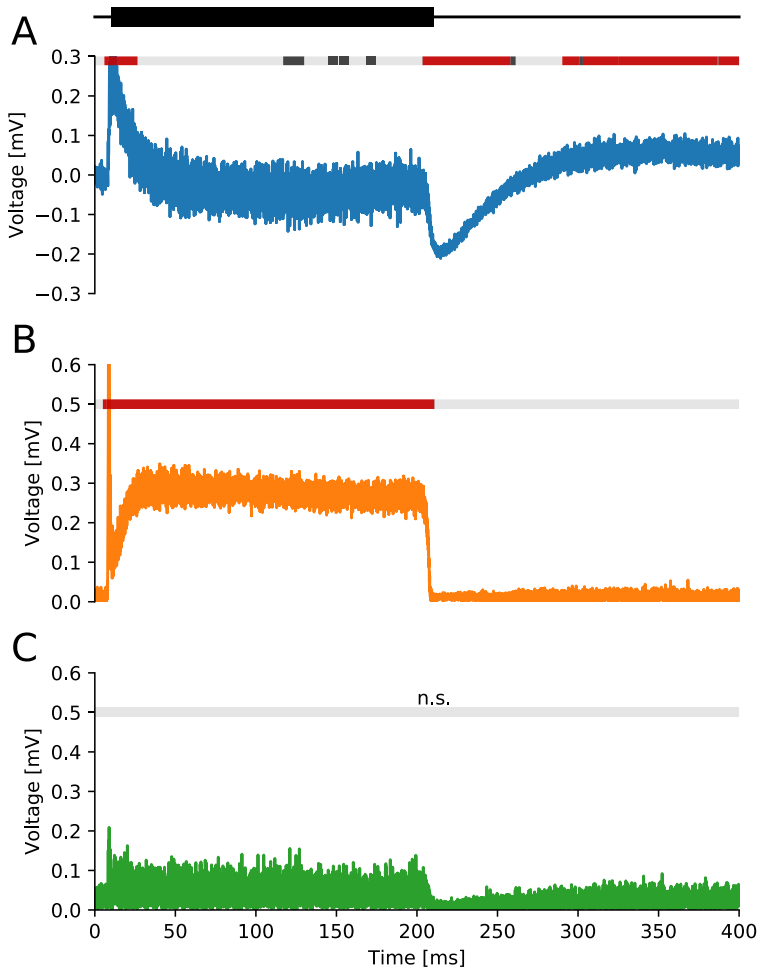

Figure 3.4: Decomposition of EFP responses into NL-neuron dependent (ITD related) and synapse dependent (NBQX related) parts. (**A**) Voltages of the purely NBQX-related component of the linear response model; see Materials and Methods for details. The colors of the horizontal bar indicate the parts with significant responses with $p < 0.05$ (dark gray) and $p < 10^{-3}$ (red), determined with a cluster-based permutation test. Stimulus-presentation interval (200 ms) indicated by black bar at top. (**B**) Amplitude of the ITD modulation in the linear response model. Significance of the coefficients indicated as in (A). (**C**) Amplitude of the interaction between the NBQX- and ITD-related parts in the linear response model. Interaction-related components were not found to be significant at any time point.

we calculated the Bonferroni-corrected probability of the null-hypothesis that the coefficients are equal to zero, based on the empirical variance estimate returned for the coefficient by the fitting procedure. Figure 3.4A shows the coefficients for the effect of NBQX. As expected, it resembles the difference between NBQX and control condition shown in Figure 3.1D. The coefficients are found to be significantly different from zero mostly for the times following stimulus on- and offset, as predicted by the STD model fitted in Figure 2.

Figure 3.4B shows the coefficients for the purely ITD-related component. Also as expected, all coefficients during stimulus presentation were found to be highly significant because the EFP does depend on ITD. The coefficients also showed the sharp transient at stimulus onset associated with the input firing behaviour (Kuokkanen et al., 2010; MacLeod et al., 2010).

Finally, examining the interaction-related coefficients in Figure 3.4C, we found no coefficient to be significantly different from zero. There appears to be some small change in the variance during stimulus presentation, which can be explained by the higher overall noise levels during stimulation. The interaction-related component is not related to the average currents from synapses and incoming axons because ITD does not affect the mean firing rates at which incoming axons and the resulting synaptic currents are driven; the ITD merely determines their relative timing on a sub-millisecond time scale. Due to the summation of contralateral and ipsilateral components in the axonal/synaptic parts of the neurophonic, this sub-millisecond timing only affects the axonal/synaptic EFP in a narrow frequency range around the stimulus frequency, but does not affect the axonal/synaptic neurophonic at other frequencies (Kuokkanen et al., 2010).

The full fit explained 48% of the variance of all observed samples. The component that did not change across ITD or NBQX conditions explained 39% of the variance. The putative synaptic contributions that were modified only by NBQX explained $< 1\%$ of the variance (Figure 3.4A), the putative axonal contributions that were modified only by ITD explained 7% (Figure 3.4B), and the putative NL spiking contributions explained $< 0.01\%$ of the variance (Figure 3.4C).

We repeated this fit for all the $n = 5$ examples, and found no significant NBQX-ITD interactions in any of the owls. We also repeated the fit for the low-pass filtered responses, as shown in Figure 3.1C, D. Here, the putative synaptic component played a more important role, explaining 1.8% of the variance, and ITD- and interaction-related components explained less than 0.2% of the variance. The constant component played a very large role, explaining 90% of the variance. These ratios further show that restricting our analysis to the low-pass filtered signal and subtracting out the constant part, as done in Figure 3.1D,E and Figure 3.2, is the best way to isolate the synaptic component.

Together, this result leads us to conclude that the difference between NBQX and control conditions examined in the previous sections does not contain significant contributions from postsynaptic NL firing activity. We cannot exclude the presence of a small contribution, but the majority must come from a different source, making the interpretation as a synaptic process subject to STD more likely.

3.3.5 A spatial model of EFP structure explains the polarity of the transient responses

As outlined in previous sections, NL synapses generated transient responses in the EFP with polarities that varied across recording locations (Figure 3.5A; see also Figure 3.1E). Taking into account NL anatomy, the varying polarity may be explained by the location of the recording electrode relative to the somata and axons of NL neurons: NL neurons are known to be almost spherical, with small, stubby dendrites and only an axon protruding from the soma (Carr and Boudreau, 1993; Kuokkanen et al., 2010). This configuration leads to a ball-and-stick-like structure of an NL neuron with a spherical soma and a myelinated axon (see Material and Methods for details), which we expected to transform excitatory synaptic input currents into EFP responses with different polarities across locations.

To test the hypothesis that the recording location affects the polarity of transients, we simulated the extracellular field produced by this model NL neuron in response to a single synaptic event at the soma (Figure 3.5B). The polarity of the resulting extracellular voltage was negative at locations opposite to the outgoing axon of an NL neuron, and positive otherwise. The polarity reversal occurred between the soma and the first node of Ranvier along the axon.

In order to predict the extracellular signature of the synaptic currents in response to the stimulations that we presented in our experiments, we applied the fitted STD process in Figure 3.2 to this spatial model. The resulting predicted extracellular responses to full stimulation are shown in Figure 3.5C. Unsurprisingly, they also show a polarity reversal, meaning that both polarities observed in experiments can be reproduced in the spatial model.

The modeling results presented in Figure 3.5B,C were simulations of a single-neuron response. The experimentally observed response is expected to be a summation of such synaptic potentials originating from many NL neurons. Experiment and theory are related only if axons of nearby NL neurons are aligned in parallel, and if NL neurons in a narrow enough spatial region (along the primary soma-axon axis) are activated by our stimuli. Both assumptions are justified in NL: NL neurons are tonotopically arranged, and our tonal

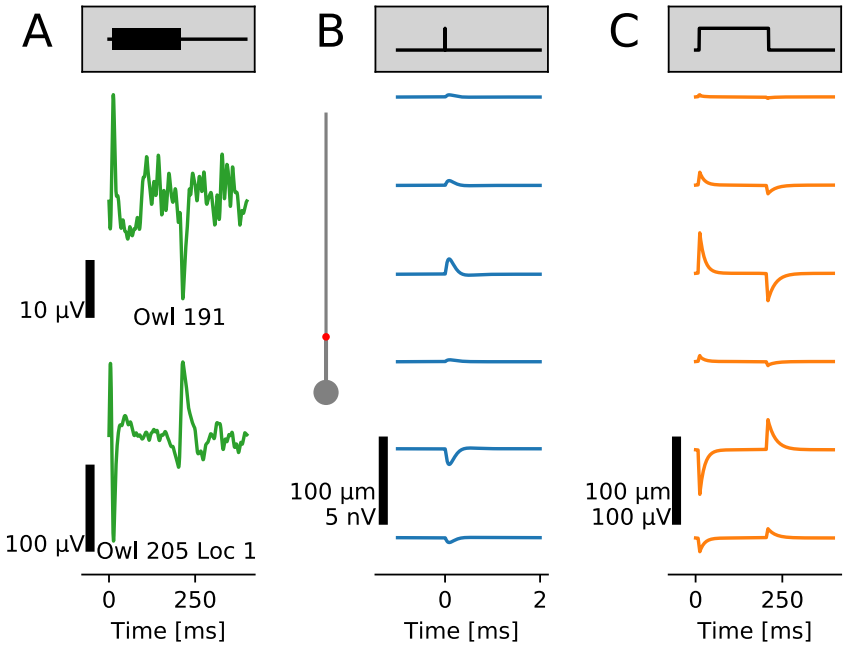

Figure 3.5: Polarity of EFPs evoked by synaptic currents can be explained by a spatially extended model of an NL neuron. (**A**) Experimental EFP responses obtained at two different recording locations can show opposite polarities (same examples as in Figure 3.1E but low-pass filtered < 100 Hz). Stimulus (black, top) in gray box. (**B**) Simulated time courses of the EFP (blue traces) generated by an NL neuron in response to a synaptic input (EPSC, black trace in gray box) in the soma. Simulated NL neuron (soma and axon) shown in gray, with the first node of Ranvier highlighted in red. Recording locations (vertical position with respect to the NL neuron) indicated by the starts of the respective blue traces (horizontal distances not to scale). Spatial (vertical) and voltage scales indicated by vertical bar. (**C**) Simulated EFP responses at different recording locations (same as in B) for synaptic currents governed by STD dynamics (as shown in Figure 2) and the input firing rate profile sketched in gray box above in a population of 2000 neurons (see also Materials and Methods). Spatial and voltage scales indicated by vertical bar.

stimulation activates NL neurons only in a narrow ($\lesssim 600\,\mu$m) frequency lamina (Kuokkanen et al., 2010); NL axons are roughly parallel to each other, and travel orthogonal to the NM axons, and parallel to the ventral border of NL (Carr and Boudreau, 1993). We therefore expect a similar overall response of a population of NL neurons as shown in Figure 3.5C (here: 2000 NL neurons and 300 synapses per neuron; see also Materials and Methods).

We attempted to test this location-dependent polarity hypothesis in further experiments. Unfortunately, it is not possible to advance an electrode parallel to an NL axon within NL because this axis is inaccessible to electrophysiology (the owl's ear is in the way). Alternatively, with a fixed electrode location, we tried to change the location at which NL neurons are activated by altering the stimulus frequency. Due to the tonotopic layout of NL (Takahashi and Konishi, 1988; Carr and Konishi, 1990), this should lead to the activation of sub-populations at different locations relative to the recording electrode. We attempted this in 3 experiments, but were unable to elicit the predicted effect. A possible explanation for this failure is that factors such as the alignment of the NL axons within the nucleus and the location of the recording electrode relative to the border of NL play a role in which polarity dominates the population response. In our experiments, the amplitude of the NBQX effect diminished with shifting frequencies, but did not re-appear with opposite polarity.

To conclude, the spatial relationship between the activated synapses and the recording location is thus able to explain the presence of different polarities in their transient EFP responses. This result further supports our hypothesis that this EFP component is of synaptic origin.

3.4 Discussion

We identified a small but consistent effect of the AMPA-receptor blocker NBQX on the extracellular field potential (EFP) recorded in the barn owl auditory brainstem. Taking advantage of the known properties of the nucleus laminaris (NL) from which we recorded while we applied tone-burst stimuli, we were able to show that the most likely source of the NBQX modulated EFP component is the synaptic current flowing in NL neurons, and that these synaptic currents are subject to short-term depression (STD), consistent with studies *in vitro* (Cook et al., 2003; Kuba et al., 2002).

3.4.1 Composition of the neurophonic potential in NL

The discovery of a small ($< 1\%$ of the overall variance) synaptic component in the neurophonic reinforces the theory of a predominantly axonal origin of

the EFP in NL (Kuokkanen et al., 2010, 2013, 2017; McColgan et al., 2017). Furthermore, as shown in Figure 3.4, we were able to put an upper bound ($< 0.1\%$ of the variance) on the even smaller contribution of NL neurons to the neurophonic. It is important to note that we could not completely exclude any contribution from NL neurons, and that further analysis of the EFP could reveal a small component associated with NL spiking activity. A small component of the non-transient EFP has been associated with NL spiking activity; the amplitude of this component strongly depends on the distance between the recording electrode and the nearest NL neuron (Kuokkanen et al., 2017).

The residuals of our fit to a model of STD in Figure 3.2B reveal further unexplained contributions to the neurophonic. The residuals have a high-frequency ($\gtrsim 200$ Hz) component that is most likely due to the stochastic nature of the activity of NM axons, which we could not capture with our model that is based on average firing rates. There is, however, also a slower ($\lesssim 100$ Hz) component visible in the residuals, which could be of a different origin. A possible candidate is the ITD-independent and frequency-non-specific recurrent inhibition from the superior olivary nucleus (Burger et al., 2005; Yang et al., 1999), which has time scales of ≈ 100 ms (Lu and Trussell, 2000; Burger et al., 2005; Tang and Lu, 2012). A second possibility could be slow potassium currents on the somata of NL neurons, which serve to compensate for DC offsets in the synaptic current (Ashida et al., 2007; Grau-Serrat et al., 2003; Kuba et al., 2005).

3.4.2 Relevance with respect to the study of synaptic processes

In our phenomenological model for STD of synaptic currents Figure 3.2, we assumed that the time constant τ_D of the slow recovery process is in the range of seconds, similar to the value 1.1 s reported by Cook et al. (2003) for the chick. Such a long time constant may seem surprising in a system that must deal with high firing rates R in the range of >100 spikes/s, i.e. average interspike intervals < 10 ms. The synapse is thus always beyond its 'limiting frequency' (Tsodyks and Markram, 1997; Tsodyks et al., 1998). However, at second glance this scenario is plausible. A long time constant τ_D, together with the high firing rate R of the input (even in the resting state), means that the synapse is always in a state in which the vesicle pool is depleted. As a result, the mean steady-state current generated by such a synapse is independent of the input rate. Since the mean input rate encodes sound intensity, this property of a depressing synapse can account for the relative insensitivity of NL neurons to sound intensity (Kuba et al., 2002; Cook et al., 2003; Peña et al., 1996). This insensitivity emerges for a wide range of utilization factors U of the STD model. The value for the utilization factor $U \approx 0.7$ determined by Cook et al.

(2003) was, however, different from the value of $U \approx 0.2$ found here. This might be due to differences in maturity, firing rates, temperatures (39°C here, 33-35°C in (Cook et al., 2003)) or extracellular calcium concentrations between the *in vivo* and *in vitro* cases (Klug et al., 2012). For review of the causes of low-release probability *in vivo*, see Borst (2010).

In analyzing possible causes of the STD process, we observed that it did not interact with spike rate adaptation in the firing patterns of NM: including a simple exponential spike rate adaptation (time constant and amplitude were the additional free fit parameters in the model) did not improve the fit to the data in Figure 3.2. We hypothesized that spike rate adaptation in NM is rapid, i.e., takes place on shorter time scales than STD. Short (< 10 ms) NM spike rate adaptation time scales are consistent with the envelope shape of the high-frequency component in Figure 3.1B and Figure 3.4B. Short time scales (8 ms) in NM spike rate adaptation were also reported by MacLeod et al. (2010). These time constants are possibly intensity-dependent, with shorter time constants for higher intensities, as observed in the auditory nerve (Westerman and Smith, 1984; Zilany et al., 2009). We used relatively high stimulus intensities ($40 - 60$ dB SPL), which further support our assumption that spike rate adaptation is faster than STD. Future studies could investigate the interaction of the two adaptive processes (STD and NM spike rate adaptation) by recording at a range of intensities and simultaneously recording NM activation statistics. When recording at low intensities close to threshold, NM adaptation might become slower and interfere with STD, making it hard to disentangle the two effects without such paired recordings, which is why we did not perform recordings at lower intensities in this study. To conclude, even though STD and spike rate adaptation could contribute to the observed adaptation of synaptic currents, both effects would support our claim that the NBQX-modulated component of the neurophonic is caused by synapses from NM axons onto NL neurons.

The ability to quantify STD *in vivo* will enable further study of its functional role. The application of a variety of different stimuli, i.e. beyond the pure tones used in our experiments, could provide further insight into the dynamics of STD in the auditory system of barn owls and other animals.

3.4.3 Conclusion

We have shown a signature of synaptic currents in the extracellular field potential (EFP) in the nucleus laminaris of the barn owl *in vivo*. We confirmed the existence of short-term depression (STD) of the synaptic current, as suggested by previous work *in vitro* in the chick (Kuba et al., 2002; Cook et al., 2003). Synaptic membrane currents and membrane currents related to the spiking activity of NL neurons were quite small, which supports the hypothesis

that currents from afferent axons dominate the EFP (Kuokkanen et al., 2010; McColgan et al., 2017).

4 Discussion

4.1 Summary of Findings

Through a combination of experimental and mathematical methods, I have shown the properties of axonal and synaptic extracellular field potentials in the barn owl auditory brainstem.

The properties of EFPs from Chapter 2 can be applied to other systems than the auditory brainstem. I showed that a bundle of axons with a projection zone containing bifurcations and terminations leads to a dipolar structure in the EFP. This EFP structure was attributed to the interplay of the bifurcations and terminations. The projection zone generates a strong dipole moment, which is maximal when the spatial scale of the membrane potential perturbation agrees with the width of the projection zone. I furthermore formulated a simplified model of the axonal EFP and showed experimentally that the predictions about the spatial structure are fulfilled in the barn owl NL. The simplified model also yielded a simple formula with which the dipole contribution of a generic activity pulse and projection zone can be predicted.

The findings on the synaptic contributions in Chapter 3 were more specific to the avian auditory brainstem. I confirmed previous *in vitro* findings of short-term depression (STD) in the NM-NL synapses (Cook et al., 2003). I showed that the time course of synaptic contributions is consistent with a simple mathematical model of STD, and was able to quantitatively fit the model to the data. The time constants of the adaptation were consistent with the fast time constant measured by Cook et al. (2003), while the utilization factor differed significantly. This measurement of STD *in vivo* is important because it shows that STD is not an artifact of the age of the animal, temperature, resting firing rates or calcium concentrations, all of which may differ between *in vivo* and *in vitro* studies.

4.2 Outlook

The barn owl neurophonic provides a unique oportunity to study the EFP in a very detailed manner. It should be possible to achieve a decomposition into all constituent parts. In Chapter 3, I have shown that it is possible to isolate

the synaptic component from the bulk signal. Future studies should be able to isolate the postsynaptic NL neuron firing activity and the recurrent inhibitory input from the superior olivary nucleus (SON). Together with the strong axonal contribution studied in Chapter 2 and the findings by Kuokkanen et al. (2010, 2013), this would account for all contributions that would be predicted from the anatomy of the nucleus (Carr and Konishi, 1990).

Recent experiments to isolate field potentials of spiking NL neurons (Kuokkanen et al., 2017) have shown that it is possible to identify the spectral contributions by analysing the ITD modulation of low-frequency components. Further analysis will show if this method also allows the direct identification of this component in the time domain.

Inhibitory feedback contributions from SON could in principle be identified using a similar pharmacological procedure as in Chapter 3. Care will have to be taken that confounding effects from increased NL activity due to disinhibition of NL neurons does not lead to wrong conclusions. Identifying the NL firing contributions first will help avoid such mistakes.

Further promising avenues of research lie in the far field contributions of NL EFPs. In Chapter 2, I suggest that axons could contribute a measurable part to the auditory brainstem response (ABR) in the barn owl. Further analysis will show if this prediction holds up after inclusion of a more detailed head model, and what the contribution of non-axonal NL firing could be. Due to the linearity of summation, no contribution of NM axons is predicted for the binaural difference potential (BDP). NL neurons on the other hand could contribute to the BDP. Conclusions about the contributions of NL EFPs to the ABR could be based on timing analysis, paired simultaneous recordings of ABR and neurophonic, or approaches which are able to selectively silence the structures, for example by lesioning or using pharmacological or optogenetic methods.

Bibliography

L. F. Abbott. Simple diagrammatic rules for solving dendritic cable problems. *Physica A: Statistical Mechanics and its Applications*, 185(1-4):343–356, June 1992. ISSN 03784371. doi: 10.1016/0378-4371(92)90474-5. URL http://dx.doi.org/10.1016/0378-4371(92)90474-5.

L. F. Abbott and Wade G. Regehr. Synaptic computation. *Nature*, 431(7010): 796–803, October 2004. ISSN 0028-0836. doi: 10.1038/nature03010. URL http://dx.doi.org/10.1038/nature03010.

L. F. Abbott, J. A. Varela, Kamal Sen, and S. B. Nelson. Synaptic depression and cortical gain control. *Science*, 275(5297):221–224, January 1997. ISSN 1095-9203. doi: 10.1126/science.275.5297.221. URL http://dx.doi.org/10.1126/science.275.5297.221.

Henrik Alle, Arnd Roth, and Jörg R. P. Geiger. Energy-efficient action potentials in hippocampal mossy fibers. *Science*, 325(5946):1405–1408, September 2009. ISSN 1095-9203. doi: 10.1126/science.1174331. URL http://dx.doi.org/10.1126/science.1174331.

Costas A. Anastassiou, Rodrigo Perin, György Buzsáki, Henry Markram, and Christof Koch. Cell type- and activity-dependent extracellular correlates of intracellular spiking. *Journal of Neurophysiology*, 114(1):608–623, July 2015. ISSN 1522-1598. doi: 10.1152/jn.00628.2014. URL http://dx.doi.org/10.1152/jn.00628.2014.

Go Ashida, Kousuke Abe, Kazuo Funabiki, and Masakazu Konishi. Passive soma facilitates submillisecond coincidence detection in the owl's auditory system. *Journal of Neurophysiology*, 97(3):2267–2282, March 2007. ISSN 1522-1598. doi: 10.1152/jn.00399.2006. URL http://dx.doi.org/10.1152/jn.00399.2006.

Go Ashida, Kazuo Funabiki, and Catherine E. Carr. Biophysical basis of the sound analog membrane potential that underlies coincidence detection in the barn owl. *Frontiers in Computational Neuroscience*, 7, 2013. ISSN 1662-5188. doi: 10.3389/fncom.2013.00102. URL http://dx.doi.org/10.3389/fncom.2013.00102.

Claude Bédard, Helmut Kröger, and Alain Destexhe. Modeling extracellular

field potentials and the frequency-filtering properties of extracellular space. *Biophysical journal*, 86(3):1829–1842, 2004.

Claude Bédard, Serafim Rodrigues, Noah Roy, Diego Contreras, and Alain Destexhe. Evidence for frequency-dependent extracellular impedance from the transfer function between extracellular and intracellular potentials. *Journal of computational neuroscience*, 29(3):389–403, 2010.

Mariano A. Belluscio, Kenji Mizuseki, Robert Schmidt, Richard Kempter, and György Buzsáki. Cross-frequency phase-phase coupling between theta and gamma oscillations in the hippocampus. *The Journal of Neuroscience*, 32(2): 423–435, January 2012. ISSN 1529-2401. doi: 10.1523/jneurosci.4122-11.2012. URL `http://dx.doi.org/10.1523/jneurosci.4122-11.2012`.

Philipp Berens, Georgios A. Keliris, Alexander S. Ecker, Nikos K. Logothetis, and Andreas S. Tolias. Comparing the feature selectivity of the gamma-band of the local field potential and the underlying spiking activity in primate visual cortex. *Frontiers in systems neuroscience*, 2, 2008. ISSN 1662-5137. doi: 10.3389/neuro.06.002.2008. URL `http://dx.doi.org/10.3389/neuro.06.002.2008`.

Antonin Blot and Boris Barbour. Ultra-rapid axon-axon ephaptic inhibition of cerebellar purkinje cells by the pinceau. *Nature Neuroscience*, 17(2): 289–295, February 2014. ISSN 1097-6256. doi: 10.1038/nn.3624. URL `http://dx.doi.org/10.1038/nn.3624`.

J Gerard G Borst. The low synaptic release probability in vivo. *Trends in Neurosciences*, 33(6):259–266, 2010.

James C Boudreau. Stimulus correlates of wave activity in the superior-olivary complex of the cat. *The Journal of the Acoustical Society of America*, 37(5): 779–785, 1965.

Stephan Brenowitz and Laurence O. Trussell. Maturation of synaptic transmission at end-bulb synapses of the cochlear nucleus. *Journal of Neuroscience*, 21(23):9487–9498, December 2001. ISSN 1529-2401. URL `http://www.jneurosci.org/content/21/23/9487.abstract`.

Romain Brette. Spiking models for level-invariant encoding. *Frontiers in Computational Neuroscience*, 5, 2011. ISSN 1662-5188. doi: 10.3389/fncom.2011.00063. URL `http://dx.doi.org/10.3389/fncom.2011.00063`.

Romain Brette and Alain Destexhe, editors. *Handbook of Neural Activity Measurement*. Cambridge University Press, Cambridge, 2012. ISBN 9780511979958. doi: 10.1017/cbo9780511979958. URL `http://dx.doi.org/10.1017/cbo9780511979958`.

Mark Browning, John Cleckler, Kayla Knott, and Matthew Johnson. Prey

consumption by a large aggregation of barn owls in an agricultural setting. *Proceedings of the 27th Vertebrate Pest Conference*, 2016.

Julian M. L. Budd, Krisztina Kovács, Alex S. Ferecskó, Péter Buzás, Ulf T. Eysel, and Zoltán F. Kisvárday. Neocortical axon arbors trade-off material and conduction delay conservation. *PLoS Computational Biology*, 6(3): e1000711+, March 2010. doi: 10.1371/journal.pcbi.1000711. URL `http://dx.doi.org/10.1371/journal.pcbi.1000711`.

R. Michael Burger, Karina S. Cramer, Joshua D. Pfeiffer, and Edwin W. Rubel. Avian superior olivary nucleus provides divergent inhibitory input to parallel auditory pathways. *J. Comp. Neurol.*, 481(1):6–18, January 2005. doi: 10.1002/cne.20334. URL `http://dx.doi.org/10.1002/cne.20334`.

György Buzsáki, Costas A. Anastassiou, and Christof Koch. The origin of extracellular fields and currents - EEG, ECoG, LFP and spikes. *Nature Reviews Neuroscience*, 13(6):407–420, May 2012. ISSN 1471-003X. doi: 10.1038/nrn3241. URL `http://dx.doi.org/10.1038/nrn3241`.

C. E. Carr and R. E. Boudreau. An axon with a myelinated initial segment in the bird auditory system. *Brain Research*, 628(1-2):330–334, November 1993. ISSN 00068993. doi: 10.1016/0006-8993(93)90975-s. URL `http://dx.doi.org/10.1016/0006-8993(93)90975-s`.

C. E. Carr and M. Konishi. Axonal delay lines for time measurement in the owl's brainstem. *Proceedings of the National Academy of Sciences*, 85(21): 8311–8315, November 1988. ISSN 1091-6490. URL `http://www.pnas.org/content/85/21/8311.abstract`.

C. E. Carr and M. Konishi. A circuit for detection of interaural time differences in the brain stem of the barn owl. *The Journal of Neuroscience*, 10(10): 3227–3246, October 1990. ISSN 1529-2401. URL `http://www.jneurosci.org/content/10/10/3227.abstract`.

Catherine Carr, Sahil Shah, Go Ashida, Thomas McColgan, Hermann Wagner, PaulaT Kuokkanen, Richard Kempter, and Christine Köppl. Maps of ITD in the nucleus laminaris of the barn owl. In Brian C. J. Moore, Roy D. Patterson, Ian M. Winter, Robert P. Carlyon, and Hedwig E. Gockel, editors, *Basic Aspects of Hearing*, volume 787 of *Advances in Experimental Medicine and Biology*, pages 215–222. Springer, New York, 2013. doi: 10.1007/978-1-4614-1590-9_24. URL `http://dx.doi.org/10.1007/978-1-4614-1590-9_24`.

Catherine E. Carr, Sahil Shah, Thomas McColgan, Go Ashida, Paula T. Kuokkanen, Sandra Brill, Richard Kempter, and Hermann Wagner. Maps of interaural delay in the owl's nucleus laminaris. *Journal of Neurophysiology*, 114(3):1862–1873, September 2015. ISSN 1522-1598. doi: 10.1152/jn.00644.2015. URL `http://dx.doi.org/10.1152/jn.00644.2015`.

Catherine E. Carr, Go Ashida, Hermann Wagner, Thomas McColgan, and Richard Kempter. The role of conduction delay in creating sensitivity to interaural time differences. In Pim van Dijk, Deniz Başkent, Etienne Gaudrain, Emile de Kleine, Anita Wagner, and Cris Lanting, editors, *Physiology, Psychoacoustics and Cognition in Normal and Impaired Hearing*, volume 894 of *Advances in Experimental Medicine and Biology*, pages 189–196. Springer International Publishing, 2016. doi: 10.1007/978-3-319-25474-6_20. URL `http://dx.doi.org/10.1007/978-3-319-25474-6_20`.

S. Y. Chiu and J. M. Ritchie. Evidence for the presence of potassium channels in the paranodal region of acutely demyelinated mammalian single nerve fibres. *The Journal of Physiology*, 313(1):415–437, April 1981. doi: 10.1113/jphysiol.1981.sp013674. URL `http://dx.doi.org/10.1113/jphysiol.1981.sp013674`.

Sooyoung Chung, Xiangrui Li, and Sacha B. Nelson. Short-term depression at thalamocortical synapses contributes to rapid adaptation of cortical sensory responses in vivo. *Neuron*, 34(3):437–446, April 2002. ISSN 08966273. doi: 10.1016/s0896-6273(02)00659-1. URL `http://dx.doi.org/10.1016/s0896-6273(02)00659-1`.

Daniel L. Cook, Peter C. Schwindt, Lucinda A. Grande, and William J. Spain. Synaptic depression in the localization of sound. *Nature*, 421(6918): 66–70, January 2003. ISSN 0028-0836. doi: 10.1038/nature01248. URL `http://dx.doi.org/10.1038/nature01248`.

John Crank. *The mathematics of diffusion*. Oxford University Press, USA, 1979.

Hermann Cuntz, Friedrich Forstner, Alexander Borst, and Michael Häusser. One rule to grow them all: A general theory of neuronal branching and its practical application. *PLoS Computational Biology*, 6(8):e1000877+, August 2010. doi: 10.1371/journal.pcbi.1000877. URL `http://dx.doi.org/10.1371/journal.pcbi.1000877`.

William M. DeBello and Eric I. Knudsen. Multiple sites of adaptive plasticity in the owl's auditory localization pathway. *The Journal of Neuroscience*, 24(31): 6853–6861, August 2004. ISSN 1529-2401. doi: 10.1523/jneurosci.0480-04.2004. URL `http://dx.doi.org/10.1523/jneurosci.0480-04.2004`.

Michael Denker, Sébastien Roux, Henrik Lindén, Markus Diesmann, Alexa Riehle, and Sonja Grün. The local field potential reflects surplus spike synchrony. *Cerebral Cortex*, 21(12):2681–2695, December 2011. ISSN 1460-2199. doi: 10.1093/cercor/bhr040. URL `http://dx.doi.org/10.1093/cercor/bhr040`.

Norman R. Draper and Harry Smith. *Applied regression analysis*. John Wiley & Sons, 2014.

Gaute T. Einevoll, Christoph Kayser, Nikos K. Logothetis, and Stefano Panzeri. Modelling and analysis of local field potentials for studying the function of cortical circuits. *Nature reviews. Neuroscience*, 14(11):770–785, November 2013. ISSN 1471-0048. doi: 10.1038/nrn3599. URL `http://dx.doi.org/10.1038/nrn3599`.

D. E. Feldman and E. I. Knudsen. NMDA and non-NMDA glutamate receptors in auditory transmission in the barn owl inferior colliculus. *Journal of Neuroscience*, 14(10):5939–5958, October 1994. ISSN 1529-2401. URL `http://www.jneurosci.org/content/14/10/5939.abstract`.

Dirk Feldmeyer. Excitatory neuronal connectivity in the barrel cortex. *Frontiers in Neuroanatomy*, 6, 2012. ISSN 1662-5129. doi: 10.3389/fnana.2012.00024. URL `http://dx.doi.org/10.3389/fnana.2012.00024`.

Antonio Fernández-Ruiz, Sagrario Muñoz, Miguel Sancho, Julia Makarova, Valeri A. Makarov, and Oscar Herreras. Cytoarchitectonic and dynamic origins of giant positive local field potentials in the dentate gyrus. *The Journal of Neuroscience*, 33(39):15518–15532, September 2013. ISSN 1529-2401. doi: 10.1523/jneurosci.0338-13.2013. URL `http://dx.doi.org/10.1523/jneurosci.0338-13.2013`.

Brian J Fischer and José Luis Peña. Owl's behavior and neural representation predicted by bayesian inference. *Nature neuroscience*, 14(8):1061, 2011.

Eric S. Fortune and Gary J. Rose. Short-term synaptic plasticity as a temporal filter. *Trends in Neurosciences*, 24(7):381–385, July 2001. ISSN 01662236. doi: 10.1016/s0166-2236(00)01835-x. URL `http://dx.doi.org/10.1016/s0166-2236(00)01835-x`.

Iwao Fukui and Harunori Ohmori. Tonotopic gradients of membrane and synaptic properties for neurons of the chicken nucleus magnocellularis. *Journal of Neuroscience*, 24(34):7514–7523, August 2004. ISSN 1529-2401. doi: 10.1523/jneurosci.0566-04.2004. URL `http://dx.doi.org/10.1523/jneurosci.0566-04.2004`.

Kazuo Funabiki, Konomi Koyano, and Harunori Ohmori. The role of GABAergic inputs for coincidence detection in the neurones of nucleus laminaris of the chick. *Journal of Physiology*, 508(3):851–869, 1998.

Kazuo Funabiki, Go Ashida, and Masakazu Konishi. Computation of interaural time difference in the owl's coincidence detector neurons. *The Journal of Neuroscience*, 31(43):15245–15256, October 2011. ISSN 1529-2401. doi: 10.1523/jneurosci.2127-11.2011. URL `http://dx.doi.org/10.1523/jneurosci.2127-11.2011`.

J. R. Geiger and P. Jonas. Dynamic control of presynaptic Ca(2+) inflow by fast-inactivating K(+) channels in hippocampal mossy fiber boutons.

Neuron, 28(3):927–939, December 2000. ISSN 0896-6273. URL `http://view.ncbi.nlm.nih.gov/pubmed/11163277`.

Carl Gold, Darrell A. Henze, Christof Koch, and György Buzsáki. On the origin of the extracellular action potential waveform: A modeling study. *Journal of Neurophysiology*, 95(5):3113–3128, May 2006. ISSN 0022-3077. doi: 10.1152/jn.00979.2005. URL `http://dx.doi.org/10.1152/jn.00979.2005`.

Joshua H. Goldwyn and John Rinzel. Neuronal coupling by endogenous electric fields: cable theory and applications to coincidence detector neurons in the auditory brain stem. *Journal of Neurophysiology*, 115(4):2033–2051, April 2016. ISSN 0022-3077. doi: 10.1152/jn.00780.2015. URL `http://dx.doi.org/10.1152/jn.00780.2015`.

Joshua H. Goldwyn, Myles Mc Laughlin, Eric Verschooten, Philip X. Joris, and John Rinzel. A model of the medial superior olive explains spatiotemporal features of local field potentials. *The Journal of Neuroscience*, 34(35):11705–11722, August 2014. ISSN 1529-2401. doi: 10.1523/jneurosci.0175-14.2014. URL `http://dx.doi.org/10.1523/jneurosci.0175-14.2014`.

Alfredo Gonzalez-Sulser, Jing Wang, Bridget N. Queenan, Massimo Avoli, Stefano Vicini, and Rhonda Dzakpasu. Hippocampal neuron firing and local field potentials in the in vitro 4-aminopyridine epilepsy model. *Journal of Neurophysiology*, 108(9):2568–2580, November 2012. ISSN 1522-1598. doi: 10.1152/jn.00363.2012. URL `http://dx.doi.org/10.1152/jn.00363.2012`.

C. S. Goodman, M. J. Bastiani, C. Q. Doe, S. du Lac, S. L. Helfand, J. Y. Kuwada, and J. B. Thomas. Cell recognition during neuronal development. *Science*, 225(4668):1271–1279, September 1984. ISSN 0036-8075. doi: 10.1126/science.6474176. URL `http://dx.doi.org/10.1126/science.6474176`.

Sergey L. Gratiy, Geir Halnes, Daniel Denman, Michael J. Hawrylycz, Christof Koch, Gaute T. Einevoll, and Costas A. Anastassiou. From maxwell's equations to the theory of current-source density analysis. *Eur J Neurosci*, 45(8):1013–1023, April 2017. doi: 10.1111/ejn.13534. URL `http://dx.doi.org/10.1111/ejn.13534`.

Victor Grau-Serrat, Catherine E. Carr, and Jonathan Z. Simon. Modeling coincidence detection in nucleus laminaris. *Biological Cybernetics*, 89(5):388–396, 2003. doi: 10.1007/s00422-003-0444-4. URL `http://dx.doi.org/10.1007/s00422-003-0444-4`.

Sabine Grosser, Bridget N. Queenan, Rupa R. Lalchandani, and Stefano Vicini. Hilar somatostatin interneurons contribute to synchronized GABA activity in an in vitro epilepsy model. *PLOS ONE*, 9(1):e86250+, January 2014. doi: 10.1371/journal.pone.0086250. URL `http://dx.doi.org/10.1371/journal.pone.0086250`.

Yoram Gutfreund. Stimulus-specific adaptation, habituation and change detection in the gaze control system. *Biological Cybernetics*, 106(11-12): 657–668, June 2012. ISSN 0340-1200. doi: 10.1007/s00422-012-0497-3. URL http://dx.doi.org/10.1007/s00422-012-0497-3.

A. Gydikov, L. Gerilovsky, N. Radicheva, and N. Trayanova. Influence of the muscle fibre end geometry on the extracellular potentials. *Biological Cybernetics*, 54(1):1–8, 1986. doi: 10.1007/bf00337110. URL http://dx.doi.org/10.1007/bf00337110.

A. A. Gydikov and N. A. Trayanova. Extracellular potentials of single active muscle fibres: Effects of finite fibre length. *Biological Cybernetics*, 53(6): 363–372, 1986. doi: 10.1007/bf00318202. URL http://dx.doi.org/10.1007/bf00318202.

Geir Halnes, Tuomo Mäki-Marttunen, Klas H. Pettersen, Ole A. Andreassen, and Gaute T. Einevoll. Ion diffusion may introduce spurious current sources in current-source density (csd) analysis. *Journal of Neurophysiology*, 118 (1):114–120, July 2017. ISSN 1522-1598. doi: 10.1152/jn.00976.2016. URL http://dx.doi.org/10.1152/jn.00976.2016.

J. B. Harris and R. R. Ribchester. The relationship between end-plate size and transmitter release in normal and dystrophic muscles of the mouse. *The Journal of Physiology*, 296(1):245–265, November 1979. doi: 10.1113/jphysiol.1979.sp013003. URL http://dx.doi.org/10.1113/jphysiol.1979.sp013003.

Laura Hausmann, Mark von Campenhausen, Frank Endler, Martin Singheiser, and Hermann Wagner. Improvements of sound localization abilities by the facial ruff of the barn owl (tyto alba) as demonstrated by virtual ruff removal. *PLoS One*, 4(11):e7721, 2009.

Oliver Heaviside. *Electromagnetic Theory*, volume 1, chapter 3, pages 132–305. The Electrician Publishing Company, 1893.

H. G. E. Hentschel and A. van Ooyen. Models of axon guidance and bundling during development. *Proceedings of the Royal Society of London B: Biological Sciences*, 266(1434):2231–2238, November 1999. ISSN 1471-2954. doi: 10.1098/rspb.1999.0913. URL http://dx.doi.org/10.1098/rspb.1999.0913.

Joachim Hermann, Benedikt Grothe, and Achim Klug. Modeling short-term synaptic plasticity at the calyx of Held using in vivo-like stimulation patterns. *Journal of Neurophysiology*, 101(1):20–30, January 2009. ISSN 1522-1598. doi: 10.1152/jn.90243.2008. URL http://dx.doi.org/10.1152/jn.90243.2008.

O. Herreras, J. Makarova, and V. A. Makarov. New uses of lfps: Pathway-

specific threads obtained through spatial discrimination. *Neuroscience*, 310: 486–503, December 2015. ISSN 03064522. doi: 10.1016/j.neuroscience.2015.09.054. URL http://dx.doi.org/10.1016/j.neuroscience.2015.09.054.

M. L. Hines and N. T. Carnevale. The NEURON simulation environment. *Neural Computation*, 9(6):1179–1209, August 1997. ISSN 0899-7667. doi: 10.1162/neco.1997.9.6.1179. URL http://dx.doi.org/10.1162/neco.1997.9.6.1179.

Michael L. Hines, Andrew P. Davison, and Eilif Muller. NEURON and Python. *Frontiers in Neuroinformatics*, 3, 2009. ISSN 1662-5196. doi: 10.3389/neuro.11.001.2009. URL http://dx.doi.org/10.3389/neuro.11.001.2009.

MichaelL Hines, Thomas Morse, Michele Migliore, NicholasT Carnevale, and GordonM Shepherd. Modeldb: A database to support computational neuroscience. *Journal of Computational Neuroscience*, 17(1):7–11, July 2004. ISSN 0929-5313. doi: 10.1023/b:jcns.0000023869.22017.2e. URL http://dx.doi.org/10.1023/b:jcns.0000023869.22017.2e.

Gary R. Holt and Christof Koch. Electrical interactions via the extracellular potential near cell bodies. *Journal of Computational Neuroscience*, 6(2): 169–184, March 1999. ISSN 09295313. doi: 10.1023/a:1008832702585. URL http://dx.doi.org/10.1023/a:1008832702585.

Yoshinori Izaki, Masatoshi Takita, and Masahiko Nomura. Local properties of CA1 region in hippocampo-prefrontal synaptic plasticity in rats. *Neuroreport*, 13(4):469–472, March 2002. ISSN 0959-4965. URL http://view.ncbi.nlm.nih.gov/pubmed/11930163.

James J. Jack, Denis Noble, and Richard W. Tsien. *Electric current flow in excitable cells*. Clarendon Press Oxford, 1975.

John D. Jackson. *Classical electrodynamics*. John Wiley & Sons, 2007.

Lloyd A. Jeffress. A place theory of sound localization. *Journal of Comparative and Physiological Psychology*, 41(1):35–39, February 1948. URL http://psycnet.apa.org/index.cfm?fa=search.displayRecord&id=F0BE069D-BF68-BB7F-0A03-D83AB1C01E7C&resultID=1&page=1&dbTab=all.

Eric Jones, Travis Oliphant, Pearu Peterson, and Others. SciPy: Open source scientific tools for Python, 2001. URL http://www.scipy.org/.

Eric R. Kandel, James H. Schwartz, Thomas M. Jessell, and Others. *Principles of neural science*, volume 4. McGraw-Hill New York, 2000.

B. Katz. The terminations of the afferent nerve fibre in the muscle spindle of the frog. *Philosophical Transactions of the Royal Society B: Biological*

Sciences, 243(703):221–240, February 1961. ISSN 0962-8436. doi: 10.1098/rstb.1961.0001. URL http://dx.doi.org/10.1098/rstb.1961.0001.

B. Katz and R. Miledi. Propagation of electric activity in motor nerve terminals. *Proceedings of the Royal Society of London B: Biological Sciences*, 161(985): 453–482, February 1965. ISSN 1471-2954. doi: 10.1098/rspb.1965.0015. URL http://dx.doi.org/10.1098/rspb.1965.0015.

Steffen Katzner, Ian Nauhaus, Andrea Benucci, Vincent Bonin, Dario L. Ringach, and Matteo Carandini. Local origin of field potentials in visual cortex. *Neuron*, 61(1):35–41, January 2009. ISSN 1097-4199. doi: 10.1016/j.neuron.2008.11.016. URL http://dx.doi.org/10.1016/j.neuron.2008.11.016.

Alexander R. Kent and Warren M. Grill. Neural origin of evoked potentials during thalamic deep brain stimulation. *Journal of Neurophysiology*, 110 (4):826–843, August 2013. ISSN 1522-1598. URL http://view.ncbi.nlm.nih.gov/pubmed/23719207.

Achim Klug, J. Gerard Borst, Bruce A. Carlson, Cornelia Kopp-Scheinpflug, Vitaly A. Klyachko, and Matthew A. Xu-Friedman. How do short-term changes at synapses fine-tune information processing? *The Journal of neuroscience : the official journal of the Society for Neuroscience*, 32(41): 14058–14063, October 2012. ISSN 1529-2401. doi: 10.1523/JNEUROSCI.3348-12.2012. URL http://dx.doi.org/10.1523/JNEUROSCI.3348-12.2012.

Christof Koch. *Biophysics of computation: information processing in single neurons*. Oxford University Press, USA, 2004.

Masakazu Konishi. How the owl tracks its prey: experiments with trained barn owls reveal how their acute sense of hearing enables them to catch prey in the dark. *American Scientist*, 61(4):414–424, 1973.

Masakazu Konishi, W. Edward Sullivan, and Terry Takahashi. The owl's cochlear nuclei process different sound localization cues. *The Journal of the Acoustical Society of America*, 78(1):360–364, July 1985. ISSN 0001-4966. doi: 10.1121/1.392499. URL http://dx.doi.org/10.1121/1.392499.

Christine Köppl. Phase locking to high frequencies in the auditory nerve and cochlear nucleus magnocellularis of the barn owl, tyto alba. *The Journal of Neuroscience*, 17(9):3312–3321, May 1997a. ISSN 1529-2401. URL http://www.jneurosci.org/content/17/9/3312.abstract.

Christine Köppl. Frequency tuning and spontaneous activity in the auditory nerve and cochlear nucleus magnocellularis of the barn owl tyto alba. *Journal of Neurophysiology*, 77(1):364–377, January 1997b. ISSN 1522-1598. URL http://jn.physiology.org/content/77/1/364.abstract.

Christine Köppl and Catherine E. Carr. Maps of interaural time difference in the chicken's brainstem nucleus laminaris. *Biological cybernetics*, 98(6): 541–559, June 2008. ISSN 0340-1200. doi: 10.1007/s00422-008-0220-6. URL http://dx.doi.org/10.1007/s00422-008-0220-6.

Gabriel Kreiman, Chou P. Hung, Alexander Kraskov, Rodrigo Q. Quiroga, Tomaso Poggio, and James J. DiCarlo. Object selectivity of local field potentials and spikes in the macaque inferior temporal cortex. *Neuron*, 49(3): 433–445, February 2006. ISSN 08966273. doi: 10.1016/j.neuron.2005.12.019. URL http://dx.doi.org/10.1016/j.neuron.2005.12.019.

Hiroshi Kuba and Harunori Ohmori. Roles of axonal sodium channels in precise auditory time coding at nucleus magnocellularis of the chick. *The Journal of Physiology*, 587(1):87–100, January 2009. doi: 10.1113/jphysiol.2008.162651. URL http://dx.doi.org/10.1113/jphysiol.2008.162651.

Hiroshi Kuba, Konomi Koyano, and Harunori Ohmori. Synaptic depression improves coincidence detection in the nucleus laminaris in brainstem slices of the chick embryo. *European Journal of Neuroscience*, 15(6):984–990, March 2002. doi: 10.1046/j.1460-9568.2002.01933.x. URL http://dx.doi.org/10.1046/j.1460-9568.2002.01933.x.

Hiroshi Kuba, Rei Yamada, Iwao Fukui, and Harunori Ohmori. Tonotopic specialization of auditory coincidence detection in nucleus laminaris of the chick. *Journal of Neuroscience*, 25(8):1924–1934, February 2005. ISSN 1529-2401. doi: 10.1523/jneurosci.4428-04.2005. URL http://dx.doi.org/10.1523/jneurosci.4428-04.2005.

Hiroshi Kuba, Takahiro M. Ishii, and Harunori Ohmori. Axonal site of spike initiation enhances auditory coincidence detection. *Nature*, 444(7122):1069–1072, November 2006. ISSN 0028-0836. doi: 10.1038/nature05347. URL http://dx.doi.org/10.1038/nature05347.

M. Fabiana Kubke, Dino P. Massoglia, and Catherine E. Carr. Bigger brains or bigger nuclei? regulating the size of auditory structures in birds. *Brain, Behavior and Evolution*, 63(3):169–180, 2004. ISSN 1421-9743. doi: 10.1159/000076242. URL http://dx.doi.org/10.1159/000076242.

Paula T. Kuokkanen, Hermann Wagner, Go Ashida, Catherine E. Carr, and Richard Kempter. On the origin of the extracellular field potential in the nucleus laminaris of the barn owl (tyto alba). *Journal of Neurophysiology*, 104 (4):2274–2290, October 2010. ISSN 1522-1598. doi: 10.1152/jn.00395.2010. URL http://dx.doi.org/10.1152/jn.00395.2010.

Paula T. Kuokkanen, Go Ashida, Catherine E. Carr, Hermann Wagner, and Richard Kempter. Linear summation in the barn owl's brainstem underlies responses to interaural time differences. *Journal of Neurophysiology*, April

2013. ISSN 1522-1598. doi: 10.1152/jn.00410.2012. URL http://dx.doi.org/10.1152/jn.00410.2012.

Paula T Kuokkanen, Go Ashida, Anna Kraemer, Thomas McColgan, Kazuo Funabiki, Hermann Wagner, Christine Köppl, Catherine E Carr, and Richard Kempter. Contribution of action potentials to the extracellular field potential in the nucleus laminaris of barn owl. *Journal of neurophysiology*, 119(4): 1422–1436, 2017.

Szymon Łęski, Daniel K Wójcik, Joanna Tereszczuk, Daniel A Świejkowski, Ewa Kublik, and Andrzej Wróbel. Inverse current-source density method in 3d: reconstruction fidelity, boundary effects, and influence of distant sources. *Neuroinformatics*, 5(4):207–222, 2007.

M. D. Levin, M. F. Kubke, M. Schneider, R. Wenthold, and C. E. Carr. Localization of ampa-selective glutamate receptors in the auditory brainstem of the barn owl. *The Journal of Computational Neurology*, 378(2):239–253, February 1997. ISSN 1096-9861. doi: 10.1002/(sici)1096-9861(19970210)378:2\%3C239::aid-cne7\%3E3.0.co;2-4. URL http://dx.doi.org/10.1002/(sici)1096-9861(19970210)378:2%3C239::aid-cne7%3E3.0.co;2-4.

Henrik Lindén, Klas H. Pettersen, and Gaute T. Einevoll. Intrinsic dendritic filtering gives low-pass power spectra of local field potentials. *Journal of Computational Neuroscience*, 29(3):423–444, December 2010. ISSN 1573-6873. doi: 10.1007/s10827-010-0245-4. URL http://dx.doi.org/10.1007/s10827-010-0245-4.

Henrik Lindén, Tom Tetzlaff, Tobias C. Potjans, Klas H. Pettersen, Sonja Grün, Markus Diesmann, and Gaute T. Einevoll. Modeling the spatial reach of the LFP. *Neuron*, 72(5):859–872, December 2011. ISSN 08966273. doi: 10.1016/j.neuron.2011.11.006. URL http://dx.doi.org/10.1016/j.neuron.2011.11.006.

Henrik Lindén, Espen Hagen, Szymon Leski, Eivind S. Norheim, Klas H. Pettersen, and Gaute T. Einevoll. Lfpy: a tool for biophysical simulation of extracellular potentials generated by detailed model neurons. *Frontiers in Neuroinformatics*, 7:41+, January 2014. ISSN 1662-5196. doi: 10.3389/fninf.2013.00041. URL http://dx.doi.org/10.3389/fninf.2013.00041.

Jing Liu and William T. Newsome. Local field potential in cortical area mt: stimulus tuning and behavioral correlations. *The Journal of neuroscience : the official journal of the Society for Neuroscience*, 26(30):7779–7790, July 2006. ISSN 1529-2401. doi: 10.1523/jneurosci.5052. URL http://dx.doi.org/10.1523/jneurosci.5052.

David Lodge and Kenneth M. Johnson. Noncompetitive excitatory amino acid receptor antagonists. *Trends in Pharmacological Sciences*, 11(2):81–86,

February 1990. ISSN 01656147. doi: 10.1016/0165-6147(90)90323-z. URL http://dx.doi.org/10.1016/0165-6147(90)90323-z.

Nikos K Logothetis, Christoph Kayser, and Axel Oeltermann. In vivo measurement of cortical impedance spectrum in monkeys: implications for signal propagation. *Neuron*, 55(5):809–823, 2007.

Tao Lu and Laurence O. Trussell. Inhibitory transmission mediated by asynchronous transmitter release. *Neuron*, 26(3):683–694, June 2000. ISSN 08966273. doi: 10.1016/s0896-6273(00)81204-0. URL http://dx.doi.org/10.1016/s0896-6273(00)81204-0.

K. M. MacLeod, T. K. Horiuchi, and C. E. Carr. A role for short-term synaptic facilitation and depression in the processing of intensity information in the auditory brain stem. *Journal of Neurophysiology*, 97(4):2863–2874, April 2007. ISSN 1522-1598. doi: 10.1152/jn.01030.2006. URL http://dx.doi.org/10.1152/jn.01030.2006.

Katrina M. MacLeod and Catherine E. Carr. Synaptic mechanisms of coincidence detection. In Laurence O. Trussell, Arthur N. Popper, and Richard R. Fay, editors, *Synaptic Mechanisms in the Auditory System*, volume 41 of *Springer Handbook of Auditory Research*, pages 135–164. Springer, New York, 2012. doi: 10.1007/978-1-4419-9517-9_6. URL http://dx.doi.org/10.1007/978-1-4419-9517-9_6.

Katrina M. MacLeod and Timothy K. Horiuchi. A rapid form of activity-dependent recovery from short-term synaptic depression in the intensity pathway of the auditory brainstem. *Biological Cybernetics*, 104(3):209–223, March 2011. doi: 10.1007/s00422-011-0428-8. URL http://dx.doi.org/10.1007/s00422-011-0428-8.

Katrina M. MacLeod, Go Ashida, Chris Glaze, and Catherine E. Carr. Short-term synaptic plasticity and adaptation contribute to the coding of timing and intensity information. In Enrique A. Lopez-Poveda, Alan R. Palmer, and Ray Meddis, editors, *The Neurophysiological Bases of Auditory Perception*, pages 347–356. Springer, New York, 2010. doi: 10.1007/978-1-4419-5686-6_33. URL http://dx.doi.org/10.1007/978-1-4419-5686-6_33.

Valeri A. Makarov, Julia Makarova, and Oscar Herreras. Disentanglement of local field potential sources by independent component analysis. *Journal of computational neuroscience*, 29(3):445–457, December 2010. ISSN 1573-6873. doi: 10.1007/s10827-009-0206-y. URL http://dx.doi.org/10.1007/s10827-009-0206-y.

Julia Makarova. Parallel readout of pathway-specific inputs to laminated brain structures. *Frontiers in Systems Neuroscience*, 5:77, 2011. ISSN 16625137. doi: 10.3389/fnsys.2011.00077. URL http://dx.doi.org/10.3389/fnsys.2011.00077.

Julia Makarova, Tania OrtuÃ±o, Alejandra Korovaichuk, Javier Cudeiro, Valeri A. Makarov, Casto Rivadulla, and Oscar Herreras. Can pathway-specific lfps be obtained in cytoarchitectonically complex structures? *Frontiers in Systems Neuroscience*, 8, May 2014. ISSN 1662-5137. doi: 10.3389/fnsys.2014.00066. URL `http://dx.doi.org/10.3389/fnsys.2014.00066`.

Eric Maris and Robert Oostenveld. Nonparametric statistical testing of EEG- and MEG-data. *Journal of Neuroscience Methods*, 164(1):177–190, August 2007. ISSN 01650270. doi: 10.1016/j.jneumeth.2007.03.024. URL `http://dx.doi.org/10.1016/j.jneumeth.2007.03.024`.

J Clerk Maxwell. A dynamical theory of the electromagnetic field. *Proceedings of the Royal Society of London*, pages 531–536, 1863.

Myles Mc Laughlin, Eric Verschooten, and Philip X. Joris. Oscillatory dipoles as a source of phase shifts in field potentials in the mammalian auditory brainstem. *The Journal of Neuroscience*, 30(40):13472–13487, October 2010. ISSN 1529-2401. doi: 10.1523/jneurosci.0294-10.2010. URL `http://dx.doi.org/10.1523/jneurosci.0294-10.2010`.

Thomas McColgan and Ji Liu. Pylaminaris. `https://github.com/phreeza/pyLaminaris`, 2017.

Thomas McColgan, Sahil Shah, Christine Köppl, Catherine E. Carr, and Hermann Wagner. A functional circuit model of interaural time difference processing. *Journal of Neurophysiology*, 112(11):2850–2864, September 2014. ISSN 1522-1598. doi: 10.1152/jn.00484.2014. URL `http://dx.doi.org/10.1152/jn.00484.2014`.

Thomas McColgan, Ji Liu, Paula T. Kuokkanen, Catherine E. Carr, Hermann Wagner, and Richard Kempter. Dipolar extracellular potentials generated by axonal projections. *bioRxiv*, pages 109918+, March 2017. doi: 10.1101/109918. URL `http://dx.doi.org/10.1101/109918`.

Christoph M. Michel, Micah M. Murray, Göran Lantz, Sara Gonzalez, Laurent Spinelli, and Rolando Grave de Peralta. Eeg source imaging. *Clinical Neurophysiology*, 115(10):2195–2222, October 2004. ISSN 13882457. doi: 10.1016/j.clinph.2004.06.001. URL `http://dx.doi.org/10.1016/j.clinph.2004.06.001`.

U. Mitzdorf. Current source-density method and application in cat cerebral cortex: investigation of evoked potentials and EEG phenomena. *Physiological Reviews*, 65(1):37–100, January 1985. ISSN 1522-1210. URL `http://physrev.physiology.org/content/65/1/37.abstract`.

U. Mitzdorf and W. Singer. Prominent excitatory pathways in the cat visual cortex (A 17 and A 18): A current source density analysis of electrically

evoked potentials. *Experimental Brain Research*, 33(3-4):371–394, 1978. doi: 10.1007/bf00235560. URL http://dx.doi.org/10.1007/bf00235560.

Ulla Mitzdorf and Wolf Singer. Laminar segregation of afferents to lateral geniculate nucleus of the cat: an analysis of current source density. *Journal of Neurophysiology*, 40(6):1227–1244, 1977.

A. Moiseff and M. Konishi. Neuronal and behavioral sensitivity to binaural time differences in the owl. *Journal of Neuroscience*, 1(1):40–48, January 1981. ISSN 1529-2401. URL http://www.jneurosci.org/content/1/1/40.abstract.

A. B. Mulder, M. P. M. Arts, and F. H. Lopes da Silva. Short- and long-term plasticity of the hippocampus to nucleus accumbens and prefrontal cortex pathways in the rat, in vivo. *European Journal of Neuroscience*, 9 (8):1603–1611, August 1997. doi: 10.1111/j.1460-9568.1997.tb01518.x. URL http://dx.doi.org/10.1111/j.1460-9568.1997.tb01518.x.

Torbjørn V. Ness, Michiel W. H. Remme, and Gaute T. Einevoll. Active subthreshold dendritic conductances shape the local field potential. *J Physiol*, 594(13):3809–3825, July 2016. doi: 10.1113/jp272022. URL http://dx.doi.org/10.1113/jp272022.

C. Nicholson and J. A. Freeman. Theory of current source-density analysis and determination of conductivity tensor for anuran cerebellum. *Journal of Neurophysiology*, 38(2):356–368, March 1975. ISSN 0022-3077. URL http://jn.physiology.org/content/38/2/356.abstract.

C. Nicholson and J. M. Phillips. Ion diffusion modified by tortuosity and volume fraction in the extracellular microenvironment of the rat cerebellum. *The Journal of Physiology*, 321(1):225–257, December 1981. ISSN 1469-7793. URL http://jp.physoc.org/content/321/1/225.abstract.

Charles Nicholson. Theoretical analysis of field potentials in anisotropic ensembles of neuronal elements. *IEEE Transactions on Biomedical Engineering*, BME-20(4):278–288, July 1973. ISSN 0018-9294. doi: 10.1109/tbme.1973.324192. URL http://dx.doi.org/10.1109/tbme.1973.324192.

H. O. Nornes and G. D. Das. Temporal pattern of neurogenesis in spinal cord: cytoarchitecture and directed growth of axons. *Proceedings of the National Academy of Sciences of the United States of America*, 69(7):1962–1966, July 1972. ISSN 0027-8424. URL http://view.ncbi.nlm.nih.gov/pubmed/4114859.

Paul L. Nunez and Ramesh Srinivasan. *Electric Fields of the Brain*. Oxford University Press, USA, January 2006. ISBN 9780195050387. doi: 10.1093/acprof:oso/9780195050387.001.0001. URL http://dx.doi.org/10.1093/acprof:oso/9780195050387.001.0001.

Harunori Ohmori. Neuronal specializations for the processing of interaural difference cues in the chick. *Frontiers in neural circuits*, 8:47, 2014.

Stefan N. Oline and R. Michael Burger. Short-term synaptic depression is topographically distributed in the cochlear nucleus of the chicken. *The Journal of Neuroscience*, 34(4):1314–1324, January 2014. ISSN 1529-2401. doi: 10.1523/jneurosci.3073-13.2014. URL `http://dx.doi.org/10.1523/jneurosci.3073-13.2014`.

Stefan N. Oline, Go Ashida, and R. Michael Burger. Tonotopic optimization for temporal processing in the cochlear nucleus. *Journal of Neuroscience*, 36(32): 8500–8515, August 2016. ISSN 1529-2401. doi: 10.1523/jneurosci.4449-15.2016. URL `http://dx.doi.org/10.1523/jneurosci.4449-15.2016`.

Nicolas Palanca-Castan, Geneviève Laumen, Darrin Reed, and Christine Köppl. The binaural interaction component in barn owl (tyto alba) presents few differences to mammalian data. *Journal of the Association for Research in Otolaryngology : JARO*, 17(6):577–589, December 2016. ISSN 1438-7573. doi: 10.1007/s10162-016-0583-7. URL `http://dx.doi.org/10.1007/s10162-016-0583-7`.

Erin E. Pararas, Zhiqiang Chen, Jason Fiering, Mark J. Mescher, Ernest S. Kim, Michael J. McKenna, Sharon G. Kujawa, Jeffrey T. Borenstein, and William F. Sewell. Kinetics of reciprocating drug delivery to the inner ear. *Journal of Controlled Release*, 152(2):270–277, June 2011. ISSN 01683659. doi: 10.1016/j.jconrel.2011.02.021. URL `http://dx.doi.org/10.1016/j.jconrel.2011.02.021`.

Roger S Payne. Acoustic location of prey by barn owls (tyto alba). *Journal of Experimental Biology*, 54(3):535–573, 1971.

Jose L. Peña, Svenja Viete, Yehuda Albeck, and Masakazu Konishi. Tolerance to sound intensity of binaural coincidence detection in the nucleus laminaris of the owl. *Journal of Neuroscience*, 16(21):7046–7054, November 1996. ISSN 1529-2401. URL `http://www.jneurosci.org/content/16/21/7046.abstract`.

Klas H. Pettersen and Gaute T. Einevoll. Amplitude variability and extracellular low-pass filtering of neuronal spikes. *Biophysical journal*, 94(3):784–802, February 2008. ISSN 1542-0086. doi: 10.1529/biophysj.107.111179. URL `http://dx.doi.org/10.1529/biophysj.107.111179`.

Klas H. Pettersen, Anna Devor, Istvan Ulbert, Anders M. Dale, and Gaute T. Einevoll. Current-source density estimation based on inversion of electrostatic forward solution: Effects of finite extent of neuronal activity and conductivity discontinuities. *Journal of Neuroscience Methods*, 154(1-2):116–133, June 2006. ISSN 01650270. doi: 10.1016/j.jneumeth.2005.12.005. URL `http://dx.doi.org/10.1016/j.jneumeth.2005.12.005`.

R. Plonsey. Action potential sources and their volume conductor fields. *Proceedings of the IEEE*, 65(5):601–611, May 1977. ISSN 0018-9219. doi: 10.1109/proc.1977.10539. URL http://dx.doi.org/10.1109/proc.1977.10539.

Jurgis Pods. A comparison of computational models for the extracellular potential of neurons. *Journal of Integrative Neuroscience*, 16(1):19–32, February 2017. ISSN 1757448X. doi: 10.3233/jin-170009. URL http://dx.doi.org/10.3233/jin-170009.

Jan Potworowski, Wit Jakuczun, Szymon Łęski, and Daniel Wójcik. Kernel current source density method. *Neural Computation*, 24(2):541–575, November 2011. doi: 10.1162/neco_a_00236. URL http://dx.doi.org/10.1162/neco_a_00236.

W. S. Pritchard. The brain in fractal time: 1/f-like power spectrum scaling of the human electroencephalogram. *The International journal of neuroscience*, 66(1-2):119–129, September 1992. ISSN 0020-7454. URL http://view.ncbi.nlm.nih.gov/pubmed/1304564.

Wilfrid Rall. Branching dendritic trees and motoneuron membrane resistivity. *Experimental Neurology*, 1(5):491–527, November 1959. ISSN 00144886. doi: 10.1016/0014-4886(59)90046-9. URL http://dx.doi.org/10.1016/0014-4886(59)90046-9.

I. M. Raman, S. Zhang, and L. O. Trussell. Pathway-specific variants of ampa receptors and their contribution to neuronal signaling. *Journal of Neuroscience*, 14(8):4998–5010, August 1994. ISSN 1529-2401. URL http://www.jneurosci.org/content/14/8/4998.abstract.

John C. R. Randle, Thierry Guet, Alexis Cordi, and Jean M. Lepagnol. Competitive inhibition by NBQX of kainate/AMPA receptor currents and excitatory synaptic potentials: importance of 6-nitro substitution. *European Journal of Pharmacology*, 215(2-3):237–244, May 1992. ISSN 00142999. doi: 10.1016/0014-2999(92)90033-z. URL http://dx.doi.org/10.1016/0014-2999(92)90033-z.

Margaret Rathouz and Laurence Trussell. Characterization of outward currents in neurons of the avian nucleus magnocellularis. *Journal of Neurophysiology*, 80(6):2824–2835, December 1998. ISSN 1522-1598. URL http://jn.physiology.org/content/80/6/2824.abstract.

Supratim Ray. Challenges in the quantification and interpretation of spike-lfp relationships. *Current Opinion in Neurobiology*, 31:111–118, April 2015. ISSN 09594388. doi: 10.1016/j.conb.2014.09.004. URL http://dx.doi.org/10.1016/j.conb.2014.09.004.

Supratim Ray and John H. R. Maunsell. Different origins of gamma rhythm and high-gamma activity in macaque visual cortex. *PLoS Biology*, 9(4):

e1000610+, April 2011. ISSN 1545-7885. doi: 10.1371/journal.pbio.1000610. URL http://dx.doi.org/10.1371/journal.pbio.1000610.

Wade G. Regehr. Short-term presynaptic plasticity. *Cold Spring Harbor Perspectives in Biology*, 4(7):a005702+, July 2012. ISSN 1943-0264. doi: 10.1101/cshperspect.a005702. URL http://dx.doi.org/10.1101/cshperspect.a005702.

Susanne Reichinnek, Thomas Künsting, Andreas Draguhn, and Martin Both. Field potential signature of distinct multicellular activity patterns in the mouse hippocampus. *Journal of Neuroscience*, 30(46):15441–15449, November 2010. ISSN 1529-2401. doi: 10.1523/jneurosci.2535-10.2010. URL http://dx.doi.org/10.1523/jneurosci.2535-10.2010.

Michael W. Reimann, Costas A. Anastassiou, Rodrigo Perin, Sean L. Hill, Henry Markram, and Christof Koch. A biophysically detailed model of neocortical local field potentials predicts the critical role of active membrane currents. *Neuron*, 79(2):375–390, July 2013. ISSN 08966273. doi: 10.1016/j.neuron.2013.05.023. URL http://dx.doi.org/10.1016/j.neuron.2013.05.023.

Samantha Richerson, Mark Ingram, Danielle Perry, and Mark M. Stecker. Classification of the extracellular fields produced by activated neural structures. *BioMedical Engineering OnLine*, 4(1):53+, September 2005. ISSN 1475-925X. doi: 10.1186/1475-925x-4-53. URL http://dx.doi.org/10.1186/1475-925x-4-53.

Helmut Riedel and Birger Kollmeier. Comparison of binaural auditory brainstem responses and the binaural difference potential evoked by chirps and clicks. *Hearing Research*, 169(1-2):85–96, July 2002. ISSN 03785955. doi: 10.1016/s0378-5955(02)00342-8. URL http://dx.doi.org/10.1016/s0378-5955(02)00342-8.

E. W. Rubel and T. N. Parks. Organization and development of brain stem auditory nuclei of the chicken: tonotopic organization of n. magnocellularis and n. laminaris. *The Journal of comparative neurology*, 164(4):411–433, December 1975. ISSN 0021-9967. doi: 10.1002/cne.901640403. URL http://dx.doi.org/10.1002/cne.901640403.

Jason T. Sanchez, Donald Gans, and Jeffrey J. Wenstrup. Contribution of NMDA and AMPA receptors to temporal patterning of auditory responses in the inferior colliculus. *Journal of Neuroscience*, 27(8):1954–1963, February 2007. ISSN 1529-2401. doi: 10.1523/jneurosci.2894-06.2007. URL http://dx.doi.org/10.1523/jneurosci.2894-06.2007.

Saeid Sanei and Jonathon A. Chambers. *EEG signal processing*. John Wiley & Sons, 2013.

Robson Scheffer-Teixeira, Hindiael Belchior, Richardson N. Leão, Sidarta Ribeiro, and Adriano B. L. Tort. On high-frequency field oscillations (>100 Hz) and the spectral leakage of spiking activity. *Journal of Neuroscience*, 33(4):1535–1539, January 2013. ISSN 1529-2401. doi: 10.1523/jneurosci.4217-12.2013. URL `http://dx.doi.org/10.1523/jneurosci.4217-12.2013`.

Erik W. Schomburg, Costas A. Anastassiou, György Buzsáki, and Christof Koch. The spiking component of oscillatory extracellular potentials in the rat hippocampus. *The Journal of Neuroscience*, 32(34):11798–11811, August 2012. ISSN 1529-2401. doi: 10.1523/jneurosci.0656-12.2012. URL `http://dx.doi.org/10.1523/jneurosci.0656-12.2012`.

C. E. Schroeder, C. E. Tenke, S. J. Givre, J. C. Arezzo, and H. G. Vaughan. Striate cortical contribution to the surface-recorded pattern-reversal VEP in the alert monkey. *Vision research*, 31(7-8):1143–1157, 1991. ISSN 0042-6989. URL `http://view.ncbi.nlm.nih.gov/pubmed/1891808`.

C. E. Schroeder, A. D. Mehta, and S. J. Givre. A spatiotemporal profile of visual system activation revealed by current source density analysis in the awake macaque. *Cerebral cortex (New York, N.Y. : 1991)*, 8(7):575–592, October 1998. ISSN 1047-3211. doi: 10.1093/cercor/8.7.575. URL `http://dx.doi.org/10.1093/cercor/8.7.575`.

Almut Schüz and Valentino Braitenberg. The human cortical white matter. In Almut Schüz, editor, *Cortical Areas*, chapter chapter 16, pages 377–386. Taylor & Francis, Abingdon, UK, 2002. ISBN 978-0-203-29582-3. doi: 10.4324/9780203219911_chapter_16. URL `http://dx.doi.org/10.4324/9780203219911_chapter_16`.

D. W. Schwarz. Can central neurons reproduce sound waveforms? an analysis of the neurophonic potential in the laminar nucleus of the chicken. *The Journal of Otolaryngology*, 21(1):30–38, February 1992. ISSN 0381-6605. URL `http://view.ncbi.nlm.nih.gov/pubmed/1564747`.

Matthew W. Self, Timo van Kerkoerle, Hans Supèr, and Pieter R. Roelfsema. Distinct roles of the cortical layers of area V1 in figure-ground segregation. *Current biology : CB*, 23(21):2121–2129, November 2013. ISSN 1879-0445. doi: 10.1016/j.cub.2013.09.013. URL `http://dx.doi.org/10.1016/j.cub.2013.09.013`.

Jonathan Z. Simon, Catherine E. Carr, and Shihab A. Shamma. A dendritic model of coincidence detection in the avian brainstem. *Neurocomputing*, 26-27:263–269, June 1999. ISSN 09252312. doi: 10.1016/s0925-2312(99)00020-x. URL `http://dx.doi.org/10.1016/s0925-2312(99)00020-x`.

Daniel J. Simons, George E. Carvell, Harold T. Kyriazi, and Randy M. Bruno. Thalamocortical conduction times and stimulus-evoked responses in the

rat whisker-to-barrel system. *Journal of Neurophysiology*, 98(5):2842–2847, November 2007. ISSN 1522-1598. doi: 10.1152/jn.00800.2007. URL http://dx.doi.org/10.1152/jn.00800.2007.

Manisha Sinha and Rishikesh Narayanan. Hcn channels enhance spike phase coherence and regulate the phase of spikes and LFPs in the theta-frequency range. *Proceedings of the National Academy of Sciences*, 112(17):E2207–E2216, April 2015. ISSN 1091-6490. doi: 10.1073/pnas.1419017112. URL http://dx.doi.org/10.1073/pnas.1419017112.

W. R. Softky and C. Koch. The highly irregular firing of cortical cells is inconsistent with temporal integration of random EPSPs. *The Journal of Neuroscience*, 13(1):334–350, January 1993. ISSN 0270-6474. URL http://www.jneurosci.org/content/13/1/334.abstract.

Eran Stark and Moshe Abeles. Predicting movement from multiunit activity. *The Journal of Neuroscience*, 27(31):8387–8394, August 2007. ISSN 1529-2401. doi: 10.1523/jneurosci.1321-07.2007. URL http://dx.doi.org/10.1523/jneurosci.1321-07.2007.

W. E. Sullivan and M. Konishi. Segregation of stimulus phase and intensity coding in the cochlear nucleus of the barn owl. *The Journal of Neuroscience*, 4(7):1787–1799, July 1984. ISSN 1529-2401. URL http://www.jneurosci.org/content/4/7/1787.abstract.

W. E. Sullivan and M. Konishi. Neural map of interaural phase difference in the owl's brainstem. *Proceedings of the National Academy of Sciences*, 83(21):8400–8404, November 1986a. ISSN 1091-6490. URL http://www.pnas.org/content/83/21/8400.abstract.

WE Sullivan and M Konishi. Neural map of interaural phase difference in the owl's brainstem. *Proceedings of the National Academy of Sciences*, 83(21): 8400–8404, 1986b.

H. A. Swadlow. Efferent neurons and suspected interneurons in S-1 vibrissa cortex of the awake rabbit: receptive fields and axonal properties. *Journal of Neurophysiology*, 62(1):288–308, July 1989. ISSN 1522-1598. URL http://jn.physiology.org/content/62/1/288.abstract.

Harvey A. Swadlow and Alexander G. Gusev. The influence of single VB thalamocortical impulses on barrel columns of rabbit somatosensory cortex. *Journal of Neurophysiology*, 83(5):2802–2813, May 2000. ISSN 1522-1598. URL http://jn.physiology.org/content/83/5/2802.abstract.

Harvey A. Swadlow, Alexander G. Gusev, and Tatiana Bezdudnaya. Activation of a cortical column by a thalamocortical impulse. *The Journal of Neuroscience*, 22(17):7766–7773, September 2002. ISSN 1529-2401. URL http://www.jneurosci.org/content/22/17/7766.abstract.

Terry T Takahashi and Masakazu Konishi. Projections of nucleus angularis and nucleus laminaris to the lateral lemniscal nuclear complex of the barn owl. *Journal of Comparative Neurology*, 274(2):212–238, 1988.

Ye-Zhong Tang and Catherine E. Carr. Development of n-methyl-d-aspartate receptor subunits in avian auditory brainstem. *J. Comp. Neurol.*, 502(3): 400–413, May 2007. doi: 10.1002/cne.21303. URL `http://dx.doi.org/10.1002/cne.21303`.

Zheng-Quan Tang and Yong Lu. Two GABAA responses with distinct kinetics in a sound localization circuit. *Journal of Physiology*, 590(16):3787–3805, 2012.

Jiannis Taxidis, Costas?A Anastassiou, Kamran Diba, and Christof Koch. Local field potentials encode place cell ensemble activation during hippocampal sharp wave ripples. *Neuron*, 87(3):590–604, August 2015. ISSN 08966273. doi: 10.1016/j.neuron.2015.07.014. URL `http://dx.doi.org/10.1016/j.neuron.2015.07.014`.

Bartosz Teleńczuk, Stuart N. Baker, Andreas V. M. Herz, and Gabriel Curio. High-frequency EEG covaries with spike burst patterns detected in cortical neurons. *Journal of Neurophysiology*, 105(6):2951–2959, June 2011. ISSN 1522-1598. doi: 10.1152/jn.00327.2010. URL `http://dx.doi.org/10.1152/jn.00327.2010`.

Bartosz Teleńczuk, Stuart N. Baker, Richard Kempter, and Gabriel Curio. Correlates of a single cortical action potential in the epidural EEG. *NeuroImage*, 109:357–367, April 2015. ISSN 10538119. doi: 10.1016/j.neuroimage.2014.12.057. URL `http://dx.doi.org/10.1016/j.neuroimage.2014.12.057`.

Craig E. Tenke, Charles E. Schroeder, Joseph C. Arezzo, and Herbert G. Vaughan. Interpretation of high-resolution current source density profiles: a simulation of sublaminar contributions to the visual evoked potential. *Experimental Brain Research*, 94(2):183–192, June 1993. doi: 10.1007/bf00230286. URL `http://dx.doi.org/10.1007/bf00230286`.

Misha Tsodyks, Klaus Pawelzik, and Henry Markram. Neural networks with dynamic synapses. *Neural Computation*, 10(4):821–835, May 1998. doi: 10.1162/089976698300017502. URL `http://dx.doi.org/10.1162/089976698300017502`.

Misha V Tsodyks and Henry Markram. The neural code between neocortical pyramidal neurons depends on neurotransmitter releaseprobability. *Proceedings of the National Academy of Sciences*, 94(2):719–723, January 1997. ISSN 1091-6490. doi: 10.1073/pnas.94.2.719. URL `http://dx.doi.org/10.1073/pnas.94.2.719`.

Svenja Viete, José L. Peña, and Masakazu Konishi. Effects of interaural

intensity difference on the processing of interaural time difference in the owl's nucleus laminaris. *The Journal of Neuroscience*, 17(5):1815–1824, March 1997. ISSN 1529-2401. URL http://www.jneurosci.org/content/17/5/1815.abstract.

Mark von Campenhausen and Hermann Wagner. Influence of the facial ruff on the sound-receiving characteristics of the barn owl's ears. *Journal of Comparative Physiology A*, 192(10):1073–1082, 2006.

Henrique von Gersdorff and J. Gerard Borst. Short-term plasticity at the calyx of held. *Nature Reviews Neuroscience*, 3(1):53–64, January 2002. ISSN 1471-003X. doi: 10.1038/nrn705. URL http://dx.doi.org/10.1038/nrn705.

Katrin Vonderschen. Processing of auditory signals in the forebrain of the barn owl: neural mechanisms of across-frequency integration. Technical report, 2008.

Hermann Wagner, Sandra Brill, Richard Kempter, and Catherine E. Carr. Microsecond precision of phase delay in the auditory system of the barn owl. *Journal of Neurophysiology*, 94(2):1655–1658, August 2005. ISSN 1522-1598. doi: 10.1152/jn.01226.2004. URL http://dx.doi.org/10.1152/jn.01226.2004.

Hermann Wagner, Sandra Brill, Richard Kempter, and Catherine E. Carr. Auditory responses in the barn owl's nucleus laminaris to clicks: Impulse response and signal analysis of neurophonic potential. *Journal of Neurophysiology*, 102(2):1227–1240, August 2009. ISSN 1522-1598. doi: 10.1152/jn.00092.2009. URL http://dx.doi.org/10.1152/jn.00092.2009.

Hermann Wagner, Lutz Kettler, Julius Orlowski, and Philipp Tellers. Neuroethology of prey capture in the barn owl (tyto alba l.). *Journal of Physiology-Paris*, 107(1-2):51–61, 2013.

Stephan Waldert, Roger N. Lemon, and Alexander Kraskov. Influence of spiking activity on cortical local field potentials. *The Journal of Physiology*, 591(21):5291–5303, November 2013. ISSN 1469-7793. doi: 10.1113/jphysiol.2013.258228. URL http://dx.doi.org/10.1113/jphysiol.2013.258228.

Tiantian Wang, Silviu I. Rusu, Bohdana Hruskova, Rostislav Turecek, and Borst. Modulation of synaptic depression of the calyx of held synapse by GABA B receptors and spontaneous activity. *The Journal of Physiology*, 591(19):4877–4894, October 2013. doi: 10.1113/jphysiol.2013.256875. URL http://dx.doi.org/10.1113/jphysiol.2013.256875.

S. G. Waxman and J. M. Ritchie. Organization of ion channels in the myelinated nerve fiber. *Science (New York, N.Y.)*, 228(4707):1502–1507, June 1985. ISSN 0036-8075. URL http://view.ncbi.nlm.nih.gov/pubmed/2409596.

NM Weinberger, LM Kitzes, and DA Goodman. Some characteristics of the 'auditory neurophonic'. *Experientia*, 26(1):46–48, 1970.

L. A. Westerman and R. L. Smith. Rapid and short-term adaptation in auditory nerve responses. *Hearing Research*, 15(3):249–260, September 1984. ISSN 0378-5955. URL `http://view.ncbi.nlm.nih.gov/pubmed/6501113`.

Dajun Xing, Chun-I I. Yeh, and Robert M. Shapley. Spatial spread of the local field potential and its laminar variation in visual cortex. *The Journal of neuroscience : the official journal of the Society for Neuroscience*, 29 (37):11540–11549, September 2009. ISSN 1529-2401. doi: 10.1523/jneurosci.2573-09.2009. URL `http://dx.doi.org/10.1523/jneurosci.2573-09.2009`.

Y Yan, PL Nunez, and RT Hart. Finite-element model of the human head: scalp potentials due to dipole sources. *Medical and Biological Engineering and Computing*, 29(5):475–481, 1991.

Lichuan Yang, Pablo Monsivais, and Edwin W. Rubel. The superior olivary nucleus and its influence on nucleus laminaris: A source of inhibitory feedback for coincidence detection in the avian auditory brainstem. *The Journal of Neuroscience*, 19(6):2313–2325, March 1999. ISSN 1529-2401. URL `http://www.jneurosci.org/content/19/6/2313.abstract`.

S. Zhang and L. O. Trussell. Voltage clamp analysis of excitatory synaptic transmission in the avian nucleus magnocellularis. *The Journal of Physiology*, 480(Pt 1):123–136, October 1994. ISSN 1469-7793. URL `http://jp.physoc.org/content/480/Pt_1/123.abstract`.

N. Zhou and T. N. Parks. Pharmacology of excitatory amino acid neurotransmission in nucleus laminaris of the chick. *Hearing Research*, 52(1):195–200, March 1991. ISSN 03785955. doi: 10.1016/0378-5955(91)90199-j. URL `http://dx.doi.org/10.1016/0378-5955(91)90199-j`.

Erik Ziegler, Sarah L Chellappa, Giulia Gaggioni, Julien QM Ly, Gilles Vandewalle, Elodie André, Christophe Geuzaine, and Christophe Phillips. A finite-element reciprocity solution for eeg forward modeling with realistic individual head models. *NeuroImage*, 103:542–551, 2014.

Muhammad S. A. Zilany, Ian C. Bruce, Paul C. Nelson, and Laurel H. Carney. A phenomenological model of the synapse between the inner hair cell and auditory nerve: Long-term adaptation with power-law dynamics. *Journal of the Acoustical Society of America*, 126(5):2390–2412, November 2009. ISSN 0001-4966. doi: 10.1121/1.3238250. URL `http://dx.doi.org/10.1121/1.3238250`.

Szymon Łęski, Henrik Lindén, Tom Tetzlaff, Klas H. Pettersen, and Gaute T. Einevoll. Frequency dependence of signal power and spatial reach of the

local field potential. *PLOS Computational Biology*, 9(7):e1003137+, July 2013. ISSN 1553-7358. doi: 10.1371/journal.pcbi.1003137. URL `http://dx.doi.org/10.1371/journal.pcbi.1003137`.

List of Figures

Selbständigkeitserklärung

Ich erkläre, dass ich die vorliegende Arbeit selbständig und nur unter Verwendung der angegebenen Literatur und Hilfsmittel angefertigt habe.

Berlin, den 22.05.2018 Thomas McColgan

List of publications

Philipp Berens, Jeremy Freeman, Thomas Deneux, Nicolay Chenkov, **Thomas McColgan**, Artur Speiser, Jakob H Macke, Srinivas Turaga, Patrick Mineault, Peter Rupprecht, et al. Community-based benchmarking improves spike inference from two-photon calcium imaging data. *bioRxiv*, page 177956, 2017.

Catherine Carr, Sahil Shah, Go Ashida, **Thomas McColgan**, Hermann Wagner, Paula T Kuokkanen, Richard Kempter, and Christine Köppl. Maps of ITD in the nucleus laminaris of the barn owl. In *Basic Aspects of Hearing*, pages 215–222. Springer, New York, NY, 2013.

Catherine Carr, Go Ashida, Hermann Wagner, **Thomas McColgan** and Richard Kempter. The role of conduction delay in creating sensitivity to interaural time differences. In *Physiology, Psychoacoustics and Cognition in Normal and Impaired Hearing*, pages 189–196. Springer, Cham, 2016.

Catherine E Carr, Sahil Shah, **Thomas McColgan**, Go Ashida, Paula T Kuokkanen, Sandra Brill, Richard Kempter, and Hermann Wagner. Maps of interaural delay in the owl's nucleus laminaris. *Journal of Neurophysiology*, 114(3):1862–1873, 2015.

Paula T Kuokkanen, Go Ashida, Anna Kraemer, **Thomas McColgan**, Kazuo Funabiki, Hermann Wagner, Christine Köppl, Catherine E Carr, and Richard Kempter. Contribution of action potentials to the extracellular field potential in the nucleus laminaris of barn owl. *Journal of Neurophysiology*, 119(4): 1422–1436, 2017.

Thomas McColgan, Sahil Shah, Christine Köppl, Catherine E Carr, and Hermann Wagner. A functional circuit model of interaural time difference processing. *Journal of Neurophysiology*, 112(11):2850–2864, 2014.

Thomas McColgan, Ji Liu, Paula Tuulia Kuokkanen, Catherine Emily Carr, Hermann Wagner, and Richard Kempter. Dipolar extracellular potentials generated by axonal projections. *eLife*, 6, 2017.